Electrochemical Poly(ProDOT) Dendritic DNA Aptamer Biosensor for Signalling Interferon Gamma (IFN-ɣ) TB Biomarker

By

Unathi Sidwaba

MSc Nanoscience

A thesis submitted in fulfilment of the requirements for the degree of

Doctor of Philosophy

Faculty of Science, Department of Chemistry

University of the Western Cape

Cape Town, South Africa

Supervisor: Prof Emmanuel I. Iwuoha

May 2017

ABSTRACT

Tuberculosis (TB) is an infectious disease that, despite all efforts devoted towards its eradication, remains a threat to many countries including South Africa. Current diagnostic assays do offer better performance than the conventional sputum smear microscopy and tuberculin skin tests. However, these assays have been proven to be affected by various factors including the condition of an individual's immune system and vaccination history. By far, electrochemical biosensors are amongst the currently investigated techniques to address the shortcomings associated with these diagnostics. At large, human health is prone to attack by various pathogens, toxins and chemicals such as bisphenol A (BPA) which is a chemical found in many household appliances owing to special properties such as light weight, high thermal resistance and transparency. This chemical is also a potential endocrine disruptor which mimics the functionality of estrogen receptors leading to adverse health problems including miscarriages, obesity, diabetes and cancer while its interference with functionality of the immune system alters secretion of cytokines such as interferon gamma (IFN-γ). IFN-γ is a cytokine secreted as immunological response specific to TB infection and has risen as the best biomarker for early TB screening. Hence, devices for IFN-γ quantification with high sensitivity and specificity are of crucial demand as they can indicate both TB infection and endocrine disruption. Herein, two conducting polymer nanocomposites have been prepared for use as redox probes and charge transfer mediators for assays developed to quantify the endocrine disrupting BPA and the TB biomarker, interferon gamma (IFN-γ). Metallic nanoparticles (gold nanoparticles and titanium dioxide nanoparticles) were employed to enhance the charge transfer efficiency of the conducting polymers; polyaniline (PANI) and poly(3,4-propylenedioxythiophene) (PProDOT). Their incorporation and effect on properties of the polymers was investigated using voltammetry (cyclic voltammetry, square wave voltammetry and differential pulse voltammetry), spectroscopy (Raman spectroscopy and ultraviolet-visible

spectroscopy), microscopy (scanning electron microscopy and transmission electron microscopy), chronocoulometry and electrochemical impedance spectroscopy. The sensing platform for bisphenol A was fabricated by immobilization of manganese peroxidase onto the PANI nanocomposite grafted with polymethyl methacrylate (PMMA) and titanium dioxide (TiO_2) nanoparticles. The biosensor system showed satisfactory performance during square-wave signalling of BPA by monitoring current changes during its oxidation. The biosensor could detect BPA with a low detection limit of 0.17 nM (corresponding to 0.039 pg/mL) and an analytical range between 0.2 nM and 1.2 nM. These values fall below the minimum tolerable daily intake value of 4 µg/kg bodyweight implying the potential application of this biosensor system in quantification of BPA in real household and environmental samples. Interferon gamma (IFN-γ) was signalled by monitoring changes in the phase angle with its varying concentrations. The sensing platform was a ternary system of PProDOT, gold nanoparticles and a thiol-modified DNA aptamer specific to IFN-γ. During recognition and subsequent binding of IFN-γ, the aptamer underwent conformational changes which retarded charge transfer and induced the observed shifts in phase angle. The aptasensor showed feasibility to detect IFN-γ in clinical samples, following its good performance during signalling of IFN-γ in pleural fluid. A detection limit of 0.2 pg/mL and a linear range with a minimum value of 0.4 pg/mL and a maximum value of 1.4 pg/mL were achieved. These detection limit values fall far below the current cut-off limit of 15 pg/mL for IFN- γ and set minimum value of 50 µg/kg for BPA, further highlighting the promising potential for application of the sensor systems towards early TB diagnosis and indication of endocrine disruption.

KEYWORDS

Aptasensor

Bisphenol A

Conducting polymer nanocomposites

Disease biomarker

DNA aptamer

Electrochemical impedance spectroscopy

Endocrine disrupting compounds

Gold nanoparticles

Immune system

Interferon gamma

Limit of detection

Pleural fluid

Poly(3,4-propylenedioxythiophene)

Tuberculosis

DECLARATION

I declare that "*Electrochemical Poly(ProDOT) Dendritic DNA Aptamer Biosensor for Signalling Interferon Gamma (IFN-γ) TB Biomarker*" is my original work, that has not been submitted before for any degree or examination in any other university. During review of published data and literature, all sources I have used or quoted have been indicated and acknowledged in accordance with standard reference practices.

UNIVERSITY *of the* WESTERN CAPE

Unathi Sidwaba   Signed:

June 2017

ACKNWLEDGEMENTS

I thank God Almighty for abiding by my side through the ups and downs I encountered while conducting this research. Through His grace, I completed the study.

To my Supervisor, Prof. Emmanuel Iwuoha, you may not know but You have been an inspiration ever since I started the research career under your supervision. I gratefully appreciate your tolerance for my 'disappearance' when times were tough.

To all Sensorlab Doctors, Seniors and Colleagues: Your assistance, information sharing, opinions, encouragement and advices have had a positive input during the conduction of this research project. Thank you all! Dr. T. Waryo, Dr. A. Baleg, Dr. F. Ngece, Dr. A. Jijana, Dr. C. Ikpo, Dr. Makelane, N. Dywili, N. Ntshongontshi, L. Wilson, S. Qakala, M. Ward, F. Muya, N. Hlongwa, X. Simelane, K. Pokpas, A. Djoumessi, V. Suru, L. Phelane, R. Elgmati and L. Pacoste.
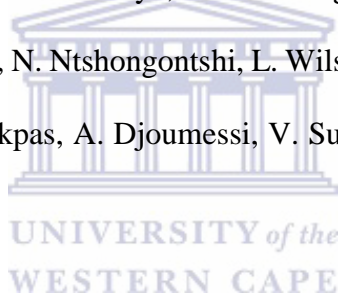
Family: To my mother, **Zoliswa Silaqu**, fathers (Mbomla Silaqu and Mayenzeke Gwadiso): Thank you very much for your unconditional love, courage and support. **Asive Sidwaba** and **Asikhanyisele Izibele Sidwaba,** you are my all! **Lubabalo Mngcongela,** thank you for everything.

To Usisipho Feleni: Thank you for being a part of my life. If only death could do us part!

## DEDICATION

This dissertation is dedicated to

My late father, Makhaza Skolo; brother, Siphamandla Silaqu and grandmother, Nocawe

Sidwaba

(May your souls rest in peace!)

Mother (Zoliswa Silaqu), aunt (Zoleka Mancasa), father (Mayenzeke Gwadiso)

Sisters (Simanye, Vuokazi and Simamkele)
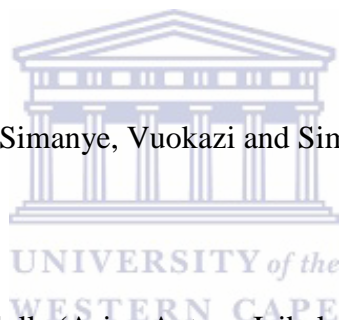
My dolls (Asive Antsor, Izibele Izzy)

Nephew and nieces (Avuziwe, Mivuyo, Luminathi and Iminathi)

Brothers (Lwazi and Vuyolwethu)

LIST OF PUBLICATIONS

Sidwaba, U., Waryo, T., Randall, P., Dheda, K., and Iwuoha, E. Electrochemical Poly(3,4-propylenedioxythiophene) DNA Aptamer Biosensor for Signalling Interferon Gamma (IFN-ɣ) TB Biomarker. *Biosensors and Bioelectronics*. (*In press*).

Sidwaba, U., Waryo, T., Randall, P., Dheda, K., and Iwuoha, E.I. Gold Nanoparticles Amplified Properties of Poly(3,4-propylenedioxythiophene). *ACS Sensors*. (*In press*).

Sidwaba, U., Ajayi, R.F., Feleni, U., Douman, S., Baker, P.G., Vilakazi, S.L., Tshikhudo, R. and Iwuoha, E.I., 2014, March. Polyanilino-Carbon Nanotubes Derivatised Cytochrome P450 2E1 Nanobiosensor for the Determination of Pyrazinamide Anti-Tuberculosis Drugs. *Nano Hybrids*. Vol. 6, pp. 59-73.

Sidwaba, U., Feleni, U., Makelane, H., Nxusani, E., Wilson, L., Qakala, S., Rassie, C., Masikini, M., Waryo, T., Ajayi, R.F., Baker, P. and Iwuoha E., 2016, A Novel Polyaniline Nanocomposite with Doping Effects of Poly(Methyl Methacrylate) and TiO_2 Nanoparticles. *Journal of Nano Research.* Vol. 44, pp. 281-294.

Ajayi, R.F., Sidwaba, U., Feleni, U., Douman, S.F., Nxusani, E., Wilson, L., Rassie, C., Tovide, O., Baker, P.G.L., Vilakazi, S.L. and Tshikhudo, R., 2014. A Nanosensor System Based On Disuccinimydyl–CYP2E1 for Amperometric Detection of the Anti-Tuberculosis Drug, Pyrazinamide. *World Academy of Science, Engineering and Technology, International Journal of Medical, Health, Biomedical, Bioengineering and Pharmaceutical Engineering*. Vol *8*(2), pp.67-71.

Socol, M., Rasoga, O., Breazu, C., Socol, G., Preda, N., Pasuk, I., Visan, D., Stavarache, I., Gherendi, F., Girtan, M., and Sidwaba, U., 2015. Heterostructures Based On Small Molecules Organic Compounds. *Digest Journal of Nanomaterials and Biostructures.* Vol. 10 (4), pp. 1383 – 1392.

Ajayi, R.F., Sidwaba, U., Feleni, U., Douman, S.F., Tovide, O., Botha, S., Baker, P., Fuku, X.G., Hamid, S., Waryo, T.T. and Vilakazi, S., 2014. Chemically amplified cytochrome P450-2E1 drug metabolism nanobiosensor for rifampicin anti-tuberculosis drug. *Electrochimica Acta*. Vol *128*, pp.149-155.

Rassie, C., van Wyk, J., Wilson, L., Makelane, H.R., Feleni, U., Sidwaba, U., Mapolie, S., Baker, P. and Iwuoha, E., 2015. Microscopy and electroanalysis of a first generation copper-poly (propyleneimine) metallodendrimer system. *International Journal of Electrochemical Science.* Vol 10, pp.432-444.

Masikini, M., Ndangili, P.M., Ikpo, C.O., Feleni, U., Duoman, S., Sidwaba, U., Waryo, T.T., Baker, P.G. and Iwuoha, E.I., 2016. Optoelectronics of stochiometrically controlled palladium telluride quantum dots. *Journal of Nano Research*, Vol 40, pp. 29-45.

Feleni, U., Ajayi, F., Jijana, F., Siwaba, U., Duoman, S., Baker, P. and Iwuoha, E., 2016. Tin Selenide Quantum Dots Electrochemical Biotransducer for the Determination of Indinavir-A Protease Inhibitor Anti-Retroviral Drug. *Journal of Nano Research,* Vol 44, pp. 196-207.

LIST OF CONFERENCES

Unathi Sidwaba, Emmanuel I. Iwuoha, Priscilla G.L. Baker, Rachel F. Ajayi. A novel titanium dioxide modified polyaniline/polymethyl methacrylate-based MnP nanobiosensor for detection of bisphenol A. 3rd International Symposium on Electrochemistry; Materials, Analytical and Physical Electrochemistry Today (MAPET), University of the Western Cape, South Africa, 26-28 May, 2015. *(poster)*

Unathi Sidwaba, Emmanuel Iwuoha. A novel titanium dioxide modified polyaniline/polymethyl methacrylate-based MnP nanobiosensor for detection of bisphenol A. 7th International Symposium on Macro- and Supramolecular Architecture and Materials (MAM-14), Johannesburg, South Africa, 23 -27 November, 2014. *(oral)*

Unathi Sidwaba, Fanelwa Ajayi, Emmanuel Iwuoha, Abongile Jijana. Development of methacrylate hydrogel nanobiosensor for phenolic endocrine disrupting compound, Bisphenol A. 13th Topical Meeting of the International Society of Electrochemistry Advances in Electrochemical Materials Science and Manufacturing, Pretoria, South Africa, 7-10 April, 2013. *(poster).*

.

TABLE OF CONTENTS

http://etd.uwc.ac.za

UNIVERSITY *of the*

WESTERN CAPE

http://etd.uwc.ac.za

LIST OF FIGURES

PART 1: BACKGROUND

CHAPTER 1

Research background, aims and objectives

Overview

Tuberculosis (TB) has been, and is still, a global burden amongst other highly infectious diseases, with alarming new cases reported annually by the World Health Organization (WHO). Although incredible commitment has been devoted in preventing the spread of the bacteria causing the disease, inventing of modernized diagnostic methods and therapy monitoring techniques, South Africa and other high burden countries (as categorized by the WHO), still show the highest TB incidents. On the other hand, endocrine disrupting chemicals (EDCs) have found applications in household appliances owing to the interesting properties they have. However, they have negative and harmful effects on human health, resulting from disruption of the endocrine system and interference with the immune system. More importantly, EDCs have been proven to interfere with secretion of cytokines including IFN-γ, a cytokine specific to TB infection. Therefore, much work ranging from invention of highly sensitive, reliable detection methods for the EDCs to development of new vaccines, highly sensitive point-of-care diagnostics and treatment drugs effective against all TB strains still remains.

This chapter gives a brief introduction to TB (causes, transmission, treatment, diagnostics and their challenges) and EDCs (applications and effects on human health), followed by current perspectives around TB and EDCs that led to conduction of this study.

1.   Introduction to tuberculosis

1.1. Tuberculosis: infection and pathogenesis

Tuberculosis (TB), a highly infectious disease that primarily targets the lungs, is caused by invasion of the human immune system by the bacterial human pathogen *Mycobacterium tuberculosis* (*MTb*), whose organisms are known as *tubercle bacilli* [1–3]. Amongst other human pathogens (Mycobacterium *africanum* and Mycobacterium *canetti*) within the mycobacterium tuberculosis complex (MTBC), *MTb* is the only significant pathogen that causes TB in humans [4]. All other bacterial species are collectively referred to as mycobacterium other than tuberculosis (MOTT) or non-tuberculous mycobacterium (NTM) organisms [5]. However, although *Mycobacterium bovis* is an animal pathogen, it is also known to cause the TB disease in humans [6]. Upon intake by the human system, *MTb* organisms bind to the alveolar macrophage and get recognised by different receptors such as the C-type lectin receptors, toll-like receptors and nod-like receptors [7]. The stage of infection in which the bacilli reside in a dormant manner within the system, without evident signs of sickness, is known as latent TB infection (LTBI) [8]. The advanced stage in which symptoms are evident, following a series of interaction mechanisms occurring between the defensive immune system and the bacilli-infected cells is active TB, commonly referred to as pulmonary TB (PTB). Common symptoms of PTB include persistent coughs with presentable bloody sputum, haemoptysis, excessive night sweats, loss of appetite, chest pain, short breaths and weight loss [9]. The time period between this symptomatic stage and bacillary entry is known as the incubation period [10] and it is during this period that the bacilli can travel to infect other parts of the body (such as the lymph nodes, kidneys, liver and meninges) [11] or progress to therapy-resistant strains resulting from chromosomal mutations [12]. These therapy-resistant forms of TB include multi-drug resistant TB (MDR-TB) which is resistant against at least two first-line anti-TB drugs

(rifampicin and isoniazid) while the extensively drug-resistant TB (XDR-TB) is resistant to both these first-line drugs and one of the fluoroquinolones and injectable second-line anti-TB drugs (ofloxacin (OFX) and amikacin (AMK)) [13]. The different categories of treatment drugs will be discussed in detail in the next section. The TB of any body part other than the lungs is referred to as extra-pulmonary TB (EPTB) [14] and the symptoms differ according to the site of infection [15]. Examples of EPTB include TB lymphadenitis, TB meningitis and hepatic TB, resulting from infection of the lymph nodes, the meninges and the liver, respectively [16–18].

The mechanism of defence against *MTb* infection is quite understandable and depends mainly on the condition of an individual's immune system. The immune cells respond by forming a barrier, known as granuloma, which engulfs the tubercle bacilli confining them to an environment designated to hinder bacilli replication and spreading [19]. Specifically responding to *MTb* infection, the helper T (Th) CD4+ cells and CD8+ cells then secrete antimicrobial intermediates (such as the reactive oxygen intermediates (ROIs) and the reactive nitrogen intermediates (RNIs)) and cytokines (such as tumor necrosis factor alpha (TNF-α), interleukin 2 (IL-2) and interferon gamma (IFN-γ)) responsible for killing or hindering replication of the bacilli [20, 21]. When the immune system is weak (i.e. deficient in certain immunity cells), it fails to engulf and control the bacilli. This allows replication of the bacilli, empowering them to defeat the immune system [22] and these due to small sizes get carried to other body parts leading to extra-pulmonary TB. However, not only a weaker immune system permits progression of LTBI to active TB, but also the deceitful character of the tubercle bacilli rendered by the glycolipids forming its cell wall. The glycolipids contain mycolic acids, Wax-D and cord factors which are the main root for the special deceitful character of the tubercle bacilli. As a result, the bacilli have an ability to resist attack from the toxic intermediates secreted by the immune cells for defence, creating an environment comfortable enough for their growth and survival. The high concentrations of glycolipids are associated with resistance

of the bacteria to many antibiotics (development of the MDR-TB and XDR-TB strains). The bacilli can also inhibit cell apoptosis at the site of infection [23]. The driving force beyond this inhibition is the *MTb* nuoG mutant gene which accommodates the reactive oxygen intermediates, leading to increased apoptosis within the infected cells [24]. During all this time, viable bacilli get a chance to replicate within the granuloma and, after breaking the granuloma wall due to a damaged immune system, escape to re-circulate within the host. This behaviour is directly linked to re-activated infection (or secondary infection), which is a symptomatic active TB disease usually observed months or years after the initial infection [25].

Despite the remarkable worldwide commitment initiated by the World Health Organization (WHO), co-infection with other pathogens and immunosuppressing conditions, mainly the human immunodeficiency virus (HIV) and diabetes mellitus (DM) complicates the control over TB [26,27]. Also, malnutrition has been associated with TB mortality. The world, generally, is aware and cautious against TB, thanks to strategies such as directly observed treatment short course therapy (DOTS), the STOP-TB Strategy and the recent End-TB Strategy [28,29], implemented to engage with communities about TB and fulfil various goals with the universal vision of a TB-free world. However, although some people have adapted to healthy nutritional lifestyles, deficiency of vitamin D (Vit D), alone, increases the risk of LTBI progression to active TB disease with a current serum-measured value of ≤20 nmol/L regarded as Vit D deficiency [30]. Calcitriol or 1,25-dihydroxyvitamin D_3 ($1,25(OH)_2D_3$), one active metabolite of Vit D, modulates immune response by inducing formation of the antibacterial RNIs and ROIs [31,32]. Hence, it has been shown that a Vit D-supplemented therapy accelerates recovery but such observations still need validation [33]. This Vit D deficiency points out that various factors have an effect on control of the TB epidemic.

4

1.2. Transmission, prevention and treatment

The tubercle bacilli carried by airborne particles called droplet nuclei, are small organisms of 0.5 μm in width, usually 3 μm long [34]. The MTb-containing droplet nuclei can remain suspended in air for 8-10 days while they can last for 20-30 hours in expelled sputum. When an infected individual (with active TB disease) sneezes or coughs, the bacilli are expelled in aerosol form. The main transmission route, therefore, is the respiratory tract through which the bacilli is expelled (from the active TB-infected individual) and inhaled (by the individual being infected) [8,35] and one individual can transmit the disease to an average of 12-15 persons [36]. With reference to *M. bovis*, the organism enters the human system through ingestion of unpasteurized bacilli-contaminated cow milk [37]. After acquiring *MTb* infection, different population groups are prone to LTBI progression to active TB disease, mainly healthcare workers in frequent exposure to active TB individuals, infants with immature immune systems, immunocompromised individuals visiting healthcare centres and close contacts with active TB-infected individuals. Hence these population groups are classified as high risk groups [38].

Currently, there is only one gold standard vaccine, the *M. bovis* Bacillus Calmette-Guérin (BCG) which is administered through intradermal injections at birth by many countries including South Africa [39]. However, as an additional cautious measure against infection of the high risk groups, the vaccine is also administered after infancy or regularly (especially to healthcare workers). Like most systems, the BCG vaccine has a limitation which is the over-stimulation of CD4+ and CD8+ cells, thereby affecting results from different diagnostic and therapy-monitoring techniques. Although the vaccine protects against *MTb* infection and progression from LTBI to active TB [40], it has been proven to have variable efficacy in preventing pulmonary TB or transmission of the bacteria and fails to give total protection in certain age groups or populations, following the high incident of TB infected infants who had

5

been vaccinated [41]. As a result, development of new and effective vaccines is under research, with some developed vaccines undergoing clinical trials. Amongst these is the Modified Vaccina Ankara 85A (MVA85A) in which the MVA expresses high levels of the antigen 85A. The MVA85A has been trialled in BCG-vaccinated infants in South Africa, for safety precautions, and it has shown no superior efficacy than the BCG [42]. Hence, new vaccines are still on demand.

The current TB therapy is a fixed-dose multi-drug regimen containing first-line and second-line TB drugs, ranked by the WHO according to their effectiveness against the disease bacteria. The first-line drugs, mainly used in treatment of drug-susceptible TB, include rifampicin (RIF), isoniazid (INH), pyrazinamide (PZA), ethambutol (EMB) and streptomycin (STR) which usually replaces EMB in EPTB cases, mainly TB meningitis. These drugs are administered for 2 months in the initial phase of treatment, known as the intense phase. This phase adopts the name from the efficacy and potency of the first-line drugs towards eradication of the bacteria. To complete the standard six-months duration, the intense phase is followed by a continuous phase in which only RIF and INH are administered for four months, mainly to prevent relapse and ensure eradication of the slowly-growing bacteria [43,44]. To monitor the effect of the drugs, sputum specimens are examined on a monthly basis [45]. The anti-TB drugs have adverse effects on human health resulting from their toxicity, with the most critical condition being permanent lung tissue and liver damage [46]. The treatment for the drug-resistant TB strains (MDR-TB and XDR-TB) varies from the standard treatment regimen for drug susceptible pulmonary TB, with administration of second-line drugs and is administered over longer periods, ranging between nine and twenty months, a period including nine months of only the intensive phase [13,47]. The second-line drugs are divided into fluoroquinolones (ofloxacin (OFX), levofloxacin (LEV), moxifloxacin (MOX) and ciprofloxacin (CIP)) and injectable drugs (kanamycin (KAN), amikacin (AMK) and capreomycin (CAP). The long

treatment period is directly linked to patient non-compliance as many people start by defaulting treatment, leading to the high number of reported drug-resistant TB cases and death, resulting from re-emergence of the disease [48,49]. The mutations in the *inhA* promoter and *katG* genome regions are responsible for INH resistance while mutations in the *rpoB* and *pncA* genome regions lead to RIF and PZA resistance, respectively [50]. Upon initiation of treatment, the drugs are metabolized by enzymes, mainly cytochrome P450 (CYP450) enzymes, into intermediates and metabolites effective against the bacteria. However, the drugs inhibit and induce the actions of these enzymes [51] and lead to adverse effects including liver damage. As a result, attempts including shortening of the therapy duration by at least two months and varying the drug dosages have been proposed as potential benefits that could minimise the emergence of drug-resistant TB strains and toxicities associated with long therapy durations. A study evaluating significance of a smear-positive result for tubercle bacilli after five months of treatment (treatment monitoring) showed that the positive results resulted from non-viable *Mtb* bacilli and/or MOTTs while a recent clinical trial study evaluating administration of a high rifampicin dosage has discovered no association between high RIF doses and cytotoxicity [40,52]. This view has opened doors to the newly emerging field of host-directed therapies (HDTs) which target biological pathways in the host to modulate immune response using readily approved immunomodulatory agents. Some agents include metformin (used against diabetes mellitus), niraparib (used in breast cancer) and Vit D3 (given as a dietary supplement) [53,54]. All these research interests show potential towards elimination of drug toxicities associated with the long therapy durations and drug interactions in patients simultaneously treating TB with other diseases and encourage patient compliance, which in turn, would have a positive effect on control of the TB disease.

1.3. Principles and challenges of current diagnostic methods

The tuberculin skin test (TST) is one of the oldest techniques for latent TB infection diagnosis. The technique is based on a delayed-type hypersensitivity reaction which occurs when an *MTb* infected individual is subjected to intradermal injections of five tuberculin units (TU) of purified protein derivative (PPD) or two TU of PPD RT23 culture filtrates [9,55]. In the case of a positive reaction, an induration appears (within 48-72 hours) at the site of injection. The positive reaction is then interpreted based on the diameter of the induration. Although this old technique is still operatory to date, it only detects LTBI (and not active TB) and it is important to note that the culture filtrates do not only contain strains from the *MTb* genome, but include strains from the BCG and some MOTT genomes [56]. As a result, the specificity performance of the TST is highly affected by BCG vaccination and exposure to MOTT strains giving false-positive results; while the sensitivity decreases with different factors (such as malnutrition and HIV co-infection which reduces CD4+ T cells) and give false-negative results, respectively [57]. Hence, absence or presence of a reaction does not solely rule out or indicate TB infection due to different factors, such as suppression of the reaction in immune-compromised individuals or overstimulation of the CD4+ and CD8+ T cells induced by the BCG vaccination.

The sputum smear microscopy (SSM) is based on identification of the acid-fast bacilli using fluorescent microscopy (from a sputum sample stained with Ziel-Neelsen stain or auramine stain). Although the technique gives results at high specificity within fourty eight hours, it has reduced specificity which needs confirmation by other methods as it fails to differentiate *MTb* from other mycobacterial strains such as *mycobacterium kansasii* and *mycobacterium marinum* [58]. The technique also has variable sensitivity in special populations including young children, diabetic and HIV co-infected individuals who fail to present MTb positive smears [59,60]. As a result, three polymerase chain reaction (PCR)-based techniques that also use sputum specimens

were later endorsed. One technique is the Gene Xpert MTB/RIF Assay (Xpert) which rapidly detects MTb infection and resistance to rifampicin (RIF) within two hours. The Xpert uses enclosed cartridges that minimise many errors such as sample cross-contamination [61,62]. The Genotype MTBDRplus technique (DRplus) and the Line Probe Assay (LPA) also detect early *Mtb* infection and, in addition to RIF resistance, measure resistance to isoniazid (INH) anti-TB drug [58,63,64]. However, the Xpert and the DRplus cannot discriminate non-viable from viable bacteria, leading to increased DNA amplification which limits their application in treatment monitoring [65] while the LPA can only be performed on confirmed positive smears [66].

Interferon gamma release assays (IGRAs) were designed to address the limitations associated with the afore-mentioned techniques (i.e. post-BCG vaccination and MOTT false-positive results, HIV co-infection false-negative results due to low CD4+ T cell counts, inability to differentiate LTBI from active TB and DNA amplification due to non-viable mycobacteria). There are two commercially available IGRAs approved by the U.S. Food and Drug Administration (FDA), namely; the QuantiFERON-TB Gold-in-Tube (QFT GIT) assay (Cellestis, Australia) and the T-SPOT.TB assay (Oxford Immunotec, UK). Both techniques are based on quantification of the antigen IFN-γ by peripheral blood cells, after stimulation by the antigens culture filtrate protein-10 kDa (CFP-10) and the early secreted antigenic target-6 (ESAT-6) [67]. These antigens have genomes within the region of difference 1 (RD1) specific to *Mtb*, excluding the BCG and other MOTT genomes. Therefore, performance of the IGRAs is not affected by past BCG vaccination or cross-reactivities with MOTTs [68]. The results from both assays are reported as a difference between the antigen response and negative control samples. The T-SPOT.TB assay is an enzyme-linked immunosorbent spot (ELISPOT)-based technique which measures the number of T cells (known as spots) producing IFN-γ. The reference for a positive result is ≥8 spots. The QFT GIT assay is an enzyme-linked immunosorbent assay (ELISA)-based technique which uses an additional antigen TB7.7 to

measure the amount of IFN-γ produced by the T-cells, expressed in international units (IU) per millilitre (mL) .The reference concentration for a positive result is $\geq$ 0.35 IU/mL [68,69]. Although the IGRAs seem to have addressed limitations associated with other diagnostic techniques [70], there are still controversial reports regarding the sensitivity of IGRAs in immunocompromised individuals where it is reported that the IGRAs sensitivity is diminished in young children and those living with TB/HIV co-infection [55,71,72].

2. Endocrine disrupting chemicals

2.1. Bisphenol A

Bisphenol A (BPA) is a monomer widely used in the production of epoxy resins and polycarbonate plastics owing to its properties such as light-weight, transparency and thermal resistance [73,74]. These epoxy resins and polycarbonate plastics yield material perfectly applied in packaging material and household appliances including compact discs, currency notes, flame retardants, plastic containers, eyewear and lining of metal food cans [75–77].

Unfortunately, exposure to BPA is associated with adverse effects harmful to human health, aquatic species and the environment. BPA has been proven to leach out of the food-packaging material, making its way to the contents while it can degrade from disposed material to finally reach ground waters [78]. In its chemical structure, BPA has two reactive phenolic groups through which it binds to estrogen receptors and interfere with both the endocrine and immune systems [79–82]. Specific disorders resulting from this interference include miscarriages, cancer (breast cancer and prostate cancer), obesity, neurodevelopmental disorders, birth defects, cardiovascular diseases and diabetes [83–87]. As a result of the adverse effects arising from exposure to the chemical, BPA is classified within a group of chemicals collectively known as endocrine disrupting chemicals (EDCs). As a protective measure to mitigate exposure to EDCs, various organisations and regulatory bodies implemented fixed values

regarded as no-observable-effect values and the current value for BPA is 50 µg/kg bodyweight per day [88].

3. Problem statement

3.1. Current TB statistics

Up to date, the World Health Organization (WHO) has shown remarkable progress towards controlling the TB epidemic which affects both young and old individuals around the world [89]. Despite the high cure rates and the fall in overall TB-related incidents achieved through different strategies implemented by the WHO, another important aspect accredited to the WHO is the endorsement of new innovations which have a great impact on the overall aim of eradicating TB, shown by a smooth transition from the STOP-TB era (which ended in 2015) to the new END-TB era destined to 2035.

Although TB is a curable disease, marked by 43 million lives saved between 2000 and 2014 [90], it has resulted in an estimated 7.4 million deaths between 2011 and 2015 (Figure 1), a value averaged at 1.5 million deaths per year. In 2015, the WHO reported an estimated 10.4 million TB cases which included 1.2 million TB/HIV co-infections in adults and a total 1.0 million TB cases in children [91]. When compared to previous years (i.e. 2011-2014), incidents reported on both TB/HIV- and TB/HIV+ infected adults show a gradual increase while the TB cases on children doubled. This phenomenal pattern may be attributed to either advances in diagnostic methods (allowing all WHO countries to report on incidents when compared to previous years in which many cases might have been missed undiagnosed) or the spread of the disease as the greatest proportion of the reported cases is constituted by low- and middle-income countries characterized by factors which favour spread of the bacteria causing the disease. These factors include nutritional deficiency, overcrowded populations (mainly in prisons) and infections with other infectious and non-communicable diseases[92,93]. Also, this

may relate to the limited efficacy of the BCG vaccine towards prevention against the TB disease.

In all these WHO Global TB reports, South Africa (SA) has been prominently appearing amongst the high burden countries (HBCs), ranked according to the mortality and morbidity rates of TB. Despite the remarkable progress towards TB control, SA still has the highest TB incidents and lower rates towards TB mortality reduction within the African region [94] and TB, nationally, has been the leading cause of death between 2012 and 2015 [95,96]. Among the alarming new cases of TB, there is a substantially increasing proportion of MDR-TB and XDR-TB cases which, despite emerging from treatment defaulting [97], can be directly
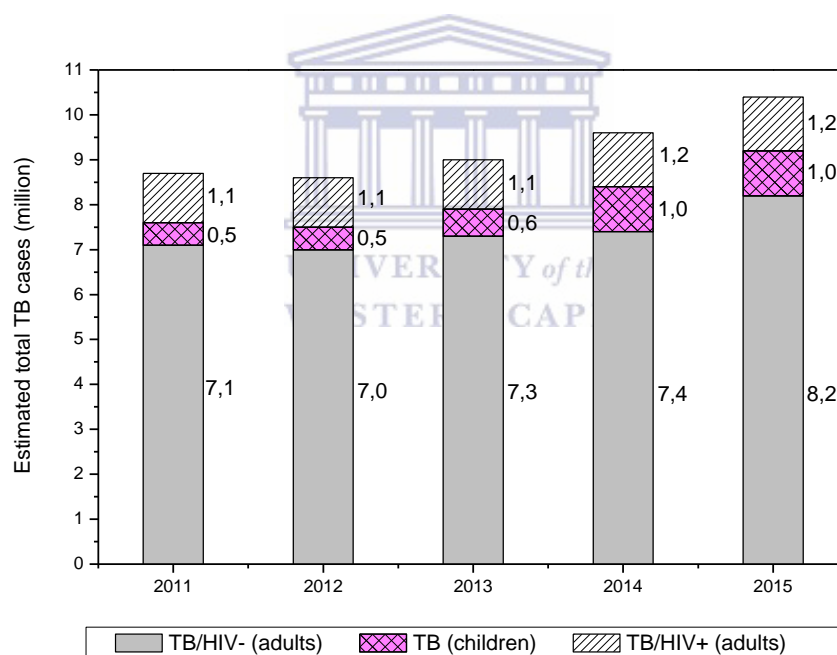
Figure 1:Annual TB trends that occurred between 2011 and 2015, highlighting the incidents of TB/HIV co-infection in adults and total TB incidents in children [91, 98,99,100,77].

acquired after exposure to drug-resistant TB strains [101]. SA prisons hold the largest population with the highest risk of rapid LTBI progression to active TB due to factors such as over-

crowding (with approximately 1.6 million inmates as in 2016 (sentenced and un-sentenced inmates) poor nutrition, limited access to healthcare facilities and prolonged close-contact exposure to infected individuals [102, 103].

3.2. Problem identification

TB continues to be a global threat to human health, in spite of all efforts ranging from preventing the spread of the disease to clinical evaluation of new vaccines and drugs and endorsement of highly sensitive diagnostic methods, characterized by a rapid turn-around time towards early diagnosis of TB. Although extensive attention has been paid to co-infection with HIV as one of the main factors with a negative retarding impact on the control of TB, the surprisingly increasing number of diabetes conditions worldwide, with a large number in LMICs has triggered an alarm that recently led the WHO to launching a global report on diabetes [104]. As documented on the report, diabetes led to 1.5 million deaths in 2012, with an additional 2.2 million death cases associated with diabetes-induced conditions. Alongside the complexity of the DM condition leading to complications such as blindness, cardiovascular disease and leg amputation, the TB/DM co-morbidity has been shown to be even higher than the TB/HIV co-morbidity with an estimated 522 million individuals to be infected with DM by 2030 and some correlation among antigens secreted by T-cells as an immune response to co-infection of these two diseases has been shown [27,105]. At a national level, the increase in number of TB deaths in SA, from 1.5 million in 2014 to 1.8 million in 2015, may be directly linked to the large number of treatment defaults [106] which may, in turn, have resulted in the steady increase in drug-resistant TB strains and TB-related deaths [107].

In addition to the immune-suppressing medications and co-infection with HIV and diabetes, BPA alters with the cytokine-secretion functionalities of the immune system leading to overstimulation of IFN-γ levels while imitation of the estrogenic functionalities leads to

adverse health disorders at concentrations much lower than the fixed allowable values. This aspect implies the ability of BPA to interfere with the plans headed towards onset identification of TB infection. This also adds to one of the limitations associated with current diagnostics where the IGRAs sensitivity is attenuated by a suppressed immune system. Moreover, the PCR-based Xpert and DRplus techniques are limited by false results arising from their failure to discriminate viable from non-viable bacteria while the LPA can only be performed on positive smears. Drawing from these aspects, a point-of-care diagnostic device that can identify onset TB infection with a fast turnaround time performance without hinging on other techniques is on demand. Additional crucial characteristics of such a device include portability, user-friendly handling and a sensitivity performance unaffected by the condition of the immune system. In view of the challenges around TB control, including the limitations of current diagnostic devices and factors deteriorating the immune system hence making human health prone to attack by various pathogens, this study sought to fabricate a system that addresses the afore-mentioned limitations of TB diagnostics by employing gold nanoparticles due to their signal-amplifying ability (with the aim of achieving high sensitivity) while the conducting polymer poly(3,4-propylenedioxythiophene) (PProDOT) is expected to facilitate charge transfer allowing easy monitoring of all binding and detection processes. In addition, use of the IFN-γ specific aptamer is hoped to increase the selectivity of the fabricated system, automatically avoiding interferences by NMTs and other pathogens. Separately, the study also fabricates a system for quantification of BPA that would potentially benefit both the medical field towards early identification of endocrine disruption or immune system interference and the regulatory sector by ensuring that BPA levels are within the allowable limits. The system is based on charge transfer mediation by a nanocomposite of polyaniline (PANI) grafted with polymethyl methacrylate (PMMA) and titanium dioxide (TiO_2) nanoparticles. The enzyme MnP was then

immobilized as a recognition element employed due to its ability to degrade phenolic compounds.

4. Motivation

Amongst the available devices or techniques used in diagnostics, electrochemical biosensor-based systems still over superior performance by addressing the limitation of poor sensitivity and specificity. Such performance arises from the use of highly electroconductive materials (polymers such as polyaniline PANI) whose properties are enhanced by different nanomaterials such as quantum dots (e.g. cadmium sulfide (CdS)), gold nanostructures (e.g. nanospheres or nanoparticles, nanorods and nanotubes) and carbon nanomaterials (e.g. carbon nanotubes and graphene) [108–112]. The resulting composites or hybrids are perfect candidates for biosensor fabrication as they act as both electron-transfer mediators (allowing easy monitoring of all mechanisms and interactions that occur) and as biocompatible receiving matrices for the biomolecules (ensuring non-destructive immobilization which, in turn, reserves the catalytic activity of the biomolecule). To increase the specificity of electrochemical biosensor systems, aptamers and enzymes are amongst the most studied biomolecules due to their high affinity towards their targets. Aptamers have been selected against pathogens and disease biomarkers including hepatitis (hepatitis C virus (HCV)), TB (interferon gamma (IFN-γ) and 10-kDa culture filtrate protein (CFP-10)), HIV (HIV glycoprotein 120 (HIV gp120)) and Burkitt lymphoma (Ramos cells) [113–117] . Therefore, use of aptamers in bioassays eliminates non-specificity and minimizes interference, hence maximizing sensitivity and performance of the fabricated systems.

Due to the specificity and high binding affinity of aptamers towards target analytes and the bio-recognition character of enzymes towards their substrates, these biomolecules have been employed in electrochemical biosensors for detection of disease biomarkers such as IFN-

15

γ and endocrine disruptors such as BPA. Motivated by studies where detection limits as low as 0.34 pg/ml for IFN-γ and 0.19 pM for BPA were obtained [112,118, 119], this study sought to develop rapid detection assays for TB and endocrine disrupting chemicals which both affect the human immune system negatively.

5. Research aims and objectives

The main and overall aim of this study was to develop an aptasensor system based on a highly electroactive nanocomposite manipulating the thiol-gold chemistry between the sulphur element of poly(3,4-propylenedioxythiophene) (PProDOT) and the gold element of gold nanoparticles (AuNPs). Integration of the thiolated IFN-γ binding aptamer onto this nanocomposite platform would then yield an aptasensor for quantitative detection of the tuberculosis biomarker, interferon gamma (IFN-γ). Due to interference of BPA with the immune system, leading to reported stimulation of IFN-γ levels, an enzyme-based system was separately prepared for its electrochemical quantification. The biosensor system employs a conducting polymer nanocomposite of polyaniline (PANI), polymethyl methacrylate (PMMA) and titanium dioxide (TiO$_2$) nanoparticles. Onto this nanocomposite, the enzyme manganese peroxidase (MnP) would then be immobilized to successfully fabricate a biosensor system for quantification of BPA.

Refined objectives of the study included:

A. An aptasensor for IFN-γ detection

(a). Novel polymerization of poly(3,4-propylenedioxythiophene) (PProDOT) from its monomer using a gold salt as an initiator, followed by structural, optical, morphological and electrochemical characterization using necessary techniques.

(b). Incorporation of gold nanoparticles to the PProDOT, with the aim of obtaining a PProDOT-AuNPs nanocomposite of improved electroactivity to act as a redox probe and a receiving matrix for the aptamer during device fabrication. Successful incorporation of the gold nanoparticles was monitored using different techniques.

(c). Fabrication of the aptasensor device through attachment of a thiolated IFN-γ binding aptamer (as an analyte recognition element) onto the PProDOT-AuNPs nanocomposite platform. Confirmation of binding between the aptamer and the nanocomposite, conferring successful fabrication of the aptasensor, was evaluated using electrochemical and optical techniques.

(d). Diagnostic application of the aptasensor system for detection of interferon gamma in spiked pleural fluid samples using electrochemical transduction methods

B. An enzyme biosensor for BPA quantification

(a). Polymerization of a PANI-based nanocomposite from the aniline monomer with fixed amounts of PMMA and TiO_2 nanoparticles, followed by structural, optical, morphological and electrochemical characterization using necessary techniques.

(b). Fabrication of the biosensor system through immobilization of MnP (as an analyte recognition element) onto the PANI-PMMA-TiO_2 nanocomposite platform. Confirmation of enzyme attachment to the nanocomposite was evaluated using cyclic voltammetry.

(c). Investigation of the biosensor feasibility towards BPA quantification using cyclic voltammetry (CV) and square wave voltammetry (SWV).

(d). Application of the biosensor system for detection of BPA using SWV.

.

6. References

1. Liao, J.-R., Zhang, D. & Wu, X.-L. Pulmonary tuberculosis combined with hepatic tuberculosis: a case report and literature review. *Clin. Respir. J.* 9, 501-505 (2014).

2. Tchaou, M., Darre, T., Mossi, K. E. & Sonhaye, L. Extra-Pulmonary Tuberculosis : Retrospective Review of 83 Confirmed Cases , Observed in Radiology in Lomé (TOGO). 6, 49–55 (2016).

3. Yruela, I., Contreras-Moreira, B., Magalhães, C., Osório, N. S. & Gonzalo-Asensio, J. *Mycobacterium tuberculosis* Complex Exhibits Lineage-Specific Variations Affecting Protein Ductility and Epitope Recognition. *Genome Biol. EvoL.* 8(12), 3751-3764 (2017).

4. Clarke, C., Helden, P. Van, Miller, M. & Parsons, S. Animal-adapted members of the Mycobacterium tuberculosis complex endemic to the southern African subregion Dassie bacillus. *J. S. Afr. Vet. Assoc.* 87(1), 1–7 (2016).

5. Nasser, M. All about Mycobacterium simiae in Brief. *J. Med. Microbio Diagnosis*. 4, 1–2 (2014).

6. Malama, S., Munyeme, M., Mwanza, S. & Muma, J. B. Isolation and characterization of non tuberculous mycobacteria from humans and animals in Namwala District of Zambia. *BMC Res. Notes* 7, 622-626 (2014).

7. Mortaz, E., Adcock, I.M., Tabarsi, P., Masjedi, M.R., Mansouri, D., Velayati, A.A., Casanova, J-L & Barnes, P.J. Interaction of Pattern Recognition Receptors with Mycobacterium Tuberculosis. *J. Clin. Immunol.* 35, 1–10 (2015).

8. Lee, S. H. Tuberculosis infection and latent tuberculosis. *Tuberc. Respir. Dis. (Seoul).* 79, 201–206 (2016).

9. Pai, M., Behr, M.A., Dowdy, D., Dheda, K., Divangahi, M., Boehme, C.C., Ginsberg, A., Swaminathan, S., Spigelman, M., Getahun, H., Menzies, D & Raviglione, M. Tuberculosis. *Nat. Rev. Dis. Prim.* 2, 16076 (2016).

10. Borgdorff, M.W., Sebek, M., Geskus, R.B, Kremer K, Kalisvaart N. & van Soolingen D. The incubation period distribution of tuberculosis estimated with a molecular epidemiological approach. *Int. J. Epidemiol.* 40, 964–970 (2011).

11. AL-Harbie, A. M. The Challenges of Tuberculosis Prevention through Early Detection of Latent Tuberculosis Infection in New Immigrants to the State of Kuwait Adel Mohanna. The University of Edinburgh. *Thesis* (2012).

12. Santos, L. C. Review: The Molecular Basis of Resistance in Mycobaterium tuberculosis. *Open J. Med. Microbiol.* 2, 24–36 (2012).

13. D 'ambrosio, L. Centis, R., Sotgiu, G., Pontali, E., Spanevello, A. & Migliori1, G.B. New anti-tuberculosis drugs and regimens: 2015 update. *ERJ. Open Res.* 1, 10–2015 (2015).

14. Ramirez-Lapausa, M., Menendez-Saldana, A. & Noguerado-Asensio, A. Extrapulmonary tuberculosis : an overview. *Rev Esp Sanid Penit.* 17, 3–11 (2015).

15. Vivar, D.E.P., Cruz, Y.J.T. & Villasana, J.E.M. Diagnosis of extra-pulmonary tuberculosis : Systematic analysis of literature and. study of seven cases in the cervicofacial region. *Rev. Odontológica Mex.* 20(4), 258–264 (2016).

16. Smaoui, S. Mezghanni, M.A., Hammami, B., Zalila, N., Marouane, C., Kammoun, S. Ghorbel, A., Jemma, M.B. & Messadi-Akrout, F. Tuberculosis lymphadenitis in a southeastern region in Tunisia: Epidemiology, clinical features, diagnosis and treatment. *Int. J. Mycobacteriology.* 4**,** 196–201 (2015).

17. Philip, N., William, T. & John, D. V. Diagnosis of tuberculous meningitis: Challenges and promises. *Malays. J. Pathol.* 37**,** 1–9 (2015).

18. Hickey, A. J., Gounder, L., Moosa, M.-Y. S. & Drain, P. K. A systematic review of hepatic tuberculosis with considerations in human immunodeficiency virus co-infection. *BMC Infect. Dis.* 15**,** 209-219 (2015).

19. Queiroz, A. & Riley, L. W. Bacterial immunostat: Mycobacterium tuberculosis lipids and

their role in the host immune response. *Rev. Soc. Bras. Med. Trop.* 50**,** 9–18 (2017).

20. Kaufmann, S. H. E. Immunopathology of mycobacterial diseases. *Semin. Immunopathol.* 38, 135–138 (2016).

21. Brighenti, M & Lerm, M. How Mycobacterium tuberculosis Manipulates Innate and Adaptive Immunity – New Views of an Old Topic. (InTechOpen) (2012).

22. NHS, Infection Control Operating Group. Clinical guidelines for Tuberculosis Management in a Hospital Setting . 1-16 (2016).

23. Agarwal, A., Sharma, G. & Jasuja, N. Analysis of Diagnostic Methods and Their Sensitivity Test for Mycobacterium Tuberculosis. *Analysis* 2, 17–27 (2016).

24. Srinivasan, L., Ahlbrand, S. & Briken, V. Interaction of mycobacterium tuberculosis with host cell death pathways. *Cold Spring Harb. Perspect. Med.* 4**,** 1–16 (2014).

25. Soul City. Literature Review of TB in South Africa. 1–89 (2015).

26. Trinh, Q. M., Nguyen, H.L., Do, T.N., Nguyen, V.N., Nguyen, B.H., Nguyen, T.V.A., Sintchenko, V & Marais, B.J.. Tuberculosis and HIV co-infection in Vietnam. *Int. J. Infect. Dis.* 46, 56–60 (2016).

27. Zheng, C., Hu, M. & Gao, F. Diabetes and pulmonary tuberculosis: a global overview with special focus on the situation in Asian countries with high TB-DM burden. *Glob. Health Action* 10, 1-11 (2017).

28. Fletcher, H. A. & Schrager, L. TB vaccine development and the End TB Strategy: Importance and current status. *Trans. R. Soc. Trop. Med. Hyg.* 110**,** 212–218 (2016).

29. Fogel, N. Tuberculosis: A disease without boundaries. *Tuberculosis.* 95, 527–531 (2015).

30. Watkins, R. R., Lemonovich, T. L. & Salata, R. A. An update on the association of vitamin D deficiency with common infectious diseases 1. *Can. J. Physiol. Pharmacol.* 93**,** 363–368 (2015).

31. Martineau, A.R., Jolliffe, D.A., Hooper, R.L., Greenberg, L., Aloia, J.F., Bergman,P.,

Dubnov-Raz, G., Esposito, S., Ganmaa, D., Ginde, A.A., Goodall, E.C., Grant, C.C., Griffiths, C.J., Janssens, W., Laaksi, I., Manaseki-Holland, S., Mauger, D., Murdoch, D.R., Neale, R., Rees, J.R., Simpson Jr, S., Stelmach, I., Kumar, G.T., Urashima, M., & Camargo Jr, C.A. Vitamin D supplementation to prevent acute respiratory infections: systematic review and meta-analysis of individual participant data. *B.M.J.* 71**,** 1-14 (2017).

32. Coussens, A. K.,. Wilkinson, R.J., Hanifac, Y., Nikolayevskyy, V., Elkington, P.T., Islam, K., Timms, P.M., Venton, T.R., Bothamley, G.H., Packe, G.E., Darmalingam, M., Davidson, R.N., Milburn, H.J., Baker, L.V., Barker, R.D., Mein, C.A., Bhaw-Rosun, L., Nuamah, R., Younga, D.B., Drobniewski, F.A., Griffiths, C.J. &. Martineau, A.R. Vitamin D accelerates resolution of inflammatory responses during tuberculosis treatment. *Proc. Natl. Acad. Sci. U. S. A.* 109, 15449–15454 (2012).

33. Selvaraj, P., Harishankar, M. & Afsal, K. Vitamin D: Immuno-modulation and tuberculosis treatment. *Can. J. Physiol. Pharmacol.* 93, 377–384 (2015).

34. Myung-Sang, M., Moon, H. & Sung-Soo, K. Tubercle Bacilli in Spinal Tuberculosis - Morphology, Cell Wall Features, Behaviour and Drugs. *J. Spine*. 4(6), 1-8 (2015).

35. Banuls, A.-L., Sanou, A., Van Anh, N. T. & Godreuil, S. Mycobacterium tuberculosis: ecology and evolution of a human bacterium. *J. Med. Microbiol.* 64**,** 1261–1269 (2015).

36. Druszczyńska, M., Kowalewicz-Kulbat, M., Fol, M., Włodarczyk, M. & Rudnicka, W. Latent M. tuberculosis infection - Pathogenesis, diagnosis, treatment and prevention strategies. *Polish J. Microbiol.* 61, 3–10 (2012).

37. Moon, M.-S., Moon, H. & Kim, S.-S. Tubercle Bacilli in Spinal Tuberculosis - Morphology, Cell Wall Features, Behaviour and Drugs. *J. Spine* 4, 4–11 (2015).

38. Getahun, H., Matteelli, A., Abubakar, I., Aziz, M.A., Baddeley, A., Barreira, D., Boon, S.D., Gutierrez, S.M.B., Bruchfeld, J., Burhan, E., Cavalcante, S., Cedillos, R., Chaisson, R., Chee, C.B., Chesire, L., Corbett, E., Dara, M., Denholm, J., de Vries, G., Falzon, D.,

Ford, N., Gale-Rowe, M., Gilpin, C., Girardi, E., Go, U., Govindasamy, D., Grant, A.D., Grzemska, M., Harris, R., Horsburgh Jr, C.R., Ismayilov, A., Jaramillo, E., Kik, S., Kranzer, K., Lienhardt, C., LoBue, P., Lönnroth, K., Marks, G., Menzies, D., Migliori, G.B., Mosca, D., Mukadi, Y.D., Mwinga, A., Nelson, L., Nishikiori, N., Oordt-Speets, A., Rangaka, M.X., Reis, A., Rotz, L., Sandgren, A., Schepisi, M.S., Schünemann, H.J., Sharma, S.K., Sotgiu, G., Stagg, H.R., R. Sterling, T.R., Tayeb, T., Uplekar, M., van der Werf, M.J., Vandevelde, W., van Kessel, F., van't Hoog, A., Varma, J.K., Vezhnina, N., Voniatis, C., Noordegraaf-Schouten, M.V., Weil, D., Weyer, K., Wilkinson, R.J., Yoshiyama, T., Zellweger, J.P. & Raviglione, M. Management of latent Mycobacterium tuberculosis infection: WHO guidelines for low tuberculosis burden countries. *Eur. Respir. J.* 46, 1563–1576 (2015).

39. Shirvani, F., Karimi, A. & Rajabnejad, M. BCG Vaccination as a Prevention Strategy, Threats and Benefits. *Arch. Pediatr. Infect. Dis.* 4, 1–10 (2016).

40. Roy, A., Eisenhut, M., Harris, R.J., Rodrigues, L.C., Sridha, S., Habermann, S., Snell, L., Mangtani, P., Adetifa, I., Lalvani, A. &Abubakar, I. Effect of BCG vaccination against Mycobacterium tuberculosis infection in children: systematic review and meta-analysis. *BMJ*. 349, 1-11 (2014).

41. Dockrell, H. M. Towards new TB vaccines: what are the challenges? *Pathog. Dis.* 74(4) 1–26 (2016)

42. Tameris, M. D., Hatherill, M., Landry, B.S.,Scriba, T.J., Snowden, M.A., Lockhart, S., Shea, J.E., McClain, J.B., Hussey, G.D., Hanekom, W.A., Mahomed, H. & McShane, H. Safety and efficacy of MVA85A, a new tuberculosis vaccine, in infants previously vaccinated with BCG: A randomised, placebo-controlled phase 2b trial. *The Lancet*. 381, 1021–1028 (2013).

43. Shin, H. J. & Kwon, Y. S. Treatment of drug susceptible pulmonary tuberculosis. *Tuberc.*

Respir. Dis. (Seoul). 78, 161–167 (2015).

44. Kang, H. K., Jeong, B-J., Lee, H., Park, H.Y., Jeon, K., Ki C-S., Lee, N.Y & Koh, W-J. Clinical significance of smear positivity for acid-fast bacilli after ≥5 months of treatment in patients with drug-susceptible pulmonary tuberculosis. *Medicine (Baltimore).* 95(31), 1-7 (2016).

45. Sotgiu, G. Nahid, P., Loddenkemper, R., Abubakar, I., Miravitlles, M. & Migliori, G.B. The ERS-endorsed official ATS/CDC/IDSA clinical practice guidelines on treatment of drug-susceptible tuberculosis. *Eur. Respir. J.* 48, 963–971 (2016).

46. Zumla, A. Rao, M., Parida, S.K., Keshavjee, S., Cassell, G., Wallis, R., Axelsson-Robertsson, R., Doherty, M., Andersson, J. & Maeurer, M.. Inflammation and tuberculosis: Host-directed therapies. *J. Intern. Med.* 277, 373–387 (2015).

47. Agyeman, A. A. & Ofori-Asenso, R. Tuberculosis—an overview. *Public Heal. Emerg.* 1, 37–37 (2016).

48. Nasiruddin, M., Neyaz, M. K. & Das, S. Nanotechnology-Based Approach in Tuberculosis Treatment. *Tuberc. Res. Treat.* 2017, 1-12 (2017).

49. El-muttalut, M. & Khidirelnimeiri, M. Factors contributing to non-compliance with treatment among tuberculosis patients-Kassala. 6**,** 332–338 (2017).

50. Zhang, Y. & Yew, W. Mechanisms of drug resistance in *Mycobacterium tuberculosis. Int J Tuberc Lung Dis.* 13, 1320–1330 (2009).

51. Chapman, H. J. & Lauzardo, M. Advances in diagnosis and treatment of latent tuberculosis infection. *J. Am. Board Fam. Med.* 27**,** 704–12 (2014).

52. Milstein, M.,Lecca, L., Peloquin, C., Mitchison, D., Seung, K., Pagano, M., Coleman, D., Osso, E., Coit, J., Vasquez, D.E.V., Garavito, E.S., Calderon, R., Contreras, C., Davies, G. & . Mitnick. C.D. Evaluation of high-dose rifampin in patients with new, smear-positive tuberculosis (HIRIF): study protocol for a randomized controlled trial. *BMC Infect. Dis.*

16, 453 (2016).

53. Zumla, A., Rao, M., Dodoo, E. & Maeurer, M. Potential of immunomodulatory agents as adjunct host-directed therapies for multidrug-resistant tuberculosis. *BMC Med.* 14, 1–12 (2016).

54. Vilaplana, C., Aklillu, E. & Rao, M. Towards host-directed therapies for tuberculosis. *Nat. Rev. Drug Disc.* 14, 511-512 (2015).

55. Mardani, M. & Abtahian, Z. New Advances in Diagnosis of Latent Tuberculosis Infection: A Review Article. *Arch. Pediatr. Infect. Dis.* 2, 1–9 (2014).

56. Mustafa, A. S. Mycobacterial Diseases The Future of Mycobacterium tuberculosis-Specific Antigens/Peptides in Tuberculin Skin Testing for the Diagnosis of Tuberculosis. *J. Mycobac. Dis.* 4(3) 1–2 (2014).

57. Napoli, C. Ferretti, F., Ninno, F.D., Orioli, R., Marani, A., Sarlo, M.G., Prestigiacomo, C., Luca, A.D., & Orsi, G.B. Screening for Tuberculosis in Health Care Workers : Experience in an Italian Teaching Hospital. *BioMed Res. Int.* 2017, 1-7 (2017).

58. Ryu, Y. J. Diagnosis of pulmonary tuberculosis: Recent advances and diagnostic algorithms. *Tuberc. Respir. Dis. (Seoul).* 78, 64–71 (2015).

59. Wang, S., Inci, F., De Libero, G., Singhal, A. & Demirci, U. Point-of-care assays for tuberculosis: Role of nanotechnology/microfluidics. *Biotechnol. Adv.* 31, 438–449 (2013).

60. Goletti, D., Petruccioli, E., Joosten, S. A. & Ottenhoff, T. H. M. Tuberculosis biomarkers: From diagnosis to protection. *Infect. Dis. Rep.* 8, 24–32 (2016).

61. Rufai, S.B., Singh, S., Singh, A., Kumar, P., Singh, J & Vishal, A. Performance of Xpert MTB/RIF on ascitic fluid samples for detection of abdominal tuberculosis. *J. Lab. Physicians.* 9(1), 45-72 (2017).

62. Nhu, N. T. Q., Heemskerk,D., Thu, D.D.A., Chau, T.T.H., Mai, N.T.H., Nghia, H.D.T., Loc, P.P., Ha, D.T.M., Merson, L., Thinh, T.T.V., Day, J., van Vinh Chau, N., Wolbers,

M., Farrar, J. & Caws, M. Evaluation of genexpert MTB/RIF for diagnosis of tuberculous meningitis. *J. Clin. Microbiol.* 52**,** 226–233 (2014).

63. Nathavitharana, R.R., Cudahy, P.G.T., Schumacher, S.G., Steingart, K.R., Pai, M. & Denkinger, C.M. Accuracy of line probe assays for the diagnosis of pulmonary and multidrug-resistant tuberculosis: a systematic review and meta-analysis. *Eur. Respir. J.* 49, 1-23 (2017).

64. MacLean, E., Huddart, S. & Pai, M. Molecular diagnosis of tuberculosis: we need solutions that span the healthcare value chain. *Expert Rev. Mol. Diagn.* 17**,** 5–7 (2017).

65. Rockwood, N., Wojno J., Ghebrekristos, Y., Nicol, M..P., Meintjes, G., Wilkinson, R.J. Utility of second generation line probe assay (Hain MTBDR *plus*) directly on 2-month sputa specimens to monitor tuberculosis treatment response. *J. Clin. Microbiol.* 55(5), 1508-1515 (2017).

66. Vittor, A. Y., Garland, J. M. & Gilman, R. H. Molecular diagnosis of TB in the HIV positive population. *Ann. Glob. Heal.* 80**,** 476–485 (2014).

67. Knierer, J., Gallegos Morales, E. N., Schablon, A., Nienhaus, A. & Kersten, J. F. QFT-Plus: a plus in variability? -- Evaluation of new generation IGRA in serial testing of students with a migration background in Germany. *J. Occup. Med. Toxicol.* 12, 1–12 (2017).

68. Starke, J. R., Byington, C.L., Maldonado, Y.A., Barnett, E.D., Davies, H.D., Edwards, K.M., Jackson, M.A., Maldonado, Y.A., Murray, D.L., Rathore, M.H., Sawyer, M.H., Schutze, G.E., Willoughby, R.E. & Zaoutis, T.E. Interferon-γ release assays for diagnosis of tuberculosis infection and disease in children. *Pediatrics.* 134(6), 1763–1773 (2014).

69. Chang, P.-C., Wang, P.-H. & Chen, K.-T. Use of the QuantiFERON-TB Gold In-Tube Test in the Diagnosis and Monitoring of Treatment Efficacy in Active Pulmonary Tuberculosis. *Int. J. Environ. Res. Public Health.* 14, 1-10 (2017).

70. Kussen, G. M. B., Dalla-Costa, L. M., Rossoni, A. & Raboni, S. M. Interferon-gamma release assay versus tuberculin skin test for latent tuberculosis infection among HIV patients in Brazil. *Braz. J. Infect. Dis.* 20, 69–75 (2016).

71. Santin, M., García-García, J.M.& Domínguez, J.. Guidelines for the use of interferon-γ release assays in the diagnosis of tuberculosis infection. *Enferm. Infecc. Microbiol. Clin.* 34(5), 1-13 (2016).

72. Pai, M. Denkinger, C.M., Kik, S.V., Rangaka, M.X., Zwerling, A., Oxlade, O., Metcalfe, J.Z., Cattamanchi, A., Dowdy, D.W., Dheda, K. & Banaeih, N. Gamma interferon release assays for detection of Mycobacterium tuberculosis infection. *Clin. Microbiol. Rev.* 27(1), 3–20 (2014).

73. Yan, X., Zhou, C., Yan, Y. & Zhu, Y. A Simple and Renewable Nanoporous Gold-based Electrochemical Sensor for Bisphenol A Detection. *Electroanalysis* 27, 2718–2724 (2015).

74. Park, H-G., Kim, J-Y. & Yeo, M.K. Paper-based Microfluidic for Bisphenol A Based Reaction and Image Analysis. *BioChip J.* 10(1), 25-33 (2016).

75. Armand G, M. K. Correlation between Bisphenol A Exposure and Adverse Health Effects. *Mod. Chem. Appl.* 3, 1–3 (2015).

76. Chen, X., Wang, Y., Xu, F., Wei, X., Zhang, J., Wang, C., Wei, H., Xu, S., Yan, P., Zhou, W., Mody, I., Xu, X. & Wang, Q. The Rapid Effect of Bisphenol-A on Long-Term Potentiation in Hippocampus Involves Estrogen Receptors and ERK Activation. *Neural Plast.* 2017, 1–9 (2017).

77. Rogers, J.A., Metz, L. & Yong, V.W. Endocrine disrupting chemicals and immune responses: A focus on bisphenol-A and its potential mechanisms. *Mol. Immunol*. 53, 421-430 (2013).

78. Wang, Z., Liu, H. & Liu, S. Low-Dose Bisphenol A Exposure: A Seemingly Instigating Carcinogenic Effect on Breast Cancer. *Adv. Sci.* 4(2), 1–14 (2016).

79. Flint, S., Markle, T., Thompson, S. & Wallace, E. Bisphenol A exposure, effects, and policy: A wildlife perspective. *J. Environ. Manage.* 104, 19–34 (2012).

80. 80. Inadera, H. Neurological effects of bisphenol A and its analogues. *Int. J. Med. Sci.* 12, 926–936 (2015).

81. Li, L. Wang, Q., Zhang, Y., Nu, Y., Yao, X. & Liu, H.. The molecular mechanism of bisphenol A (BPA) as an endocrine disruptor by interacting with nuclear receptors: Insights from molecular dynamics (MD) simulations. *PLoS One*. 10(3), 1–18 (2015).

82. Xu, J., Huang, G. & Guo, T. L. Developmental Bisphenol A Exposure Modulates Immune-Related Diseases. *Toxics*. 4, 1-23 (2016).

83. Rochester, J. R. Bisphenol A and human health: A review of the literature. *Reprod. Toxicol.* 42, 132–155 (2013).

84. Clément, F., Xu, X., Donini, C.F., Clément, A., Omarjee, S., Delay, E., Treilleux, I., Fervers, B., Romancer, M.L., Cohen, P.A. & Maguer-Satta1, V. Long-term exposure to bisphenol A or benzo(a)pyrene alters the fate of human mammary epithelial stem cells in response to BMP2 and BMP4, by pre-activating BMP signaling. *Cell Death Differ.* 24(1) 155-166 (2016).

85. Giannandrea, F. & Fargnoli, S. Environmental Factors Affecting Growth and Occurrence of Testicular Cancer in Childhood: An Overview of the Current Epidemiological Evidence. *Children.* 4(1), 1-9 (2017).

86. Gao, X. & Wang, H. S. Impact of bisphenol A on the cardiovascular system - Epidemiological and experimental evidence and molecular mechanisms. *Int. J. Environ. Res. Public Health.* 11, 8399–8413 (2014).

87. Ferguson, A., Penney, R. & Solo-gabriele, H. A Review of the Field on Children's Exposure to Environmental Contaminants: A Risk Assessment Approach. *Int. J. Environ. Res. Public Heal. Rev.* 14, 1–25 (2017).

88. Bodin, J., Bølling, A.K., Becher, R., Kuper, F., Løvik, M. & Nygaard, U.C. Transmaternal Bisphenol A Exposure Accelerates Diabetes Type 1 Development in NOD Mice. *Toxicol. Sci.*.137, 311–323 (2014).

89. Laurenti, P. Raponi, M., de Waure, C., Marino, M., Ricciardi, W. & Damiani, G. Performance of interferon- γ release assays in the diagnosis of confirmed active tuberculosis in immunocompetent children : a new systematic review and meta-analysis. *BMC Infect. Dis.* 16, 1-11 (2016).

90. Takarinda, K. C., Sandy, C., Masuka, N., Hazangwe, P., Choto, R.C., Mutasa-Apollo, T., Nkomo, B., Sibanda, E., Mugurungi, O., Harries, A.D. & Siziba, N. Factors Associated with Mortality among Patients on TB Treatment in the Southern Region of Zimbabwe. *Tuberc. Res. Treatment*.2017, 1-11 (2017).

91. World Health Organization. Global Tuberculosis Report. *WHO*. (2016).

92. Gebrecherkos, T., Gelaw, B. & Tessema, B. Smear positive pulmonary tuberculosis and HIV co-infection in prison settings of North Gondar Zone, Northwest Ethiopia. *BMC Public Health* 16, 1091–1101 (2016).

93. Kalonji, G. M., Connick, G.D., Ngongo, L.O., Nsaka, D.K. Kabengele, T., Kandolo, F.T., Ilunga-Ilunga, F., Adelin, A & Get, D. Prevalence of tuberculosis and associated risk factors in the Central Prison of Mbuji-Mayi, Democratic Republic of Congo. *Trop. Med. Health.* 44, 1-6 (2016).

94. Heunis, J. C., Kigozi, N. G., Chikobvu, P., Botha, S. & Van Rensburg, H. D. Risk factors for mortality in TB patients: A 10-year electronic record review in a South African province. *BMC Public Health.* 17, 1–7 (2017).

95. Statistics South Africa. Mortality and causes of death in South Africa: Findings from death notification. *Stat. release P0309.3* 1–127 (2011).

96. Statistics South Africa. Mortality and causes of death in South Africa: Findings from death

notification, 2014. Statistical release P0309.3. (2015)

97.   Kigozi, G., Heunis, C., Chikobvu, P., Botha, S. & van Rensburg, D. Factors influencing treatment default among tuberculosis patients in a high burden province of South Africa. *Int. J. Infect. Dis.* 54, 95–102 (2017).

98.   World Health Organization. Global tuberculosis report. *(WHO)* (2012).

99.   Lewandowski, C. M., Co-investigator, N. & Lewandowski, C. M. WHO Global tuberculosis report. *Eff. Br. mindfulness Interv. acute pain Exp. An Exam. Individ. Differ.* 1, 1689–1699 (2015).

100.   World Health Organization. Global Tuberculosis Report. *WHO*.(2013).

101.   Shah, N. S. Sara C James C.M. Brust, Barun Mathema, Nazir Ismail, *et al.* Transmission of Extensively Drug-Resistant Tuberculosis in South Africa. *N. Engl. J. Med.* 376, 243–253 (2017).

102.   Department of Correctional Services. Correctional Services Annual Report 2015/2016. (2016).

103.   Telisinghe, L., Fielding, K.L., Malden, J.L., Hanifa, Y., Churchyard, G.J., Grant, A.D., Charalambous, S. High tuberculosis prevalence in a South African prison: The need for routine tuberculosis screening. *PLoS One.* 9, 1-9 (2014).

104.   World Health Organization. Global Report on Diabetes.*WHO*. (2016).

105.   Kapur, A. & Harries, A. D. The double burden of diabetes and tuberculosis - Public health implications. *Diabetes Res. Clin. Pract.* 101, 10–19 (2013).

106.   Yoko, J., Tumbo, J., Mills, A. & Kabongo, C. Characteristics of pulmonary tuberculosis patients in Moses Kotane region North West Province, South Africa. *South African Fam. Pract.* 59(2), 78-81 (2017).

107.   Asati, A., Nayak, S. & Indurkar, M. A study on factors associated with non-adherence to ATT among pulmonary tuberculosis patients under RNTCP. 4, 2759–2763 (2017).

108.   Sharma, R., Deacon, S.E., Nowak, D., George, S.E., Szymonik, M.P., Tang, A.A., Tomlinson, D.C., Davies, A.G., McPherson, M.J. & Wälti, C. Label-free electrochemical impedance biosensor to detect human interleukin-8 in serum with sub-pg/ml sensitivity. *Biosens. Bioelectron.* 80, 607–613 (2016).

109.   Torati, S. R., Reddy, V., Yoon, S. S. & Kim, C. G. Electrochemical biosensor for Mycobacterium tuberculosis DNA detection based on gold nanotubes array electrode platform. *Biosens. Bioelectron.* 78, 483–488 (2016).

110.   Sidwaba, U., Ajayi, R.F., Feleni, U., Douman, S., Baker, P.G., Vilakazi, S.L., Tshikhudo, R. & Iwuoha, E.I. Polyanilino-Carbon Nanotubes Derivatised Cytochrome P450 2E1 Nanobiosensor for the Determination of Pyrazinamide Anti-Tuberculosis Drugs. *Nano Hybrids.* 6, 59–73 (2014).

111.   Wang, Y., Zhang, Y., Wu, D., Ma, H1., Pang, X., Fan, D., Wei, Q. & Du, B. Ultrasensitive Label-free Electrochemical Immunosensor based on Multifunctionalized Graphene Nanocomposites for the Detection of Alpha Fetoprotein. *Sci. Rep.* 7, 1–10 (2017).

112.   Huang, H., Li, J., Shi, S., Yan, Y. & Zhang, M. Detection of Interferon-Gamma for Latent Tuberculosis Diagnosis Using an Immunosensor Based on CdS Quantum Dots Coupled to Magnetic Beads as Labels. 10, 2580–2593 (2015).

113.   Rotherham, L. S., Maserumule, C., Dheda, K., Theron, J. & Khati, M. Selection and Application of ssDNA Aptamers to Detect Active TB from Sputum Samples. *PLoS One*. 7(10), 1–11 (2012).

114.   Oliviero, G., Stornaiuolo, M., Atri, V.D., Nici, F., Yousif, A.M., D'Errico, S., Piccialli, G., Mayol, L., Novellino, E., Marinelli, L., Grieco, P., Carotenuto, A., Noppen, S., Liekens, S., Balzarini, J. & Borbone, N. Screening Platform toward New Anti-HIV Aptamers Set on Molecular Docking and Fluorescence Quenching Techniques. *Anal. Chem.* 88, 2327–2334

(2016).

115.   Mallikaratchy, P., Tang, Z., Kwame, S., Meng, L., Shangguan, D. & Tan, W. Aptamer directly evolved from live cells recognizes membrane bound immunoglobin heavy mu chain in Burkitt's lymphoma cells. *Mol. Cell. Proteomics.* 6, 2230–2238 (2007).

116.   Matsunaga, K.-I., Kimoto, M., Hanson, C., Sanford, M., Young, H.A. & Hirao, I.. Architecture of high-affinity unnatural-base DNA aptamers toward pharmaceutical applications. *Sci. Rep.* 5, 18478 (2015).

117.   Fernández-Sanlés, A. Berzal-Herranz, B., González-Matamala, R., Ríos-Marco, P., Romero-López, C. & Berzal-Herranz, A. RNA aptamers as molecular tools to study the functionality of the Hepatitis C Virus CRE region. *Molecules.* 20, 16030–16047 (2015).

118.   Ding, S., Mosher, C., Lee, X.Y., Das, S.R., Cargill, A.A., Tang, X., Chen, B., McLamore, E.S., Gomes, C., Hostetter, J.M. & Claussen, J.C. Rapid and Label-Free Detection of Interferon Gamma via an Electrochemical Aptasensor Comprising a Ternary Surface Monolayer on a Gold Interdigitated Electrode Array. *ACS Sensors* 2, 210–217 (2017).

119.   Yu, P., Liu, Y., Zhang, X., Zhou, J., Xiong, E., Li, X. & Chen, J. A novel electrochemical aptasensor for bisphenol A assay based on triple-signaling strategy. *Biosens. Bioelectron.* 79**,** 22–28 (2016).

PART 2: LITERATURE REVIEW

Overview

This section is based on literature reviewed during conduction of this project.

Chapter 2, titled 'Poly(3,4-propylenedioxythiophene), derivatives and composites: Properties and applications' reviews and summarizes trends in the synthesis, properties and applications of conducting polymers, with specific reference to poly(3,4-propylenedioxythiophene), its derivatives, its nanocomposites with different nanomaterials and its applications.

UNIVERSITY *of the*
WESTERN CAPE

Chapter 2

Poly(3,4-propylenedioxythiophene), derivatives and composites: Properties and applications

ABSTRACT

Poly(3,4-propylenedioxythiophene) (PProDOT) is a polythiophene- derivatized electrically conducting polymer with interesting optical and electrochemical properties that can be further enhanced by different strategies including substitution of the monomer with or incorporation of different molecules and materials at different sites. Hence, PProDOT has been applied in electrochromic devices, energy storage devices, sensors, memory devices and photocatalysis. This study reviews trends in the synthetic routes, properties displayed by and applications of PProDOT, its derivatives, copolymers and nanocomposites.

KEYWORDS: conducting polymers, polythiophene derivatives, polymer nanocomposites, poly(3,4-propylenedioxythiophene), biosensor

1. Introduction

Conducting polymers (CPs), characterized by the π-conjugation responsible for charge mobility along their backbones, are amongst the most widely studied materials for various applications including biosensors, lithium-ion batteries, supercapacitors, electrochromic devices, bioelectronics and memory devices [120–123]. Conducting polymers exhibit interesting properties such as easy synthesis through a wide range of strategic routes, tuneable conductivity between insulating and conducting metallic states, high optical activity, compatibility with many biomolecules and accessible modification with different material [121,124,125]. This ever-increasing attention towards CPs is also driven by the high demand for high performance devices ranging from electronic displays to energy storage devices and human health-related devices including diagnostics and therapeutics. This demand is catered for by the advances in functionalization of polymers with different materials including nanomaterials and other polymers [126,127], yielding composites with outstanding properties for the desired applications. Structures of the most widely investigated CPs; polypyrrole (PPy), polythiophene (PTh) and polyaniline (PANI) in neutral states, are shown in Figure 2.

Polythiophene (PTh)

Polyaniline (PANI)
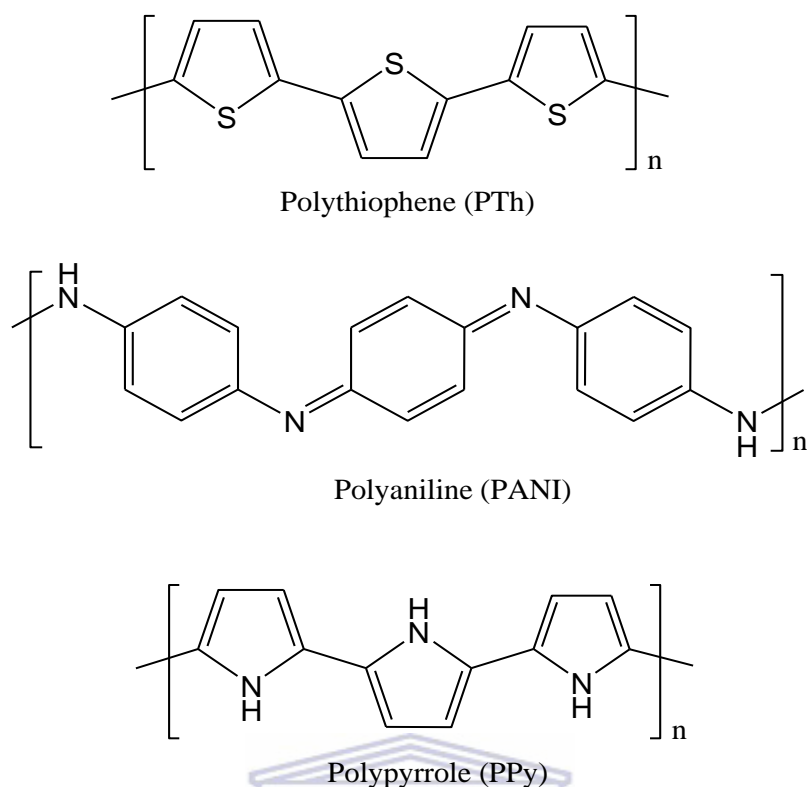
Polypyrrole (PPy)

Figure 2: Chemical structures of polythiophene, polyaniline and polypyrrole in neutral states.

Despite the attractive properties that CPs exhibit, their applications were limited by their instability, insolubility in certain solvents and undesired wide band gaps for photovoltaics applications until the era of their functionalization with different ions, molecules and materials [128,129]. Polythiophene is one of such CPs whose applications had been limited due to its insolubility until it was discovered that substituting the monomer with different molecules or blending with other polythiophenes could tune the different properties [124,130,131]. Hence, substituted polythiophene derivatives, poly(ethylenedixythiophene) (PEDOT) and poly(3,4-propylenedioxythiophene) (PProDOT) which are polythiophene compounds substituted at the 3- and 4- positions (see Figure 3), have predominantly gained potential in many academic and industrial applications.

http://etd.uwc.ac.za
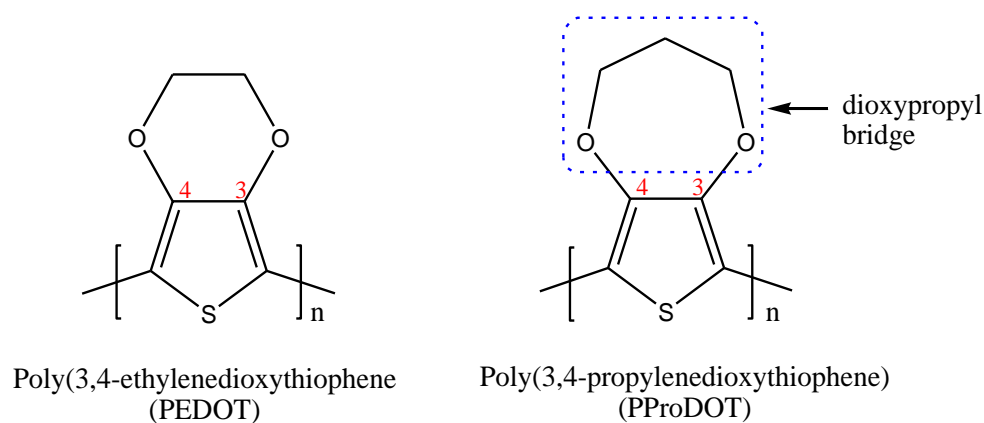
Figure 3: Chemical structures of PEDOT and PProDOT based on repeating monomer units, showing 3- and 4- positions of the polythiophene ring and the dioxypropyl bridge extending the thiophene ring in PProDOT.

2. Poly(3,4-propylenedioxythiophene)

Poly(propylenedioxythiophene) (PProDOT), alongside PEDOT, is a polythiophene derivative whose existence evolved as an addressing measure to the limited applications of polythiophene [132]. Basically, the PProDOT monomer, propylenedioxythiophene (ProDOT) is a thiophene molecule extended with a dioxypropyl bridge at the 3- and 4- positions of the thiophene heterocyclic ring [133,134], as can be seen in Figure 3. PProDOT has found applications in electrochromic devices and supercapacitors, elicited by its environmental stability, low oxidation potentials, high thermal stability, high electrical conductivity and optical activity [135].

3. Polymer growth methods

3.1. Mechanochemical polymerization

This is one of the most applied preparation routes in which polymerization is initiated by an oxidizing agent in a solvent-free solid-state manner [136]. The monomer (and its dopants) and the oxidizing agent, usually ferric chloride ($FeCl_3$), are ground together and PProDOT (and doped-PProDOT) formation is then usually indicated by a distinguishable coloured powder

than the starting material, depending on the doping level and the obtained polymer state. During the grinding (also known as milling), an excess potential energy accompanied by shear and friction forces exerted on the starting material causes defects and changes which lead to a polymer of improved reactivity [137]. Using this method, an irregular sponge-like morphology (revealed by transmission electron microscopy (TEM) and scanning electron microscopy (SEM)) has been evidenced for PProDOT [138].

3.2. Chemical oxidative polymerization

This route uses an oxidizing agent and, sometimes, a catalyst which both act as dopants by forming a charged species residing closely to the opposite charge on the polymer backbone [138,139]. In addition to these, nanomaterials and other polymers are also incorporated into CPs with the aim of enhancing different properties and it is documented that the amount and nature of these dopants greatly affect different properties of CPs, including their morphology, optical activity and electrical conductivity [140,141]. To emphasize the critical role that preparation conditions (nature of oxidising agent, supporting solution, dopants and initial monomer concentration) have on polymer properties (this case refers specifically to morphology), Osman and co-workers obtained an irregular morphology for a PProDOT polymer prepared chemically using ferric chloride from a monomer solution dissolved in chloroform [142]. Using auric chloride as an oxidizing agent and a ProDOT monomer solution in acetonitrile, a rod-like morphology was revealed by SEM while the presence of surfactant, sodium dodecyl sulfate, revealed a globular morphology (authors work in Figure 4).
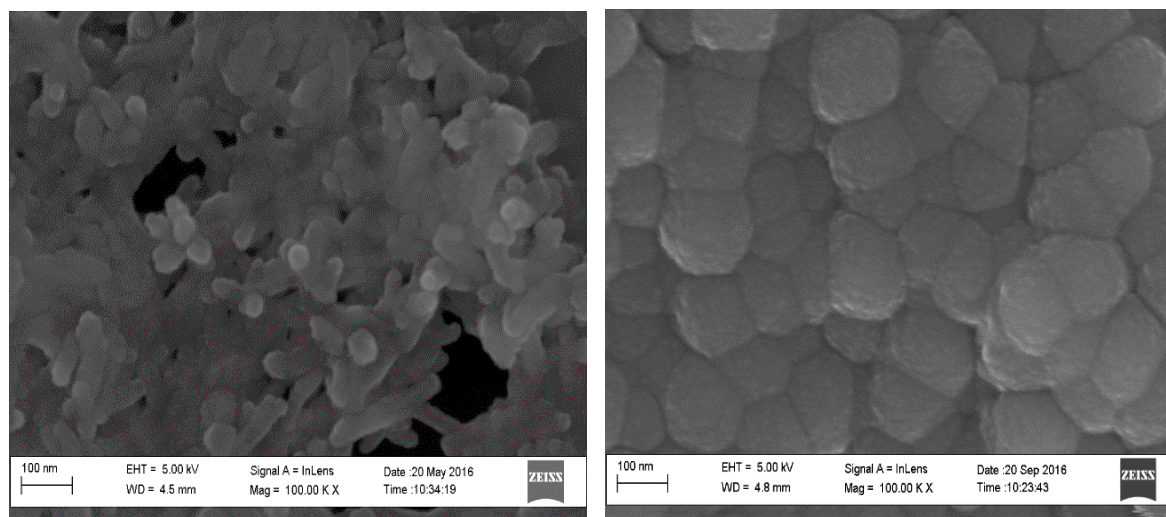
Figure 4: SEM image of PProDOT prepared chemically at room temperature (from a ProDOT monomer solution in acetonitrile) using auric chloride as an oxidizing agent. (A) Surfactant-free PProDOT and (B). Sodium dodecyl sulfate-templated PProDOT.

Besides the possibility of large-scale production which allowed commercialization of various CPs, another advantage of using the chemical polymerization route is the ability to exploit different materials known as templates (categorized as soft templates such as polyanions and surfactants, hard templates such as anodized aluminum oxide and reactive templates such as methyl orange and bovine serum albumin), towards production of nanoscale conducting polymers with specific desired morphologies including spheres, tubes and ribbons [143–27].

3.3. Electrodeposition

There is a wide range of techniques associated with this preparation method including galvanostatic (constant current), potentiodynamic (sweeping potential between specific limits) and potentiostatic techniques (constant potential) [147–149]. The most common and versatile is the potentiodynamic method in which the polymer is grown within a fixed potential range, and polymer growth is monitored through current changes induced by nucleation, oxidation and

reduction processes which yield various polymer structures; one-dimensional (1-D), two-dimensional (2-D) and three-dimensional (3-D) [150,151]. Although the above mentioned techniques can be exploited and optimized to yield the desired polymers and/or polymer composites, the electrochemical deposition method is highly favoured for its ability to directly deposit the polymer onto the substrate of choice (carbon steel, titanium sheets, stainless steel mashes and gold plates), leading to increased adhesion while it also favours environmental benign conditions such as room temperature and use of potential and current instead of the harsh oxidizing agents [143,151,152–155]. Electrodeposition also avoids formation of undesired oligomers as this can be avoided by optimising parameters such as initial polarization and the potential limits. Other parameters that need consideration, towards preparation of desired morphologies, include the number of deposition cycles and scan rate (in the case of potentiodynamic deposition) or deposition time and applied potential (in the case of potentiostatic and galvanostatic methods) for controlled film thickness and polarization necessary for a desired polymer state (reduced or oxidized state) [151,156]. These parameters greatly govern or direct the morphology of the polymer and have a positive effect on the electrical conductivity and mechanical properties of the deposited film. With specific reference to potentiodynamic electrodeposition, the first few cycles of the process are usually different from all other cycles and are characterized by a cross-over loop and a large wave associated with onset oxidation of the monomer. This cross-over loop is associated with nucleation mechanism while the new waves at various potential values, increasing with the number of deposition scans, are associated with polymer growth and its doping/de-doping with the electrolyte anions (depending on the electrolyte solution) [121,149,157].

The major disadvantage of electrochemically deposited polythiophene-based polymers is their poor mechanical stability and poor adhesion onto certain substrates. Some reasons for this poor behaviour include poor interaction between the substrates and the polymers due to

different polarities, mechanical instability which causes the polymer to detach from the substrate as it thickens and dissolution of the polymer in the solvent used in the support electrolyte [143,158,159]. Hence, different strategies such as copolymerization and functionalization of monomers have been invented not only to address the poor adhesion of polymers onto substrates during electrodeposition, but to also enhance all optical, electrochemical and mechanical properties using various methods.

4. Enhancing different properties of PProDOT

Although PProDOT exhibits satisfactory optical properties which led to its application in electrochromic and energy storage devices, much work is ongoing on enhancing its different properties for high performance devices with improved stability and longer life-times. Amongst available strategies for improving these properties, functionalization of the monomer, ProDOT, is the most advanced strategy which has led to a wide range of polymers, made possible by easy exploitation of the propyl molecule (from the dioxypropyl bridge) extending the thiophene-based ring. The following sub-sections discuss some examples of conducted strategies (yielding PProDOT polymers from functionalized or substituted monomers, co-polymers and nanocomposites) and highlights the significant outcomes accomplished.

4.1. Functionalized or substituted PProDOTs

4.1.1. Dimethyl substituted PProDOT

Schwendeman and co-researchers fabricated an electrochromic device based on dimethyl-substituted PProDOT (PProDOT-Me$_2$) (Figure 5(b)) [160]. The PProDOT-Me$_2$ was fabricated as a top layer with the electrochemically complimentary poly[3,6-bis(2-(3,4,ethylenedioxy)thienyl)-N-methylcarbazole] (PBEDOT-NMeCz) as a back layer. The main strategy was based on color switching between the two layers where, when the PProDOT-Me$_2$ was oxidatively doped from its neutral state, the carbazole polymer switched from the oxidized

to a neutral state and vice-versa. The device exhibited improved electrochromic contrasts of 55% in the visible region, 80% in the near-infrared (NIR) region and 50% in the IR region. The device had a switching time of 3 s and exhibited a stability of 10 000 switches with only a 20% loss of the initial contrast over a period of 6 days.

4.1.2. *Sulfonated PProDOT*

Sulfonated PProDOT (PProDOT-sultone) (Figure 5 (a)) was synthesized from a hydroxymethyl-substituted ProDOT monomer (PProDOT-OH) which had been previously shown to easily electropolymerize and exhibit a high contrast [161]. In their study, Jain and co-researchers made use of the free hydroxyl group to introduce a propane sultone molecule through alkylation catalysed by (1,4-diazabicyclo[2.2.2]octane) (DABCO) [162]. The electrochromic device, fabricated with two layers of PProDOT sultone (achieved through the layer-by-layer technique) exhibited coloration and decoloration times of 100 ms and 50 ms, respectively, between light blue and dark purple-blue upon application of different potentials. This color switching, associated with the neutral and oxidized states of the polymer, occurred on only one layer without noticeable degradation or memory effect giving the device an important self-switching character without hinging on a reduction counterpart for switching.

4.1.3. *Acrylated PProDOT*

Acrylated PProDOT (PProDOT-Ac) (Figure 5(c)) with potential application in eyewear and smart windows was developed by Otley and co-researchers [163]. The work was based on improving cycling stability and addressing spotting issues in electrochromic devices caused by defects hypothesized to occur as a result of left-over unpolymerized monomers based on the obtained 0.5% yield after PProDOT-Ac polymerization. They proposed a strategy of interlocking the conjugated polymer and unreacted monomers through photochemical cross-linking into a gel matrix that hindered diffusion of the unpolymerized monomers towards

41

nucleation spots on the counter electrode, thereby avoiding spot formation. Compared to a PProDOT-Me$_2$ device (Figure 5(b)) which showed spotting after 4000 cycles, the PProDOT-Ac device exhibited an exceptional performance of above 10 000 cycles without spots.

(a) PProDOT-sultone   (b) PProDOT-Me$_2$ (c) PProDOT-Ac
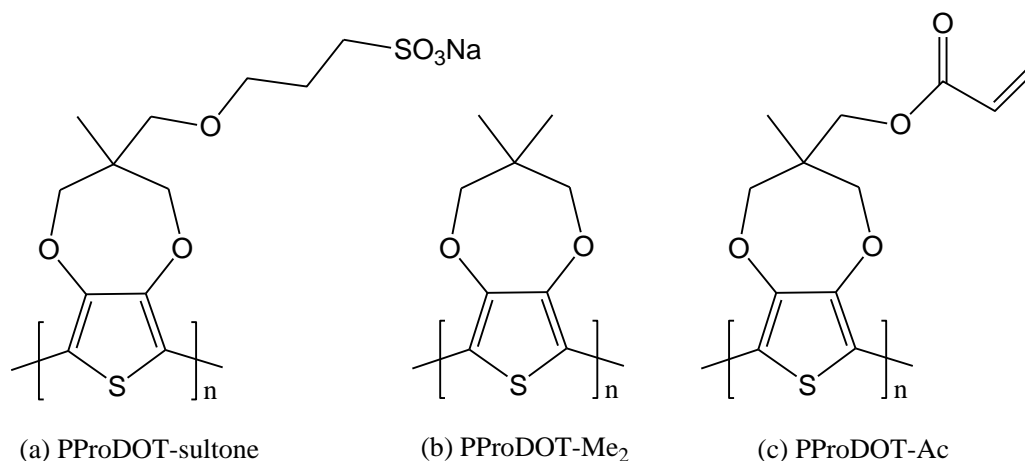
Figure 5: PProDOTs substituted with different molecules. (a) Propyl sulfonated ProDOT (PProDOT-sultone), (b). dimethyl- substituted PProDOT (PProDOT-Me$_2$) and (c) Acrylated PProDOT (PProDOT-Ac).
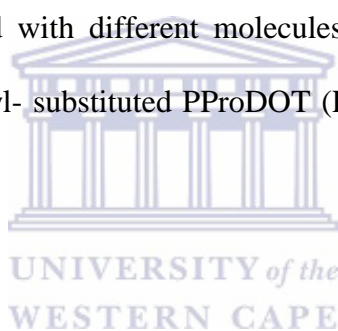
4.2. Bulky branched and linear disubstituted PProDOT

Based on improving different properties such as coloration efficiency, quantum efficiency and electrochromic contrast, Reeves and co-researchers exploited the C$_2$ of the dioxypropyl bridge of ProDOT to synthesise different monomers (Figure 6) by varying the size of the alkylenedioxy ring, the number of constituents and their placement through different reaction mechanisms such as alkylation, etherification, Grignard metathesis and Mitsunobu chemistry [164]. The polymers, based on substituted ProDOT monomer repeating units are shown in Figure 6. The resulting quantum efficiencies were 0.43, 0.38 and 0.4 for PProDOT(EtHx)$_2$, PProDOT(CH$_2$OEtHx)$_2$ and PProDOT(C18), respectively. It was noticed that the quantum efficiencies of PProDOT(CH$_2$OEtHx)$_2$ and PProDOT(C18) films deposited by drop casting (followed by vacuum drying) dramatically dropped when compared to polymers in solution

42

and this behaviour was associated with rapid decay at inter-chain sites. Although PProDOT(C18) showed the best electrochromic behaviour by switching between red and dark-purple at different temperatures, it was impossible to electropolymerize as there was no solvent that could dissolve the monomer and not the polymer. The switching times were found to be independent of structure, except for this long linear polymer which also showed a smaller band gap than the branched polymers. This was associated with limited conjugation in the branched polymers.

(a) PProDOT-(EtHx)$_2$ (c) PProDOT-(C18)$_2$ (b) PProDOT-(CH$_2$OEtHx)$_2$

R: (C18)
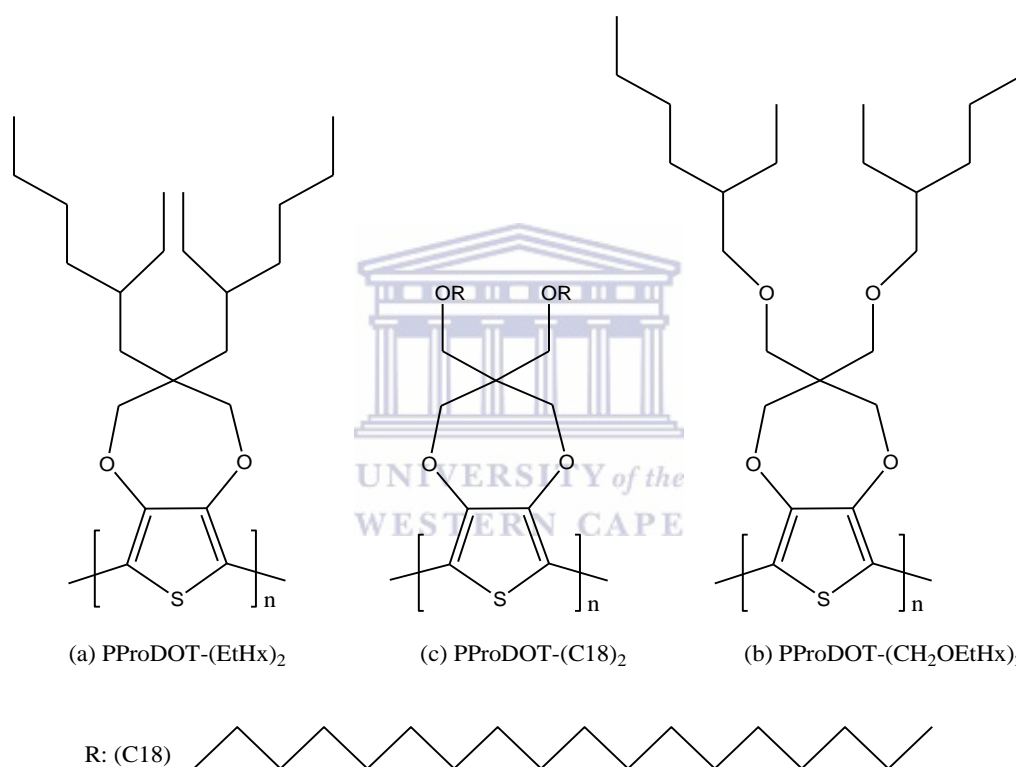
Figure 6: A series of dialkyl-substituted PProDOTs with various branched and linear molecules. Branched substituents: (a) (EtHx)$_2$) and (b) (CH$_2$OEtHx)$_2$). Linear substituents: (c) (C18)$_2$

4.3. PProDOT co-polymers

4.3.1.   Poly(3,4-propylenedioxytiophene-co-N-phenylsulfonyl pyrrole)

In their study, Guler and Sarac investigated the effects of N-phenylsulfone pyrrole (PSP) on PProDOT [133]. They potentiodynamically copolymerized ProDOT and PSP monomers (Figure 7 (a)) onto single carbon fibre microelectrodes (SCFMEs) with varied PSP concentrations. They found that the PSP feed concentration had an effect on the morphology and conductivity of the copolymer. Although they concluded that the substitution of the sulfonyl group in PSP hindered electrochemical polymerization, the copolymer exhibited promising electrochemical properties for potential application in electrochemical biosensors.
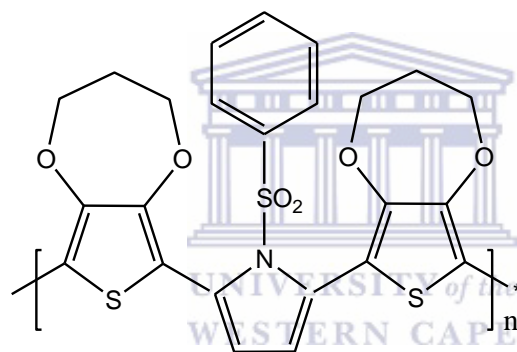
(a) Poly(ProDOT-co-PSP)
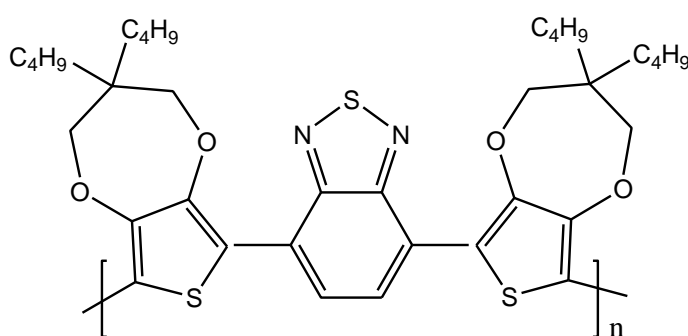
(b) Poly(4,7-bis(3,3-diethyl-3,4-dihydro-2H-thieno[3,4-b][1,4] dioxepin-6-yl)benzo[c][1,2,5]thiadiazole)

Figure 7: Chemical structures of PProDOT co-polymers based on repeating monomer units.

4.3.2. *Poly(5,8-bis(2,3-dihydroxythieno[3,4-b][1,4]dioxin-5-yl)-2,3-dihexy-1quinoxaline)*

It was mentioned earlier that some ProDOT derivatives such as the bulky ProDOT-C18 do not electropolymerize due to solvent difficulties as it is crucial that the solvent/electrolyte does not dissolve the polymer [164]. Li and co-researchers developed a monomer, (5,8-bis(2,3-dihydroxythieno[3,4-b][1,4]dioxin-5-yl)-2,3-dihexy-1quinoxaline) (Figure 7(b)), and potentiodynamically deposited a stable and uniform polymer film from a monomer solution in acetonitrile (in which the polymer was insoluble) with a few drops of dichloromethane (in which the monomer dissolved) [165]. They fabricated an electrochromic device which exhibited an excellent contrast of 80% in the mid-infrared region and a switching time of 1s.

4.4. *Nanocomposites*

4.4.1. *PProDOT-titanium dioxide (TiO$_2$) nanocomposite*

TiO$_2$ nanoparticles are transition metal oxide-based particles with interesting properties such as non-toxicity, biocompatibility, low cost, high optical, photocatalytic activity, luminescent activity and possess antibacterial properties [166–172]. TiO$_2$ has then been incorporated into CPs to improve different electrical (electrical conductivity), optical (refractive index) and mechanical (Young's modulus and hardness) properties [173–175]. Osman and co-researchers [142] incorporated TiO$_2$ nanoparticles into PProDOT and yielded a nanocomposite of highly capacitive behaviour and improved specific capacitance of 219 F·g^{-1}.

4.4.2. *PProDOT-zinc oxide (ZnO) nanocomposite*

Similarly to TiO$_2$, zinc oxide (ZnO) is a transition metal oxide which possesses unique optical, photocatalytic, mechanical and antibacterial properties [176–179]. Different CP properties such as Young's modulus, antibacterial activity, tensile strength and dielectric constants have been improved through incorporation of ZnO nanoparticles [180–182]. A PProDOT nanocomposite

45

with ZnO nanoparticles exhibited a comparable capacitance value of 220 F·g^{-1}, increased electrical conductivity and improved photocatalytic activity towards degradation of methylene blue (MB) dye [183].

4.4.3. PProDOT-gold nanocomposite

Metallic gold nanoparticles (AuNPs) have excellent biocompatibility, high optical activity and electrical conductivity and have found applications in disease diagnosis, drug delivery, biosensors and disease therapy [184–187]. The synergistic effect of AuNPs on the conductivity of PProDOT in neutral pH media is shown in Figure 8 (author's experimental work), where the cyclic voltammogram (CV) of PProDOT shows two broad redox pairs labelled I_1/I_1' (-430 mV/0.0 mV) and II_1'/II_1' (-0.1 mV/0.33 mV), attributed to reduction/oxidation transitions between the polaron and bipolaron states of the polymer, respectively [188]. After incorporation of the AuNPs, a dramatic change is observed in the current peaks, with a two-fold increase for the reduction peaks. Such behaviour is attributed to the synergistic effect of the high surface area and electroactive AuNPs yielding a nanocomposite of improved electrical conductivity and reversibility exhibited by the well-resolved oxidation/reduction pairs I_2/I_2' (-448 mV/160 mV) and II_2'/II_2' (-150 mV/290 mV). CV results for both the PProDOT and PProDOT-AuNP nanocomposite show that reduction peaks I_1 and I_2 do not show any potential shifts with increasing scan rates, a typical behaviour associated with surface-confined and reversible electron transfer reactions [137, 189]. However, it is worth noting that oxidation peak I_1' in the PProDOT film becomes prominent at higher scan rates than lower scan rates, implying that the polaronic state of the polymer prefers fast kinetics.

http://etd.uwc.ac.za
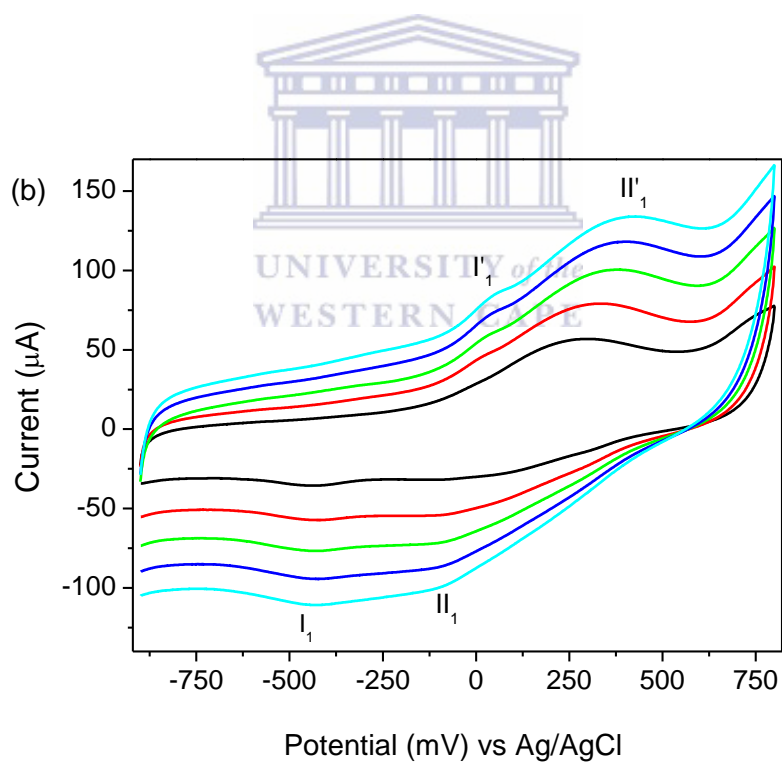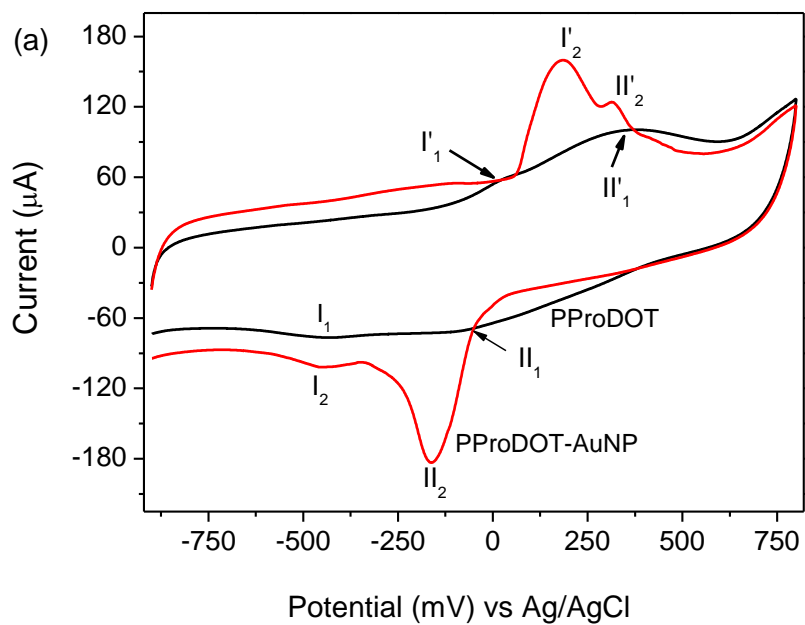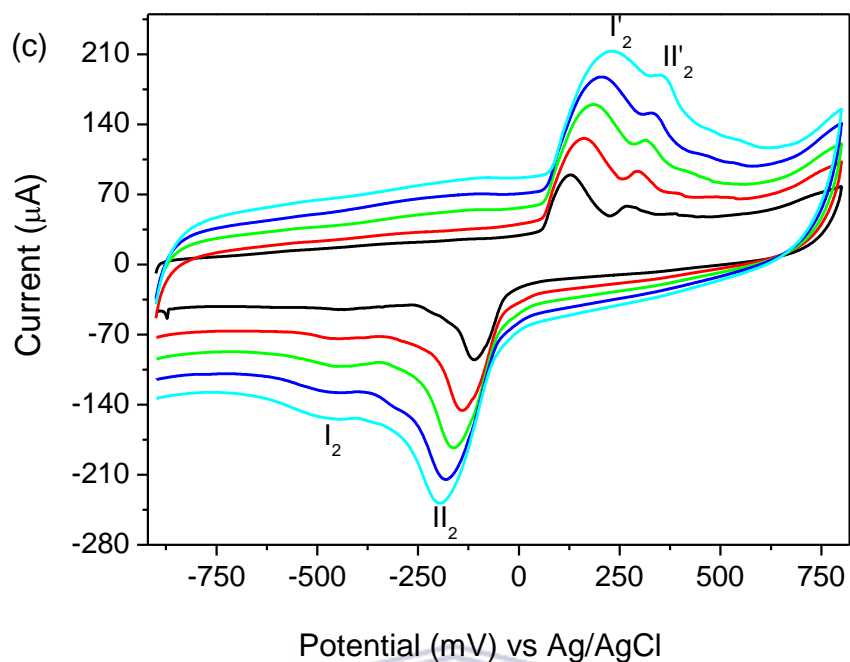
Figure 8: (a) CV graph depicting the synergistic effect of gold nanoparticles on electrical conductivity of PProDOT drop-casted onto screen printed carbon electrodes, recorded at 40 mV/s. CV profiles of (b): PProDOT and (c): PProDOT-AuNPs nanocomposite at incremental scan rates of 20 mV·s^{-1}, from 20 - 100 mV·s^{-1} in increments. Experiments were conducted in 0.1 M LiClO$_4$.

4.4.4. PProDOT-tin oxide nanocomposite

Similarly to ZnO and TiO$_2$, tin oxide (SnO$_2$) is a transition metal oxide semiconducting nanomaterial which has gained vast applications in photocatalysis due to its wide band gap and electron-hole recombinations which are optimized to yield nanomaterials that produce powerful radicals necessary for degradation of various compounds under UV light illumination [190]. In hybrid form with different conducting polymers, SnO$_2$ has been applied in supercapacitors, lithium-ion batteries and gas sensors [191–194]. A PProDOT nanocomposite with

48

SnO_2 showed variable morphologies, stability and capacitive behaviour depending on the amount of SnO_2 and preparation method [195]. Although $PProDOT/SnO_2$ nanocomposites prepared by hand grinding and ball milling exhibited higher specific capacitance (SC) and stability than pure PProDOT, the hand ground PProDOT nanocomposite with 15%wt SnO_2 had the highest SC of 259 F·g^{-1} and a good cycle performance with only 18% loss after 1000 cycles.

5. Applications of PProDOT

5.1. Electrochromic devices

The performance of the electrochromic device (ECD) is determined by the ability of the electrochromic material employed during its fabrication to change optical properties (absorbance, transmittance, reflectance, contrast and luminescence) between transparent (also known as bleached) and coloured states upon insertion or removal of charge from the material while maintaining a stable charge balance on opposite sides of the device during this insertion/removal process induced by application of current, voltage and temperature [164,196–198]. PProDOT has found considerable attention towards preparation of electrochromic devices with proven fast switching times, improved contrast, high transmittance, improved stability and full spectrum transmissions with promising applications in multicolour EC displays [163,199–202].

5.2. Photocatalysis

Organic dyes, produced in large amounts by textile industries, are amongst the most toxic and non-biodegradable water pollutants with adverse effects on both human health and aquatic life. Photocatalytic degradation of these dyes (such as methylene blue, Congo Red and methylene orange) is one of the most effective low cost methods of water treatment, towards assurance of quality safe drinkable water [203–205]. TiO_2 is characterized by high catalytic activity imposed by its ability to form highly reactive radicals induced by UV irradiation and to enhance this

property by avoiding the undesirable electron-hole recombinations, it has been coupled to different materials [206–209]. PProDOT nanocomposites with transition metal oxides ZnO and TiO$_2$ have been shown to exhibit good catalytic activity towards degradation of the toxic dye, methylene blue (MB) with degradation efficiencies of 52% and 90.5%, respectively [138,183].

5.3. Sensors

Sensors cover a wide scope of devices identified according to the signal transduction methods including calorimetry, surface plasmon resonance, amperometry, fluorescence and conductivity for various applications [210–213]. PProDOT, characterized by excellent optical properties within the polythiophene family of polymers, was employed as a surfactant colorimetric sensor due to its ability to switch from purple to blue in a non-ionic surfactant environment and from purple to black in the presence of a cationic surfactant [214]. The surfactants included the widely employed surfactants towards production of highly soluble and nanostructured, oriented and porous polymers; anionic surfactants (sodium dodecyl sulfate (SDS) and sodium dodecyl benzene sulfonate (SDBS)), non-ionic surfactants (Tween 80 and Triton X-100 (TX-100)) and cationic surfactants (cetyltrimethylammonium bromide (CTAB) and cetylpyridinium chloride (CPyC).

Although electrochemical characterizations pinpoint the potential use of PProDOT in electrochemical biosensors, little has been published on this field. To investigate biosensing feasibility of PProDOT, the PProDOT-gold nanocomposite (section 4.4.3) was applied in fabrication of a biosensor system for detection of bisphenol A (BPA), a chemical associated with environmental pollution and harmful effects on human health. The biosensor system was completed by immobilization of the enzyme manganese peroxidase (MnP), followed by its preliminary application towards BPA quantification using square wave voltammetry (SWV) and the corresponding results are shown in Figure 9.
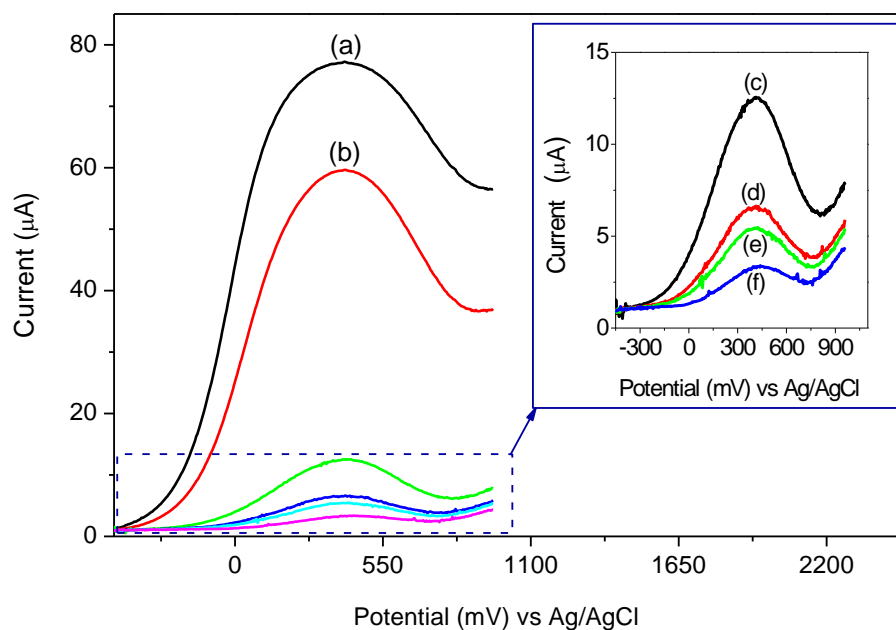
Figure 9: SWV graphs for the PProDOT-gold nanocomposite and the fabricated manganese peroxidase (MnP) biosensor response during BPA detection. (a): The electrochemical behaviour of the PProDOT-gold nanocomposite revealing an oxidation peak at 407 mV (vs Ag/AgCl), (b):confirmation of MnP attachment is depicted by a decrease in peak current and (c) – (f): current response profiles of the biosensor system during detection of BPA. Decreasing peak current values correspond to BPA concentrations of (c) 2 nM, (d) 10 nM, (e) 15 nM and (f) 30 nM. Experiments were performed in 0.1 M phosphate buffer solution (pH 7.4) at an amplitude of 30 mV and a frequency of 4 Hz.

.

The SWV graph of the nanocomposite reveals a peak observed at 407 mV (vs Ag/AgCl) with a maximum current response of 77 µA. This peak is associated with oxidation of the nanocomposite. During biosensor fabrication, MnP attachment onto the nanocomposite was monitored and confirmed by the observable decrease in peak current to 59 µA. In the presence

51

of BPA, further decrease in peak currents with increasing BPA concentrations is observed and this is accompanied by potential shifts towards more positive values implying ability of the biosensor to catalytically oxidize BPA.

5.4. Energy storage devices

The key requirements for high performance *supercapacitors*, which are devices that store energy in an electric double-layer between the electrolyte and the electrode, include improved cycling stability over a wide range of potential, high specific capacitance, high stability in the electrolyte, faster ion diffusion during charge-discharge cycling, thermal stability at different working temperatures and high energy density determined by the electrode material used [215–217]. Amongst various materials, CPs and other carbon-based material have been used as cathode materials due to their redox activity essential for ion intercalation/de-intercalation during charge/discharge, high surface area associated with high capacitance and porosity which facilitates ion diffusion [218,219]. Supercapacitor devices based on PProODT were fabricated and shown to degrade in ethyl methyl imidazolium bis(trifluoromethanesulfonylimide) (EMIBTI) ionic liquid-based electrolyte and this phenomenon was associated with irreversible oxidation of PProDOT at high potentials [220]. Most importantly, it was proven that the presence of impurities in the EMIBTI used during polymer growth and as an electrolyte had a great effect on the performance of the device. The device fabricated on PProDOT deposited from purified EMIBTI tolerated higher voltage operations and retained 93% of its initial capacity after 10 000 cycles while the device fabricated from un-purified EMIBTI retained only 53% of its initial capacity after the 10 000 cycles. A photo-supercapacitor based on diethylene-substituted PProDOT (PProDOT-Et$_2$) exhibited a specific capacitance of 0.48 F cm^{-2}, energy density of 22 Wh cm^{-2}, a power density of 0.6 mW cm^{-2} and an energy storage efficiency of 0.6% while providing a photocharge voltage of 0.75 V, suitable for electronic devices [221].

Interestingly, a device employing technologies from electrochromics and dye-sensitized solar cells was fabricated by Amasawa and co-researchers [222]. The device exhibited high cyclic stability with an electrochromic switching time of 1s, 4.5% conversion efficiency, 34% transmittance and only 3% degradation after 5000 cycles. A polymeric matrix of sodium alginate (SA) and PProOT was also fabricated into a battery which exhibited a better binding strength associated with a longer lifetime, improved Young's and strength modulus and maintained a specific capacitance of 170 mAh g^{-1} at over 400 cycles [223].

6. Conclusion

Conducting polymers exhibit interesting properties desirable for applications in a wide range of devices including electronic displays, sensors, biomedical electronics and energy storage devices. The increasing demand for high performance of these devices, stipulated by factors such as the alarming global energy consumption, exponentially growing cases of different diseases and environmental pollution gave conducting polymers the visible attention they have, up to today, as they have credential potential of producing devices that address these needs.

Due to the high demand for high performance devices, the different strategies of improving the properties of conducting polymers for the desired applications have been conducted. PProDOT, amongst these conducting polymers, is produced through various techniques including mechanochemical polymerization, electrodeposition and chemical polymerization. The special dioxypropyl group of the ProDOT monomer allows easy functionalization through the middle carbon element of the propyl group while the sulfur element of the thiophene ring can form bonds with gold surfaces or groups. These together yield polymers, composites, co-polymers, nanocomposites and fabricated devices of outstanding properties and performance.

Although intensive research has been conducted on development of strategies aimed at enhancing different properties of PProDOT, little has been headed towards its applications in sensors. In fact, the scarcity of reported work on PProDOT application in sensors motivated our group to investigate and prove potential application of PProDOT in electrochemical biosensors. By fabricating a manganese peroxidase biosensor for detection of BPA. A vast amount of research has focussed on application of PProDOT in (a) photocatalytic devices with an ability to degrade environmentally toxic dyes with good efficiency, (b) detection of surfactants which, despite their potential use as dopants and addressing measures towards production of highly processable polymers, become toxic when released to the environment, (c) electrochromic devices that could essentially prompt end-users about food expiration under different storage conditions and (d) highly stable energy storage devices that can tolerate different conditions such as voltage and temperature. Different research studies have reported on the potential characteristics of PProDOT for use in biosensor applications and, therefore, it can be concluded that taking advantage of the current functionalization trends and integration techniques will open doors for its biosensor applications, following the fact that PProDOT has recently gained application in biomedical applications.

7. References

120.   Ying, L., Huang, F., Bazan, G. C., Janssen, R. A. J. & Gundlach, D. J. Regioregular narrow-bandgap-conjugated polymers for plastic electronics. *Nat. Commun.* 8, 14047 (2017).

121.   Nguyen, D. N. & Yoon, H. Recent advances in nanostructured conducting polymers: From synthesis to practical applications. *Polymers.* 8, 1-38 (2016).

122.   Mawad, D., Mansfield, C., Lauto, A., Perbellini, F., Nelson, G.W., Tonkin, J., Bello, S.O., Carrad, D.J., Micolich, A.P., Mahat, M.M., Furman, J., Payne, D.J., Lyon, A.R., Gooding, J.J., Harding, S.E., Terracciano, C.M. & Stevens, M.M. A conducting polymer with enhanced electronic stability applied in cardiac models. *Sci. Adv*. 2, 1-13 (2016)

123.   Yen, H-J., Shan, C., Wang, L Xu, P., Zhou, M & Wang, H-L. Development of Conjugated Polymers for Memory Device Applications. *Polymers (Basel).* 9, 1-16 (2017).

124.   Cho, W., Im, S., Kim, S., Kim, S. & Kim, J. Synthesis and Characterization of PEDOT:P(SS-co-VTMS) with Hydrophobic Properties and Excellent Thermal Stability. *Polymers.* 8, 1-11 (2016).

125.   Zhou, Q. & Shi, G. Conducting Polymer-Based Catalysts. *J. Am. Chem. Soc.* 138, 2868–2876 (2016).

126.   Zhao, Q., Jamal, R., Zhang, L., Wang, M. & Abdiryim, T. The structure and properties of PEDOT synthesized by template-free solution method. *Nanoscale Res. Lett.* 9, 1-9 (2014).

127.   Hackett, A. J., Malmström, J. & Travas-Sejdic, J. Functionalization of Conducting Polymers for Biointerface Applications. *Prog. Polym. Sci.* 70, 18-33 (2017).

128.   Park, C.S., Lee, C. & Kwon, O.S. Conducting Polymer Based Nanobiosensors. Polymers. 8, 1-18 (2016).

129.   Zhao, Y., Cao, L., Li, L., Cheng, W., Xu, L., Ping, X., Pan, L. & Shi, Y. Conducting

polymers and their applications in diabetes management. *Sensors (Switzerland)* 16, 1–14 (2016).

130.   Balint, R., Cassidy, N. J. & Cartmell, S. H. Conductive polymers: Towards a smart biomaterial for tissue engineering. *Acta Biomater.* 10, 2341–2353 (2014).

131.   Kumar, R., Singh, S. & Yadav, B. C. Conducting Polymers : Synthesis , Properties and Applications. 2, 595–604 (2015).

132.   Valderrama-Garcia, B. X., Rodriguez-Alba, E., Morales-Espinoza, E.G., Chane-Ching, K.M. & Rivera, E. Synthesis and characterization of novel polythiophenes containing pyrene chromophores: Thermal, optical and electrochemical properties. *Molecules.* 21, 1-18 (2016).

133.   Gule, F. G. & Sarac, A. S. Electrochemical synthesis of poly[3, 4-Propylenedioxythiophene-co-N-Phenylsulfonyl pyrrole]: Morphological, electrochemical and spectroscopic characterization. *Express Polym. Lett.* 5, 493–505 (2011).

134.   Kumar, A. & Kumar, A. Single step reductive polymerization of functional 3,4-propylenedioxythiophenes via direct C-H arylation catalyzed by palladium acetate. *Polym. Chem.* 1, 286–288 (2010).

135.   Krishnamoorthy, K., Ambade, A. V, Kanungo, M., Contractor, A. Q. & Kumar, A. Rational design of an electrochromic polymer with high contrast in the visible region: dibenzyl substituted poly(3{,}4-propylenedioxythiophene). *J. Mater. Chem.* 11, 2909–2911 (2001).

136.   Xu, C., De, S., Balu, A. M., Ojeda, M. & Luque, R. Mechanochemical synthesis of advanced nanomaterials for catalytic applications. *Chem. Commun.* 51, 6698–6713 (2015).

137.   Brownson, D. A. C. & Banks, C. E. *Interpreting Electrochemistry*. (2014).

138.   Jamal, R., Osman, Y., Rahman, A., Ali, A., Zhang, Y. & Abdiryim, T. Solid-State Synthesis and Photocatalytic Activity of Polyterthiophene Derivatives/TiO$_2$

Nanocomposites. 7, 3786–3801 (2014).

139.   Aronggaowa, B., Toda, Y., Ito, N., Shikinaka, K. & Shimomura, T. Transparent conductive films fabricated from polythiophene nanofibers composited with conventional polymers. *Polymers.* 5, 1325–1338 (2013).

140.   Hu, W., Chen, S., Yang, Z., Liu, L. & Wang, H. Flexible Electrically Conductive Nanocomposite Membrane Based on Bacterial Cellulose and Polyaniline Flexible Electrically Conductive Nanocomposite Membrane Based on Bacterial Cellulose and Polyaniline. 9, 8453–8457 (2011).

141.   Wu, K. H., Ting, T. H., Wang, G. P., Ho, W. D. & Shih, C. C. Effect of carbon black content on electrical and microwave absorbing properties of polyaniline/carbon black nanocomposites. *Polym. Degrad. Stab.* 93, 483–488 (2008).

142.   Osman, Y., Jamal, R., Adalet, R., Xu, F., Ahmat, A. & Tursun, A. Comparative study on poly(3,4-propylenedioxythiophene)/TiO$_2$ nanocomposites synthesized by mechanochemical and chemical solution methods. *Synth. Met.* 179, 54–59 (2013).

143.   Ouyang, L., Wei, B., Kuo, C-C., Pathak, S., Farell, B. & Martin, D.C. Enhanced PEDOT adhesion on solid substrates with electrografted P(EDOT-NH$_2$). 3(3), 1–12 (2017).

144.   Šetka, M., Drbohlavová, J. & Hubálek, J. Nanostructured Polypyrrole-Based Ammonia and Volatile Organic Compound Sensors. *Sensors* 17(3), 1-28 (2017).

145.   Xie, Y., Kocaefe, D., Chen, C. & Kocaefe, Y. Review of Research on Template Methods in Preparation of Nanomaterials. *J. Nanomater.* 2016, 1-10 (2016).

146.   Yang, X., Zhu, Z., Dai, T. & Lu, Y. Facile fabrication of functional polypyrrole nanotubes via a reactive self-degraded template. *Macromol. Rapid Commun.* 26, 1736–1740 (2005).

147.   Song, Y., Guo, Z., Hu, Z., Wang, J. & Jiao, S. Electrochemical self-assembly of nano-polyaniline film by forced convection and its capacitive performance. *RSC Adv.* 7, 3879–

3887 (2017).

148.   Liu, C., Cai, Z., Zhao, Y., Zhao, H. & Ge, F. Potentiostatically synthesized flexible polypyrrole/multi-wall carbon nanotube/cotton fabric electrodes for supercapacitors. *Cellulose.* 23, 637–648 (2016).

149.   Bozzini, B., Bocchetta, P., Kourousias, G. & Gianoncelli, A. Electrodeposition of Mn-Co / polypyrrole nanocomposites : an electrochemical and in situ soft-X ray microspectroscopic investigation. 9(1) 1–23 (2016).

150.   Kondratiev, V. V, Malev, V. V & Eliseeva, S. N. Composite electrode materials based on conducting polymers loaded with metal nanostructures. *Russ. Chem. Rev.* 85, 14–37 (2016).

151.   Gvozdenovic, M., Jugovic, B., Stevanovic, J. & Grgur, B. Electrochemical synthesis of electroconducting polymers. *Hem. Ind.* 68, 673–684 (2014).

152.   Wang, J., Wen, Z., Zi, Y., Lin, L., Wu, C., Guo, H., Xi, Y., Xu, Y. & Wang, Z.L. Self-Powered Electrochemical Synthesis of Polypyrrole from the Pulsed Output of a Triboelectric Nanogenerator as a Sustainable Energy System. *Adv. Funct. Mater.* 26, 3542–3548 (2016).

153.   Liu, B. Enhanced Corrosion Protection of Polypyrrole Coatings on Carbon Steel via Electrodeposition. *Int. J. Electrochem. Sci.* 12, 994–1003 (2017).

154.   Darmanin, T. & Guittard, F. Templateless electrodeposition of conducting polymer nanotubes on mesh substrates for high water adhesion. *Nano-Structures and Nano-Objects.* 7, 64–68 (2016).

155.   El-Maiss, J., Darmanin, T. & Guittard, F. Controlling electrodeposited conducting polymer nanostructures with the number and the length of fluorinated chains for adjusting superhydrophobic properties and adhesion. *RSC Adv.* 5, 37196–37205 (2015).

156.   Ansari, R. Polypyrrole Conducting Electroactive Polymers: Synthesis and Stability

Studies. *CODEN ECJHAO E-Journal Chem.* 3, 973–4945 (2006).

157.   El-Abdallah, G. M. Electrochemical characterization of poly 3-thiopheneacetonitrile: Technique, solvent and relaxation effects. *J. Saudi Chem. Soc.* **1**8, 825–834 (2014).

158.   Yun, S., Lund, P. D. & Hinsch, A. Stability assessment of alternative platinum free counter electrodes for dye-sensitized solar cells. *Energy Environ. Sci.* 8, 3495–3514 (2015).

159.   Xu, F., Ren, S. & Gu, Y. A novel conductive poly (3, 4-ethylenedioxythiophene)-BSA film for the construction of a durable HRP biosensor modified with NanoAu particles. *Sensors.* 16, 10–13 (2016).

160.   Schwendeman, I., Hwang, J., Welsh, D. M., Tanner, D. B. & Reynolds, J. R. Combined visible and infrared electrochromism using dual polymer devices. *Adv. Mater.* 13, 634–637 (2001).

161.   Mishra, S. P., Krishnamoorthy, K., Sahoo, R. & Kumar, A. Synthesis and characterization of monosubstituted and disubstituted poly(3,4-propylenedioxythiophene) derivatives with high electrochromic contrast in the visible region. *J. Polym. Sci. Part A Polym. Chem.* 43, 419–428 (2005).

162.   Jain, V., Sahoo, R., Mishra, S.P., Sinha, J., Montazami, R., Yochum, H.M., Heflin, J.R. & Kumar, A. Synthesis and characterization of regioregular water-soluble 3,4-propylenedioxythiophene derivative and its application in the fabrication of high-contrast solid-state Electrochromic devices. *Macromolecules* 42, 135–140 (2009).

163.   Otley, M. T., Alamer, F.A., Zhu, Y., Singhaviranon, A., Zhang, X., Li, M., Kumar, A. & Sotzing, G.A. Acrylated poly(3,4-propylenedioxythiophene) for enhancement of lifetime and optical properties for single-layer electrochromic devices. *ACS Appl. Mater. Interfaces.* 6, 1734–1739 (2014).

164.   Reeves, B. D., Grenier, C.R.G., Argun, A.A., Cirpan, A., McCarley, T.D. & Reynolds, J.R.. Spray coatable electrochromic dioxythiophene polymers with high coloration

efficiencies. *Macromolecules.* 37, 7559–7569 (2004).

165.   Li, Z., Liu, S. & Liu, D. Electropolymerizable Conjugated Polymers with High Contrast in Infrared Region. 2(4), 152–158 (2012).

166.   Wang, J., Wang, L. & Fan, Y. Adverse biological effect of TiO_2 and hydroxyapatite nanoparticles used in bone repair and replacement. *Int. J. Mol. Sci.* 17, 1–14 (2016).

167.   Lan, M. Y., Liu, C. P., Huang, H. H. & Lee, S. W. Both Enhanced Biocompatibility and Antibacterial Activity in Ag-Decorated TiO_2 Nanotubes. *PLoS One.* 8, 4–11 (2013).

168.   Tayeb, A. M. & Hussein, D. S. Synthesis of TiO_2 Nanoparticles and Their Photocatalytic Activity for Methylene Blue. *Amer. J. Nanomat..* 3(2), 57–63 (2015).

169.   Chaudhari, S., Shaikh, T. & Pandey, P. Review on Polymer TiO_2 Nanocomposites. *Int. J. Eng. Res. Appl.* 3(5), 1386–1391 (2013).

170.   Lin, X., Li, J., Ma, S., Liu, G., Yang, K., Tong, M. & Lin, D. Toxicity of TiO_2 nanoparticles to Escherichia coli: effects of particle size, crystal phase and water chemistry. *PLoS One.* 9(10), 1-8 (2014).

171.   Ahmad, R. & MeryamSardar. TiO_2 nanoparticles as an antibacterial agents against E. coli. *Int. J. Innov. Res. Sci. Eng. Technol.* 2, 3569–3574 (2013).

172.   Khalid, N.S., Fazli, F.I.M., Hamed, N.K.A., Napi, M.L.M., Fhong, S.C. & Ahmad, M.K. Biocompatibility of TiO_2 Nanorods and Nanoparticles on HeLa Cells. *Sains Malays*.45, 1675–1678 (2016).

173.   Liaqat, F.,Tahir, M.N., Schechtel, E., Kappl, M., Auernhammer, G.K.,Char, K., Zentel, R., Butt, H.J. & Tremel, W. High-Performance TiO_2 Nanoparticle/DOPA-Polymer Composites. *Macromol. Rapid Commun.* 36(11), 1129-1137 (2015). doi:10.1002/marc.201400706

174.   Liu, Y., Sun, D., Askari, S., Patel, J., Macias-Montero, M., Mitra, S., Zhang, R., Lin, W.F., Mariotti, D. & Maguire, P. Enhanced Dispersion of TiO_2 Nanoparticles in a

TiO₂/PEDOT:PSS Hybrid Nanocomposite via Plasma-Liquid Interactions. *Sci. Rep.* 5, 1-11 (2015).

175.   Guo, Q., Ghadiri, R., Weigel, T., Aumann, A., Guverich, E.L., Esen, C., Medenbach, O., Cheng, W., Chichkov, B. & Osterndorf, A. Comparison of in situ and ex situ methods for synthesis of two-photon polymerization polymer nanocomposites. *Polymers.* 6, 2037–2050 (2014).

176.   Mote, V. D., Purushotham, Y., Shinde, R. S., Salunke, S. D. & Dole, B. N. Structural, optical and antibacterial properties of yttrium doped ZnO nanoparticles. *Ceramica.* 61, 457–461 (2015).

177.   Thirumavalavan, M., Huang, K.-L. & Lee, J.-F. Preparation and Morphology Studies of Nano Zinc Oxide Obtained Using Native and Modified Chitosans. *Materials.* 6, 4198–4212 (2013).

178.   Kakhaki, Z. M., Youzbashi, A. & Naderi, N. Optical Properties of Zinc Oxide Nanoparticles Prepared by a One- Step Mechanochemical Synthesis Method. *J. Phys.Sci.* 26(2), 41–51 (2015).

179.   Bharti, D. B. & Bharati, A. V. Synthesis of ZnO nanoparticles using a hydrothermal method and a study its optical activity. *Luminescence.* 32, 317–320 (2017).

180.   Samzadeh-kermani, A., Mirzaee, M. & Ghaffari-moghaddam, M. Polyvinyl Alcohol / Polyaniline/ZnO Nanocomposite : Synthesis , Characterization and Bactericidal Property. *Adv. Bio. Chem.* 6, 1–11 (2016).

181.   Díez-Pascual , A.M. & Díez-Vicente, A.L., Poly(3-hydroxybutyrate)/ZnO bionanocomposites with improved mechanical, barrier and antibacterial properties. *Int. J. Mol. Sci.* 15(6), 10950–10973 (2014).

182.   Vaishnav, D. & Goyal, R. K. Thermal and Dielectric Properties of High Performance Polymer/ZnO Nanocomposites. *IOP Conf. Ser. Mater. Sci. Eng.* 64, 1-11 (2014).

183.   Ali, A., Jamal, R., Shao, W., Rahman, A., Osman, Y. & Abdiryim, T. Structure and properties of solid-state synthesized poly(3,4-propylenedioxythiophene)/nano-ZnO composite. *Prog. Nat. Sci. Mater. Int.* 23, 524–531 (2013).

184.   Huang, X., O'Connor, R. & Kwizera, E. A. Gold Nanoparticle Based Platforms for Circulating Cancer Marker Detection. *Nanotheranostics* 1, 80–102 (2017).

185.   Sett, A., Gadewar, M., Sharma, P., Deka, M. & Bora, U. Green synthesis of gold nanoparticles using aqueous extract of Dillenia indica. *Adv. Nat. Sci. Nanosci. Nanotechnol.* **7,** 1–7 (2016).

186.   Unser, S., Holcomb, S. & Sagle, L. Collagen-Gold Nanoparticle Conjugates for Versatile Biosensing. *Sensors.* 17, 378 (2017).

187.   Zhou, W., Gao, X., Liu, D. & Chen, X. Gold Nanoparticles for In Vitro Diagnostics. *Chem. Rev.* 115, 10575–10636 (2015).

188.   Wei, B., Ouyang, L., Liu, J. & Martin, D. C. Post-polymerization functionalization of poly(3,4-propylenedioxythiophene) (PProDOT) via thiol–ene 'click' chemistry. *J. Mater. Chem. B.* 3, 5028–5034 (2015).

189.   Masikini, M., Mailu, S.N., Tsegaye, A., Ikpo, C.O., Njomo, N., Waryo, T.T., Baker, P.G.L. & Iwuoha, E.I. In -situ Electrochemical Synthesis, Microscopic and Spectroscopic Characterisations of Electroactive poly(2,5- dimethoxyaniline) – Multi-Walled Carbon Nanotubes Composite Films in Neutral Media. *Int. J. Electrochem. Sci* 9, 7003–7020 (2014).

190.   He, Z. & Zhou, J. Synthesis, Characterization, and Activity of Tin Oxide Nanoparticles: Influence of Solvothermal Time on Photocatalytic Degradation of Rhodamine B. *Mod. Res. Catal.* 2, 13–18 (2013).

191.   Liu, M., Zhou, D., Jiang, H.R., Ren, Y.X., Kang, F.Y. & Zhao, T.S. A highly-safe lithium-ion sulfur polymer battery with SnO2 anode and acrylate-based gel polymer

electrolyte. *Nano Energy.* 28, 97–105 (2016).

192.   J. Sharma, H., A. Salorkar, M. & B. Kondawar, S. H_2 and CO gas sensor from SnO_2/polyaniline composite nanofibers fabricated by electrospinning. *Adv. Mater. Proc.* 2, 61–66 (2016).

193.   Zou, B., Gong, S., Wang, Y. & Liu, X. Tungsten oxide and polyaniline composite fabricated by surfactant-templated electrodeposition and its use in supercapacitors. *J. Nanomater.* 2014, 1-9 (2014).

194.   Sher Shah, M. S. A., Muhammad, S., Park, J. H., Yoon, W.-S. & Yoo, P. J. Incorporation of PEDOT:PSS into SnO_2/reduced graphene oxide nanocomposite anodes for lithium-ion batteries to achieve ultra-high capacity and cyclic stability. *RSC Adv.* 5, 13964–13971 (2015).

195.   Zhang, L., Jamal, R., Zhao, Q., Zhang, Y., Wang, M & Abdiryim, T. The structure and electrochemical properties of poly(3,4-propylenedioxythiophene)/SnO_2 nanocomposites synthesized by mechanochemical route. *Polym. Compos.* 37**,** 2884–2896 (2016).

196.   Vidotti, M. & Torresi, S. I. C. De. Nanochromics Old Materials, New Structures and Architectures. *J. Braz. Chem. Soc*. 19(7), 1248–1257 (2008).

197.   Granqvist, C.G. Electrochromic Thin Film Devices. *Workshop on ' Physics for Renewable Energy*. (2005).

198.   Mortimer, R. J., Rosseinsky, D. R. & Monk, P. M. S. Electrochromic Materials and Devices. *Electrochromic Mater. Devices.* 77, 1–638 (2015).

199.   Amb, C. M., Kerszulis, J. A., Thompson, E. J., Dyer, A. L. & Reynolds, J. R. Propylenedioxythiophene (ProDOT)-phenylene copolymers allow a yellow-to-transmissive electrochrome. *Polym. Chem.* 2, 812–814 (2011).

200.   Xu, T., Walter, E.C., Agrawal, A., Bohn, C., Velmurugan, J., Zhu, W., Lezec, H.J. & Talin, A.A. High-contrast and fast electrochromic switching enabled by plasmonics. *Nat.*

Commun. 7, 1-6 (2016).

201.   Jain, V., Khithere, M., Montazami, R., Yochum, H.M., Shea, K.J. & Heflin, J.R. High-contrast solid-state electrochromic devices of viologen-bridged polysilsesquioxane nanoparticles fabricated by layer-by-layer assembly. *ACS Appl. Mater. Interfaces* 1, 83–89 (2009).

202.   Mishra, S. P., Krishnamoorthy, K., Sahoo, R. & Kumar, A. Synthesis and characterization of monosubstituted and disubstituted poly(3,4-propylenedioxythiophene) derivatives with high electrochromic contrast in the visible region. *J. Polym. Sci. Part A Polym. Chem.* 43, 419–428 (2005).

203.   Mohammad, A., Kapoor, K. & Mobin , S. M. Improved Photocatalytic Degradation of Organic Dyes by ZnO-Nanoflowers. *Chem. Select.* 1, 3483–3490 (2016).

204.   Thao, L., Dang, T., Khanitchaidecha, W., Channei, D. & Nakaruk, A. Photocatalytic Degradation of Organic Dye under UV-A Irradiation Using TiO_2-Vetiver Multifunctional Nano Particles. *Materials..* 10, 1-12 (2017).

205.   Pipi, A., Byzynski, G. & Ruotolo, L. Photocatalytic Activity and RNO Dye Degradation of Nitrogen-doped TiO_2 Prepared by Ionothermal Synthesis. 20(3), 628-638 (2017).

206.   Jothi Ramalingam, R. Surface and Electrochemical Characterization of N-Fe-doped-TiO_2 Nanoparticle Prepared by Hydrothermal and Facile Electro-Deposition Method for Visible Light Driven Pollutant Removal. *Int. J. Electrochem. Sci.* 12, 797–811 (2017).

207.   Nica, I. C.Stan, M.S., Popa, M., Chifiriuc, M.C., Lazar, V., Pircalabioru, G.G., Dumitrescu, I., Ignat, M., Feder, M., Tanase, L.C., Mercioniu, I., Diamandescu, L. & Dinischiotu, A. Interaction of new-developed TiO_2-based photocatalytic nanoparticles with pathogenic microorganisms and human dermal and pulmonary fibroblasts. *Int. J. Mol. Sci.* 18(2), 1-23 (2017).

208.   Peng, F., Gao, H., Zhang, G., Zhu, Z., Zhang, J. & Liu, Q. Synergistic Effects of Sm

and C Co-Doped Mixed Phase Crystalline TiO$_2$ for Visible Light Photocatalytic Activity. *Materials.* 10, 1-14 (2017).

209.   Vaiano, V., Sacco, O, Sannino, D. & Clambell, P. N-Doped TiO$_2$: An Efficient Catalyst for the Photocatalytic Treatment of Water and Wastewater under Visible Light Irradiation. *J. Adv. Chem. Eng.* 6(1), 1 (2016).

210.   Pires, N. M. iguel M., Dong, T., Hanke, U. & Hoivik, N. Recent developments in optical detection technologies in lab-on-a-chip devices for biosensing applications. *Sensors.* 14, 15458–15479 (2014).

211.   Park, N-H., Akamatsu, T., Itoh, T., Izu, N. & Shin, W. Calorimetric thermoelectric gas sensor for the detection of hydrogen, methane and mixed gases. *Sensors*. 14, 8350-8362 (2014)..

212.   Solovei, D., Žák, J., Majzlíková, P., Sedláček, J. & Hubálek, J. Chemical sensor platform for non-invasive monitoring of activity and dehydration. *Sensors.* 15, 1479–1495 (2015).

213.   Gupta, V. K. & Africa, S. Optical and Electrochemical Selective Sensor for Zn 2$^+$ ions. *Int. J. Electrochem. Sci*. 11, 1640–1650 (2016).

214.   Chen, X. Colorimetric sensing of non-ionic and cationic surfactants using a versatile anionic poly(3,4-propylenedioxythiophene) derivative. *Anal. Methods.* 7, 2800–2805 (2015).

215.   Ping, Y., Gong, Y., Fu, Q. & Pan, C. Preparation of three-dimensional graphene foam for high performance supercapacitors. *Prog. Nat. Sci. Mater. Int.* 27(2), 177-181 (2017).

216.   He, X., Wang, J., Xu, G., Yu, M. & Wu, M. Synthesis of microporous carbon/graphene composites for high-performance supercapacitors. *Diam. Relat. Mater.* 66, 119–125 (2016).

217.   Wang, K., Zhang, X., Sun, X. & Ma, Y. Conducting polymer hydrogel materials for

high-performance flexible solid-state supercapacitors. *Sci. China Mat.* 59(6), 412–420 (2016).

218.   Li, Y., Zhang, Q., Zhang, J., Jin, L., Zhao, X. & Xu, T. A top-down approach for fabricating free-standing bio-carbon supercapacitor electrodes with a hierarchical structure. *Sci. Rep.* 5, 1-10 (2015).

219.   Sun, F., Gao, J., Zhu, Y., Pi, X., Wang, L., Liu, X. & Qin, Y. A high performance lithium ion capacitor achieved by the integration of a Sn-C anode and a biomass-derived microporous activated carbon cathode. *Sci. Rep.* 7, 1-10 (2017).

220.   Stenger-Smith, J.D., Chafin, A.P., Kline Jr, C.F., Ostrom, G.S. & Quintana, R.L. Ionic Liquids in Charge Storage Devices : Effect of Purification on Performance. (IntechOpen), 2011.

221.   Chen, H., Lee, K. & Hu, C. A dye-sensitized photo-supercapacitor based on PProDOT-Et$_2$ thick films. *J. Power Sources.* 195, 6232–6238 (2015).

222.   Amasawa, E., Sasagawa, N., Kimura, M. & Taya, M. Design of a New Energy-Harvesting Electrochromic Window Based on an Organic Polymeric Dye, a Cobalt Couple, and PProDOT-Me$_2$. *Adv. Energy Mater.* 4(14), 1-9 (2014).

223.   Ling, M., Qiu, J., Li, S., Yan, C., Kiefel, M.J., Liu, G. & Zhang, S. Multifunctional SA-PProDOT Binder for Lithium Ion Batteries. *Nano Lett.* 15, 4440–4447 (2015).

PART 3: RESULTS AND DISUSSION

Overview

This section is based on results obtained for all prepared materials, their characterization and applications.

Chapter 3, titled 'Detection of Bisphenol A Using a Biosensor Based on a Polymethyl Methacrylate-Grafted Polyaniline Nanocomposite' is based on a polyaniline nanocomposite with grafted PMMA and titanium dioxide nanoparticles (TiO₂). This nanocomposite served as a receiving matrix and electron transfer mediator for a biosensor fabricated for detection of an endocrine disrupting chemical, bisphenol A (BPA).

Chapter 4, titled 'Gold nanoparticles amplified poly(3,4-propylenedioxythiophene) (PProDOT) properties' explores the effect of incorporating gold nanoparticles into PProDOT as a means of enhancing its electroconductivity for later application as a redox probe and charge transfer mediator in biosensors.

Chapter 5, 'Electrochemical Poly(3,4-propylenedioxythiophene) DNA Aptamer Biosensor for Signalling Interferon Gamma (IFN-ɣ) TB Biomarker, focusses on fabrication, characterization and application of an aptasensor system fabricated onto the nanocomposite (intensively characterized in Chapter 4) for electrochemical signalling of the tuberculosis biomarker interferon gamma.

Chapter 3

Detection of Bisphenol A Using a Biosensor Based on a Polymethyl Methacrylate-Grafted Polyaniline Nanocomposite

ABSTRACT

Bisphenol A (BPA), a potential endocrine disrupting chemical found in many household appliances, has been proven to cause adverse problems in both human health and wildlife. As a result, a tolerable daily intake value has been set by regulatory bodies, with the current minimum value of 4 µg/kg bodyweight revised due to proven serious effects at concentrations much lower than the former 50 µg/kg recommended by the United States Environmental Protection Agency. This study developed an electrochemical enzyme-based biosensor system employing manganese peroxidase and a highly electroconductive nanocomposite of polyaniline, poly(methyl methacrylate) and titanium dioxide nanoparticles for quantification of BPA. The voltammetric results showed that the nanocomposite had enhanced electroactivity in neutral phosphate buffer medium which is favourable for faster electron transfer between the electrode and the interface at which enzyme/analyte interactions occur. The nanobiosensor system showed high sensitivity towards different concentrations of bisphenol A, with a detection limit of 0.17 nM, a sensitivity of 2.11 µA nM^{-1} within a dynamic linear range extending from 0.2 nM to 1.2 nM.

KEYWORDS: bisphenol A, conducting polymer nanocomposite, manganese peroxidase, electrochemical biosensor, electrochemical polymerization, square wave voltammetry.

1. Introduction

Endocrine disrupting compounds have been under intensive investigation by academic and industrial researchers globally, due to their detrimental toxicity which leads to negative effects on human health, wildlife and the environment [83,87,224]. Bisphenol A (BPA), amongst other phenolic chemicals, is categorized under these compounds due to its estrogenic behaviour, through which it mimics the human oestrogen system by binding to the α- and β- estrogen receptors [79–81]. BPA is a monomer used in the manufacture of polycarbonates and epoxy resins which are used in consumer products such as children's toys, plastic food containers, metal canned food and beverage liners, water pipes, dental sealants, electronics and flame retardants [75,76,225]. The excellent light-weight, transparency, durability and thermostability properties of BPA yield thermosets of excellent thermal and mechanical properties which best suit the increasing demand for the plastic-based re-usable products, making BPA one of the highest volume chemicals produced per year [226].

Despite the diverse applications in which BPA is found, this chemical has been proven to degrade from the epoxy resins or leach out of the polycarbonates and migrate into the contents of different packaging material. BPA is also a potential pollutant which enters the environment as waste from manufacturing companies, research institutions and by degradation as a leachate from landfills [78]. Many studies have reported that human exposure to BPA is associated with abnormalities and behavioural disorders in children [227,228], cancer [84,85], diabetes and hypertension [86,229], miscarriages [230] and altered male reproduction [231]. As a result, BPA is amongst the chemicals under regulation, assessment and monitoring by bodies such as the World Health Organisation (WHO), the United States Environmental Protection Agency (EPA) and the European Food Safety Authority (EFSA). 'Following the banning of the use of BPA especially in baby-products, there has been a tremendous shift towards the dominance of

BPA-free products in the markets. This notwithstanding BPA is still used in other products and has been shown to cause adverse effects at concentrations much lower than the set TDI value of 50 µg/kg per day as recommended by the EPA and EFSA [226,232,233]. As a result of such reports, EFSA has revised the TDI to a new temporary value of 4 µg kg^{-1} bodyweight per day [233]. Therefore, there is a mandatory need for faster and reliable highly sensitive methods for trace level detection of this compound in order to protect human health, wildlife and the environment.

Electrochemical techniques, especially biosensors with incorporated nanoparticles, have gained much interest as detection methods for BPA and other toxic chemicals. BPA has been detected and monitored using biosensors and other methods in a variety of samples such as human fluids (urine, serum and blood) [234–236], water samples (bottled water and wastewater) [237–239], canned food (fish, corn and tomato paste) [28-242] and consumer packaging materials (beverage cans and plastic containers) [243–245]. Conductive polymers have received considerable attention due to their conductivity which allows charge transport and their biocompatibility which makes them suitable candidates for biomolecule immobilization during biosensor fabrication. Amongst these is polyaniline (PANI), a π-conjugated conductive polymer which has vastly gained applications in biosensors, lithium-ion batteries and fuel cells [246–248]. However, PANI has been associated with drawbacks such as poor mechanical properties and selective conductivity wherein it shows poor electroactivity in neutral pH media [249,250]. As a result, PANI composites have emerged as the best transducer material for electrochemical sensor applications. Various composites of PANI doped with nanoparticles (e.g. nano-graphene, carbon nanotubes, quantum dots and titanium dioxide nanoparticles) and other polymeric materials (e.g. polymethyl methacrylate and polyurethane) have been synthesized and applied [249,251–253]. Titanium dioxide (TiO_2) nanoparticles are electrochemically active transition metal oxides which possess properties such as high surface

area and high photocatalytic activity. These properties have gained TiO_2 applications in sensors, solar cells, water purification systems and most importantly, photocatalytic removal of various environmental pollutants [254–257]. Poly(methyl methacrylate) (PMMA) is a hydrogellic polymer which is applied mainly in biomedicine due to its biocompatibility towards human tissue and has gained applications in biosensors, following its consideration as a good matrix for enzyme immobilization and stabilization [258,259].

In this study, a polyaniline-based nanocomposite employing the combined properties of the biocompatible poly(methyl methacrylate) and the transition metal titanium dioxide nanoparticles (TiO_2) is reported. The combined effects of these materials (i.e. high electroconductivity, biocompatibility and high surface area) were utilized to yield a nanocomposite with (a) a high surface area for high enzyme loading, (b) improved biocompatibility for non-destructive enzyme immobilization and to maintain the activity of the enzyme and (c) enhanced electroconductivity for increased sensitivity and faster electron transfer between the enzyme and the electrode. The nanocomposite employed here was extensively characterized and the synergistic effects of both PMMA and TiO_2 as dopants to PANI were investigated structurally, morphologically, optically and electrochemically [260]. Herein, we report for the first time, a manganese peroxidase (MnP) biosensor for detection of the endocrine disruptor, bisphenol A. MnP is a fungal enzyme well-known for degradation and catalytic oxidation of various phenolic compounds in a wide pH range. The enzyme was immobilized onto the polyaniline nanocomposite through drop casting. The response properties of the biosensor towards BPA were studied by cyclic voltammetry (CV) and square wave voltammetry (SWV).

2. Experimental section

2.1. Reagents

All reagents were of analytical reagent grade and purchased from Sigma Aldrich. Aniline was purified by vacuum distillation and used in the electrochemical synthesis of polyaniline (PANI) in acidic medium sulphuric acid (H_2SO_4). The following chemicals were used without further purification: Bisphenol A (BPA), Ti(IV) oxide rutile nanopowder (TiO_2), poly(methyl methacrylate) (PMMA), N-Hydroxysuccinimide (NHS), N-Ethyl-N′-(3-dimethylaminopropyl) carbodiimide hydrochloride (EDC), sodium phosphate monobasic dihydrate ($NaH_2PO_4 \cdot 2H_2O$), disodium hydrogen phosphate dibasic dihydrate ($Na_2HPO_4 \cdot 2H_2O$), tetrahydrofuran (THF), bovine serum albumin (BSA) and absolute ethanol. $NaH_2PO_4 \cdot 2H_2O$ and $Na_2HPO_4 \cdot 2H_2O$ were used in the preparation of 0.1 M phosphate buffer (PBS), pH 7.4. A 4.2 µM MnP stock enzyme solution was prepared from manganese peroxidase (from *Nematoloma frowardii*; EC 1.11.1.13). De-ionized water, used throughout the experiments, was prepared with a Milli-Q water purification system. Analytical grade argon, obtained from Afrox South Africa, was used for degassing of the cell solutions where necessary. Micro-alumina powders (1.0 µm, 0.3 µm and 0.05 µm) and microcloth pads (Buehler, IL, US) were used for pre-conditioning of the glassy carbon working electrode (GCE) prior the experiments.

2.2. Characterization of the nanocomposite

2.2.1. Electrochemical characterization and electrochemical biosensing techniques

Electrochemical measurements (cyclic voltammetry (CV) and square wave voltammetry (SWV)) were recorded using a Princeton Applied Research Potentiostat Model 273A integrated to a conventional three-electrode system with a glassy carbon working electrode (GCE), Ag/AgCl (3 M NaCl) reference electrode and a platinum wire counter electrode. Prior to use, the working electrode was pre-conditioned by polishing in micro-alumina slurries of 1.0 µm,

0.3 µm and 0.05µm, followed by ultrasonication for 5 minutes in ethanol and water, respectively. All experiments were conducted in a 10-ml phosphate buffer solution (pH 7.4).

The electrochemical transitions of the nanocomposite were explored by CV cycling between -300 mV and +1300 mV (vs Ag/AgCl) at varying rates from 1 mV·s^{-1} and 8 mVs^{-1}.Using electrochemistry, electrode interface significant parameters such as the diffusion coefficient, surface concentration and the number of electrons transferred during reduction-oxidation processes can be determined as these parameters play a crucial role towards performance of different devices employing them [261].

2.2.2. *Bond properties and structural confirmation*

Baseline-corrected Raman spectra of PANI and the PANI/PMMA/TiO$_2$ nanocomposite were recorded in the frequency range 500 cm^{-1} to 2000 cm^{-1} using a Dilor XY Raman spectrometer in which samples were illuminated by a Coherent Innova 300 Argon laser ($\lambda = 514.5$ nm). This technique was employed to confirm successful doping of PANI by identifying the characteristic transmission bands and Raman shifts associated with the obtained polymer state, bond deformations and vibrations [262,263].

2.2.3. *Morphological view of doped and undoped PANI*

The morphology of the samples was investigated using a Hitachi S3000N scanning electron microscope at an acceleration voltage of 20 kV. SEM studies have the potential to clearly show how the dopants are attached to the PANI backbone. The polymer dopants have been shown to affect the polymer morphology in a series of ways where they can form the core-shell architectures, adsorb and attach on the surface of the polymer or distribute evenly within the polymeric network [264–266].

2.2.4. Energy absorption and chromophore identification in the nanocomposite

The ultraviolet-visible (UV-Vis) spectra of samples dissolved in dimethyl sulfoxide (DMSO) were recorded on a Nicolet Evolution 100 spectrophotometer (Thermo Electron Cooperation, UK) between 280 nm and 900 nm. PANI is characterized by tuneable optical activity where it absorbs energy at different wavelengths of the spectrum and has gained application in optical devices following the tuning of its optical properties through incorporation of different chromophores to its backbone. Therefore, this techniques allows identification of incorporated or foreign chromophores to PANI based on alterations in its conjugation lengths and doping level [267,268].

2.3. Stepwise BPA biosensor fabrication strategy

2.3.1. Potentiodynamic deposition of PANI-PMMA-TiO$_2$ nanocomposite film

A monomer solution containing distilled aniline refluxed with 0.02% wt TiO$_2$ and 100 µl of a PMMA solution (0.2 % wt in THF) was prepared in 10 ml of 1 M H$_2$SO$_4$. The solution was degassed under argon gas for 10 minutes. The GC/PANI/PMMA/TiO$_2$ nanocomposite film was potentiodynamically deposited onto a glassy carbon electrode by subjecting the monomer solution to a 30-segments potential cycling at 30 mV/s between -200 mV and +1200 mV (vs Ag/AgCl). A green film (denoted GC//PANI-PMMA-TiO$_2$), characteristic of PANI in its conducting emeraldine salt form, was obtained. A short schematic presentation for deposition of the nanocomposite is shown in Figure 10 with the proposed interactions between PANI, PMMA and TiO$_2$.
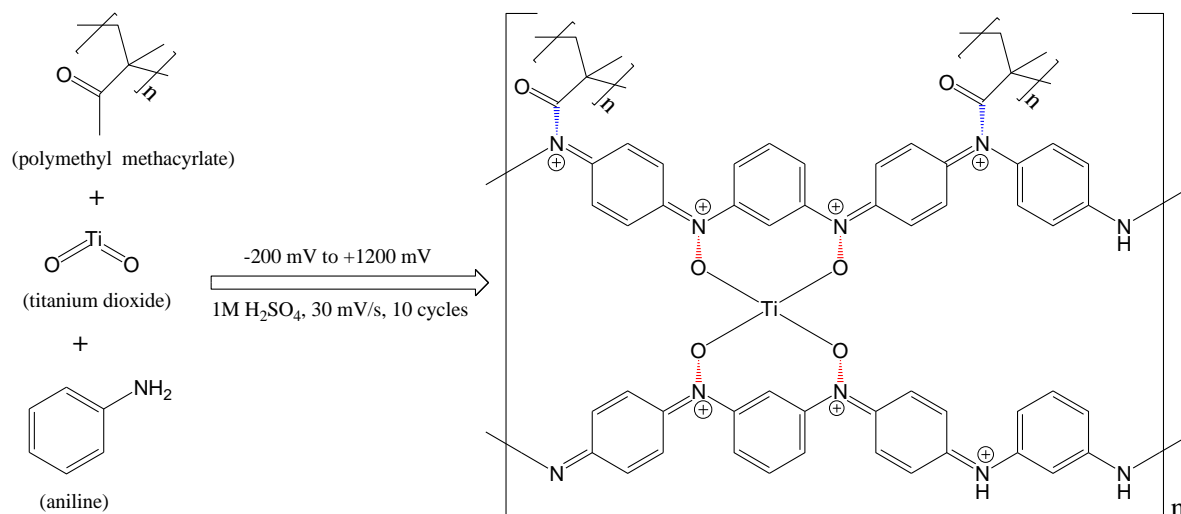
Figure 10: Schematic presentation for the preparation the nanocomposite and proposed interactions between its components.
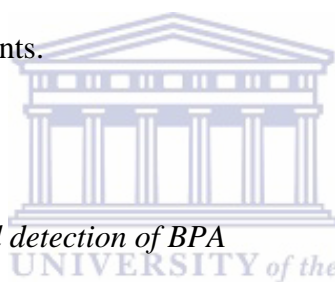
2.3.2. *Biosensor fabrication and detection of BPA*

The PANI-PMMA-TiO$_2$ nanocomposite (above) was used as a receiving matrix for the enzyme MnP. A 1:1 solution (3 µl) of 0.1 M EDC:NHS was drop-coated onto the nanocomposite, followed by drop-casting of 3 µl of MnP:BSA solution where BSA acted as a blocking agent to unreactive sites of the enzyme. The stable, amide bond-linked biosensor system, denoted as GC//PANI-PMMA-TiO$_2$-MnP, was immersed in 3 ml 0.1 M PBS (pH 7.4) to remove any unbound enzyme and was kept at 4 ˚C for 4 h before use. The preparation scheme is shown in Figure 11.
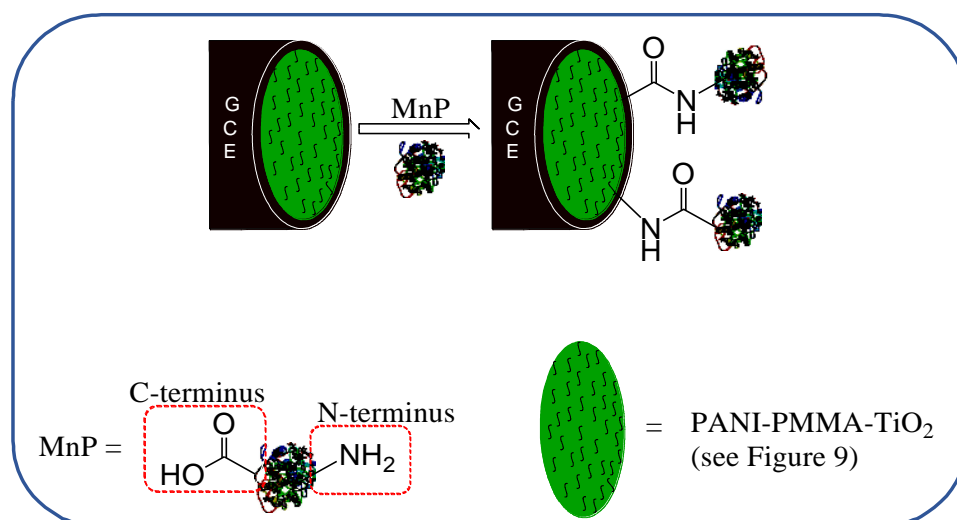
Figure 11: Schematic representation for fabrication of the MnP nanobiosensor system achieved through covalent bonding between the amine and carboxyl groups from both the nanocomposite and the enzyme.
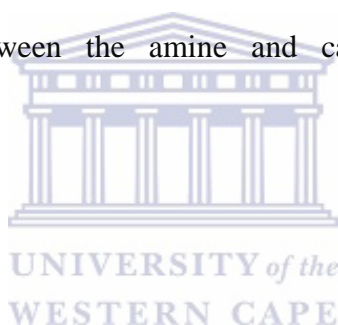
3. Results and discussion

3.1. Chemical structure confirmation using Raman spectroscopy

The molecular structure of PANI and its signature bonds were identified in its pristine and doped form using Raman spectroscopy (Figure 12).The PANI film (Figure 12(a)) exhibits the characteristic signature of peaks associated with its benzenoid and quionoid rings. The peak at 578 cm⁻¹, 848 cm⁻¹ and 1197 cm⁻¹ are assigned to the in plane N-H bending deformations of the amine groups and C-H in plane bending vibrations of the benzenoid and quinoid rings associated with PANI's emeraldine salt form [269]. The peaks at 1259 cm⁻¹ and 1460 cm⁻¹ are assigned to C-N stretching mode of secondary amine typically representing a benzenoid structure and C=N stretching mode of a quinoid ring, respectively, while the peak at 1346 cm⁻¹ is associated with C-N bond characteristic to a localized polaronic structure. The peaks at 1590 cm⁻¹ and 1630 cm⁻¹ respectively represent C-C and C=C stretching vibrations of both the

benzeniod and quinoid units of PANI while the peak at 1520 cm^{-1} depicts N-H bending deformations of a protonated amine [262,269,270]. Therefore, it can be concluded that the electrodeposited PANI film was obtained in the emeraldine salt form of PANI and the Raman bands confirm presence of a polaronic structure and protonated amine groups associated with the sulfuric acid used during polymerization, acting as a dopant to PANI [271].
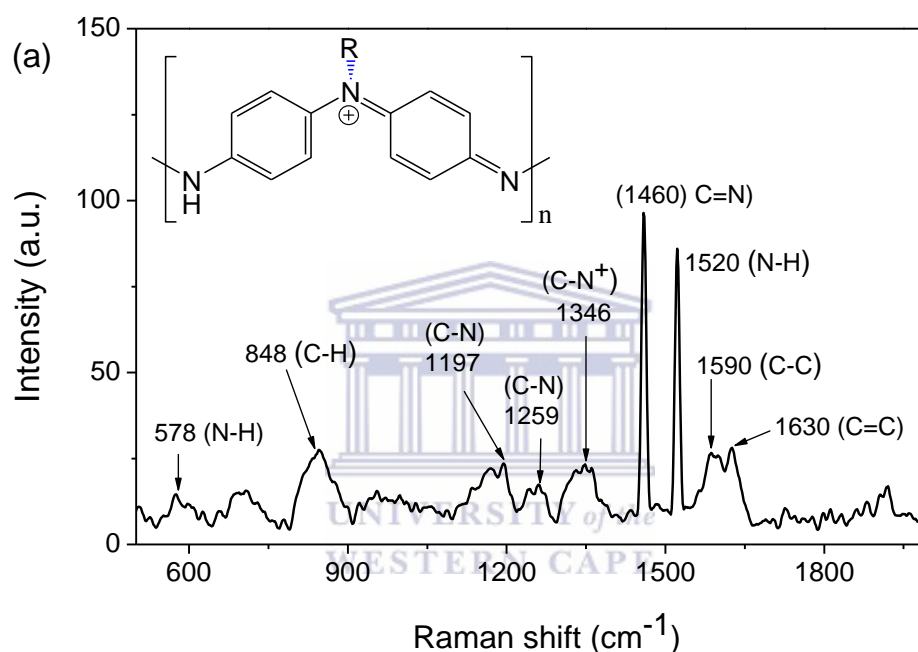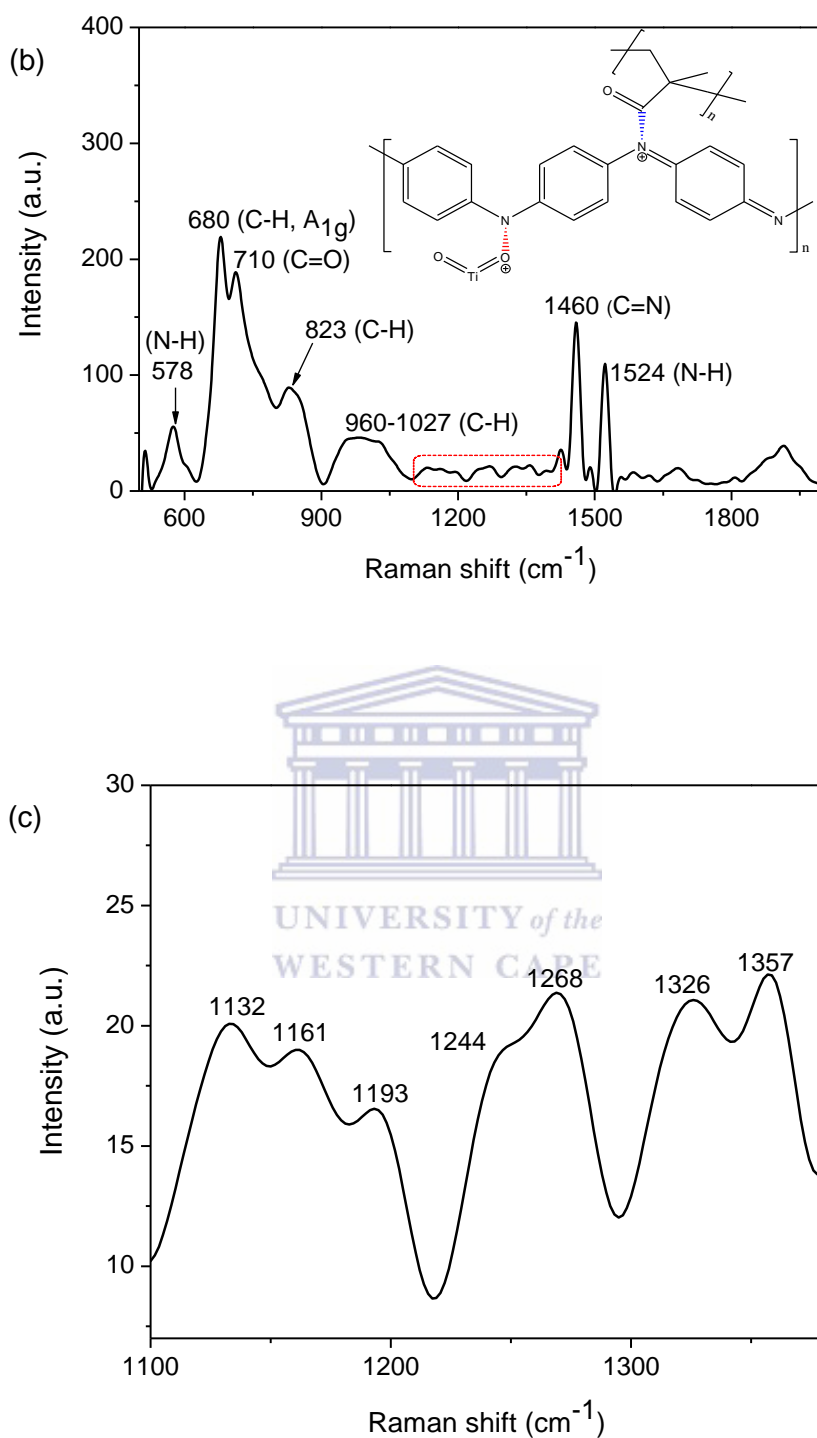
Figure 12: Chemical structure confirmation using Raman spectroscopy. (a) PANI, (b) PANI-

PMMA-TiO$_2$ and (c) a magnified view of the red-squared area. (in (b))

http://etd.uwc.ac.za

The nanocomposite also reveals that characteristic signature peaks of PANI. The peaks at 578 cm^{-1} and 1460 cm^{-1}, assigned to the in plane N-H deformations of amine groups and C=N stretching vibrations of a quinoid unit were also observed at the same wavenumbers in PANI. The peak at 1524 cm^{-1}, assigned to N-H bending deformations of a protonated amine was also evident in the PANI film at 1520 cm^{-1} while the C-H in plane vibration peak at 823 cm^{-1} was observed at 848 cm^{-1} in PANI. The highly pronounced peak at 680 cm^{-1} may be attributed to either A^1_g vibrations of the TiO_2 dopant or C-H bending vibrations of the PANI rings at higher intensity induced by overlapping C-H vibrations of the PMMA while the peak at 710 cm^{-1} is solely attributed to C=O vibrations of PMMA [272].

Absence of an obvious peak for the $C-N^+$ vibrations associated with presence of polaronic structures became suspicious and led to zooming in to the area marked by the red square in the spectrum (Figure 12(b)). As a results, well resolved coupled peaks were revealed (Figure 12(c)). The first three peaks at 1132 cm^{-1}, 1161 cm^{-1} and 1193 cm^{-1} are responsible for the C-H bond deformations while the pairs at 2144 cm^{-1} - 1268 cm^{-1} and 1326 - 1357 cm^{-1} are respectively assigned to C-N and $C-N^+$ vibrations of the benzenoid and polaronic structures of PANI. These peaks are assigned relatively to PANI as above. These pairs are attributed to overlapping symmetric and asymmetric vibrations while the observable shifts to higher and lower wavenumbers and increased intensity confirm interactions between PANI and its dopants, thus inferring their incorporation into the PANI backbone [273,274].

3.2. Energy absorption properties

Ultraviolet-visible (UV-vis) spectroscopy was used to confirm the state of PANI obtained in both undoped and doped films through identifications of electronic energy transitions by different chromophores. Figure 13 displays the UV-Vis spectrum of PANI and the PANI-PMMA-TiO_2 nanocomposite. PANI shows two characteristic absorption peaks at 335 nm and

457 nm corresponding to π-π* transitions of the C=C bonds in the benzenoid ring and n-π* polaronic transitions of the C=N bonds in the quinoid ring, respectively, while the large broad peak commencing around 800 nm, also known as the free-carrier tail, corresponds to n-π* polaronic transitions associated with delocalized proton charge carriers indicative of the protonated emeraldine salt form of PANI [275,276].
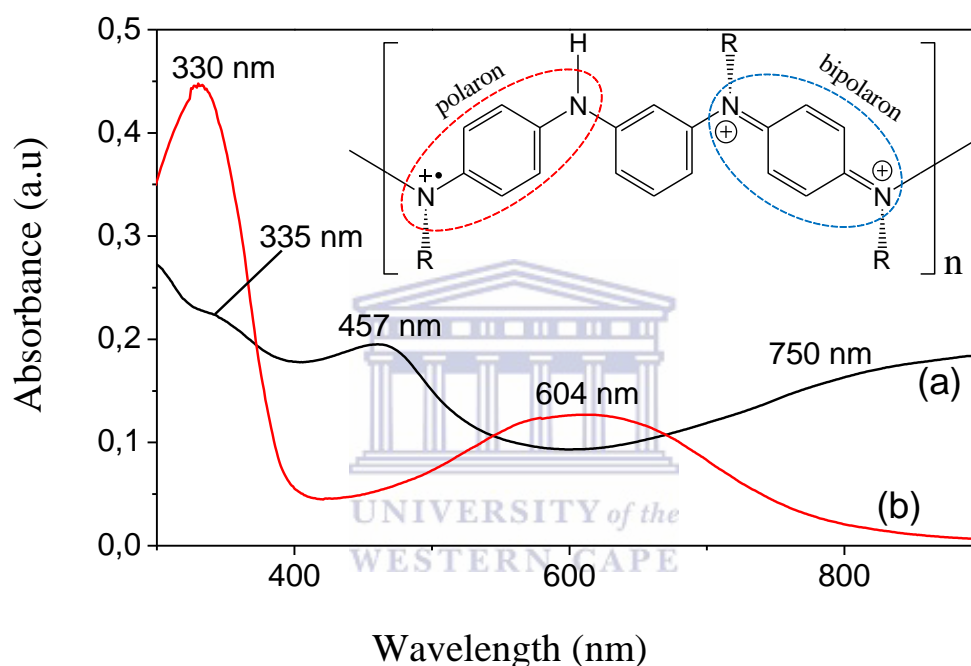
Figure 13: Energy absorption properties of (a) PANI and (b) PANI-PMMA-TiO$_2$ induced by different chromophores in the polymer matrix.

The nanocomposite also exhibits the characteristic π-π* transitions at 330 nm. This peak is observed at a lower wavelength than in the PANI film and this shift is associated with conjugation of the dopants to PANI which decreases the energy level of the π-orbital, change the benzenoid to quinoid ratio and eventually shorten its conjugation length [276,277]. The incorporation of the two dopants to PANI is also confirmed by disappearance of the free-carrier

tail and the peak corresponding to n-π* polaronic transitions observed at 457 nm in the PANI film. Instead, a new peak centred at 604 nm is revealed and is attributed to the n-π* polaronic transitions n from the highest occupied energy level of the benzenoid unit to the lowest unoccupied energy level of the quinoid units [278]. Therefore, it may be concluded that the dopants form strong bonds with the PANI through its amine groups, thereby displacing the protons responsible for the free-carrier tail revealing the deprotonated emeraldine base form of PANI with only polarons and bipolarons as charge carriers [279].

3.3. Electron exchange and charge transfer properties

PANI has three interconnected oxidation states which differ according to chemical structure namely; pernigraniline, emeraldine and leucoemeraldine [280,281]. Amongst these, emeraldine is the most conductive form whose electrochemical properties can be switched between a base and a salt through oxidation and reduction but this phenomenon is pH dependent as pure PANI shows high electroactivity only in acidic media (pH ≤ 4). Hence, this property is addressed by incorporation of dopants. With respect to PANI, its composites show improved electroactivity in neutral pH media but with less ability than in acidic media [260,282]. Two redox pairs or even one pair are usually obtained for PANI composites in neutral media due to overlapping of the redox processes observed in acidic media [283].
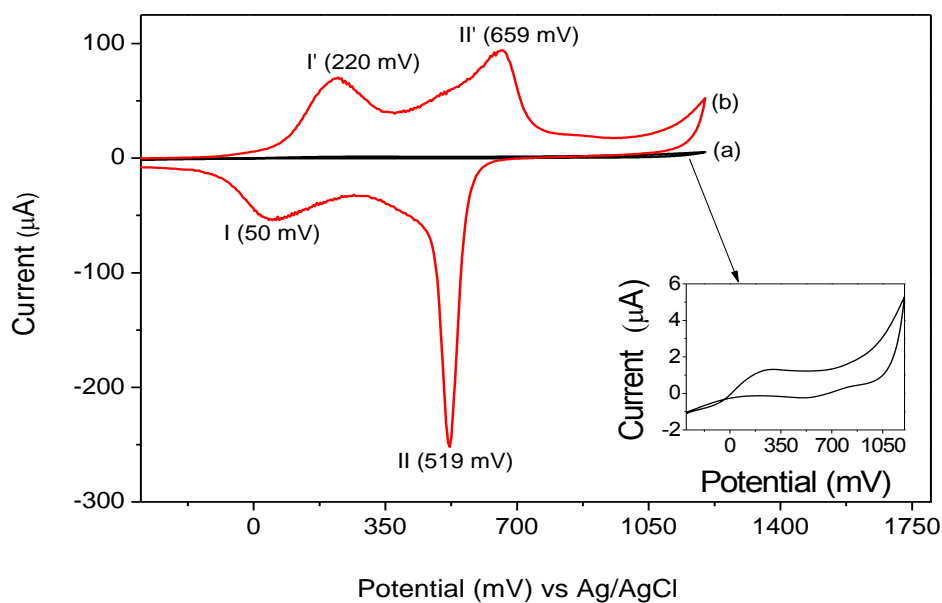
Figure 14: CV graph obtained for the PANI-PMMA-TiO$_2$ nanocomposite in 0.1 M PBS at 2 mV/s. The nanocomposite exhibits two well-resolved redox pairs attributed to electronic transitions between PANI's emeraldine, leucoemeraldine and pernigraniline states.
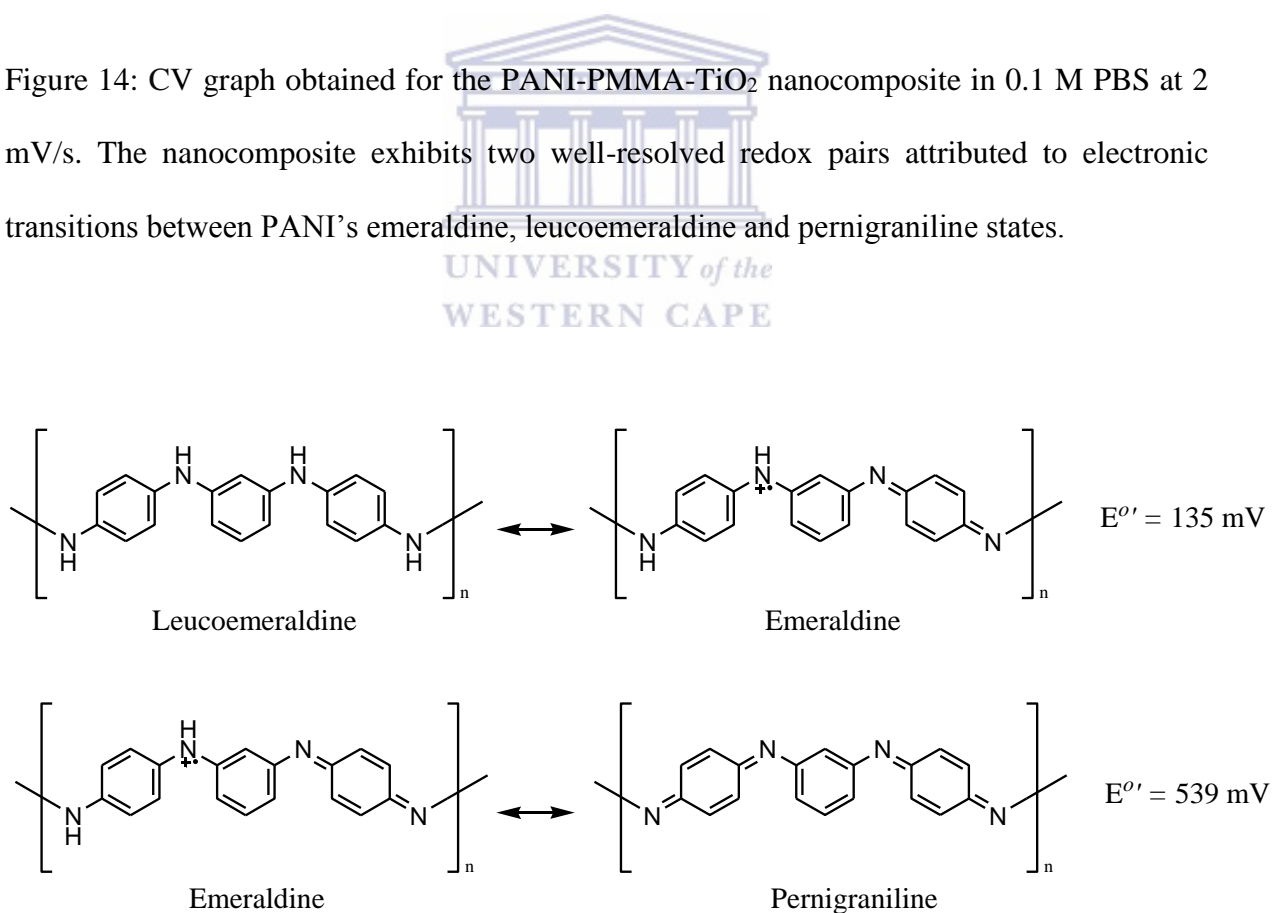
Figure 15: Representative chemical structures depicting the electron exchange between the PANI oxidation states in the nanocomposite.

Figure 14 shows the CV curves of PANI and the PANI-PMMA-TiO$_2$ nanocomposite in phosphate buffer solution (PBS, pH 7.4) at 2 mV/s. PANI exhibits no reduction or oxidation peaks due to loss of its electroactivity in the neutral pH PBS medium. Its nanocomposite exhibits two redox pairs, labelled I/I´ (50 mV/ 220 mV vs Ag/AgCl) and II/II´ (519 mV/ 659 mV), assigned to PANI's interconnected transitions between leucoemeraldine/emeraldine and emeraldine/pernigraniline, respectively [284,285]. The chemical structures of these PANI transition processes are also shown in the Figure 15. The increase in the current peaks observed for the nanocomposite is associated with the synergistic effect of the incorporated dopants which reduce the migration length for electrolyte ions leading to a reduced resistance of charge flow, hence increasing the charge transfer capability of the nanocomposite [286].

The PANI-PMMA-TiO$_2$ nanocomposite was then evaluated at varying scan rates to determine different parameters including its reversibility, surface concentration and the rate of electron diffusion. The CV curves of the nanocomposite at scan rates between 1 and 8 mV/s are shown in Figure 16 with the insert representing the linear relationship correlating current dependence of the anodic peak I´ on scan rate (with a linear correlation value r = 0.999). It is observed that current peaks for all processes increase with increasing scan rates indicating a reversible electron transfer determined process at lower scan rates (between 1 mV/s and 3 mV/s) and a quasi-reversible process a higher scan rates (from 4 − 8 mV/s) while the shift in potential peaks indicates electron hopping along a well surface adhered polymeric network [238,287]. The nanocomposite exhibited a diffusion coefficient of 4.7 x 10^{-6} cm/s^2 which in range with reported values for doped PANI films [288,289]. The nanocomposite also reveals that peak II´ showed a potential shift towards negative values between 1 mV/s and 3 mV/s while peak I broadens and almost disappears with increasing scan rate. Such phenomena is associated with

difficulty in oxidizing emeraldine to pernigraniline at the lowest scan rates and the characteristic loss of reversibility induced by faster scan rates [290].
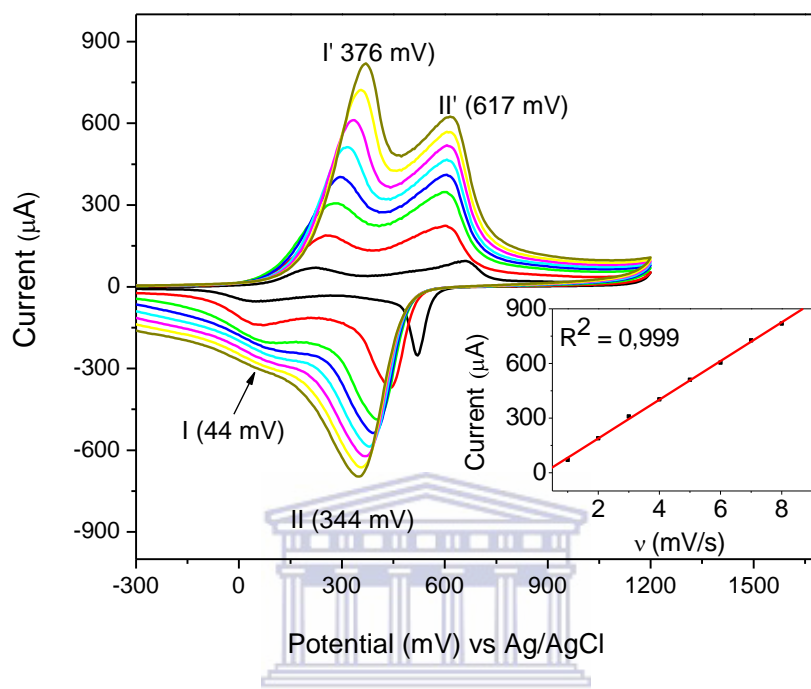
Figure 16: CV graph for the behaviour of the nanocomposite at scan rates varied between 1 mV/s and 8 mV/s. Insert graph depicts current response dependence on scan rate.

3.4. Design of the biosensor interface

The schematic presentation for the design and construction of the biosensor is depicted in Figure 11. The first step was electrodeposition of the polymeric network of PANI with PMMA and TiO_2 nanoparticles in which the dopants PMMA and TiO_2 bound to the PANI through hydrogen bonding between the amine groups of PANI, the oxygen group of TiO_2 and the carboxyl group of PMMA. At fixed concentrations, both PMMA and TiO_2 were grafted into PANI, with the strategic reason of achieving covalent bonding with the carboxyl groups of manganese peroxidase and free amine groups of PANI. Also due to the binding competition between the two dopants, the tacticity of PMMA and the tetragonal conformation of TiO_2 may

leave some of their functional groups exposed. Hence, MnP may also bind to these exposed functional groups through the amine terminus of its amino acids.

The enzyme immobilization and binding step was confirmed using CV at 50 mV/s in the PBS pH 7.4 medium. The parameters were used in accordance with published literature of some biosensor systems for electrochemical BPA quantification in phosphate buffer media [291–293]. The CV confirmation of the stepwise fabrication of the nanobiosensor system is shown in Figure 17. The CV graph excludes the cyclic voltammogram of the PANI nanocomposite (Figure 16) due to the high peak current which mask the CV graphs of other films. When compared to the nanocomposite alone, immobilization of the enzyme (MnP) drastically
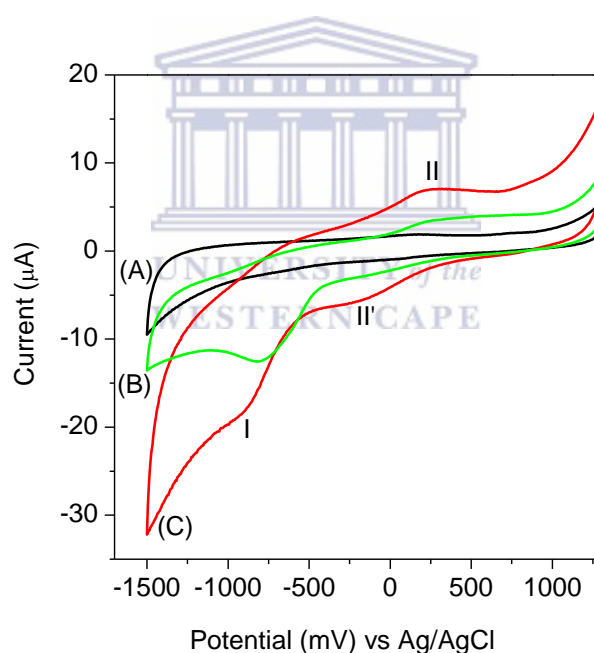
Figure 17: CV graph illustrating current and potential changes during the stepwise fabrication of the biosensor system. (A) PANI, (B) MnP and (C) PANI-PMMA-TiO$_2$-MnP. Enzyme transitions are represented by the peaks II/II′ (for Fe$^{3+/2+}$ redox transitions) and I (for reduction of Mn^{2+} to Mn). the enzyme heme.

decreased the current peaks and this can be attributed to the adsorption of MnP, confirming its binding to the nanocomposite [294,295]. The decrease in current can also be associated with elongation of the polymer chain given the very high molecular weight of the enzyme, leading to an increase in the inter-chain distance and possibly a lag in the electron hopping process within the PANI-PMMA-TiO$_2$-MnP/electrode interface [295,296]. The MnP enzyme exhibits a redox pair (II/II´) centred at +85 mV/250 mV (vs Ag/AgCl) and a reduction peak (I) centred at -740 mV (vs Ag/AgCl) respectively attributed to the redox transitions of Fe$^{3+/2+}$ and reduction of Mn^{2+} to Mn contained in the heme [297].

3.5. Feasibility of the MnP biosensor towards detection of BPA

The feasibility of the nanobiosensor system was evaluated in absence and presence of BPA at a concentration of 0.04 nM using CV and SWV (Figure 18). In the presence of 0.04 nM BPA,
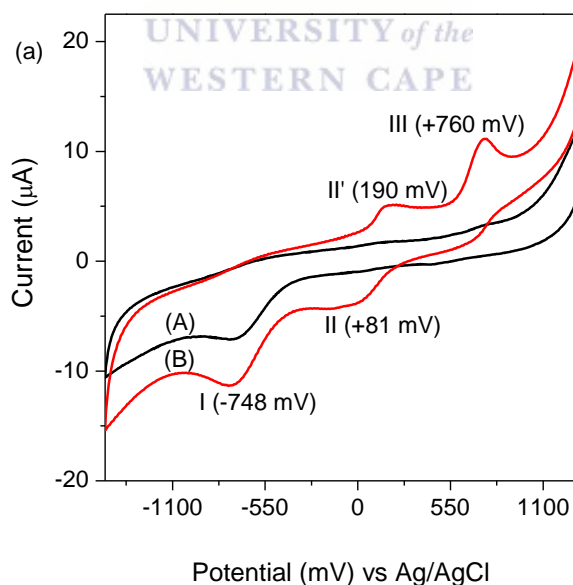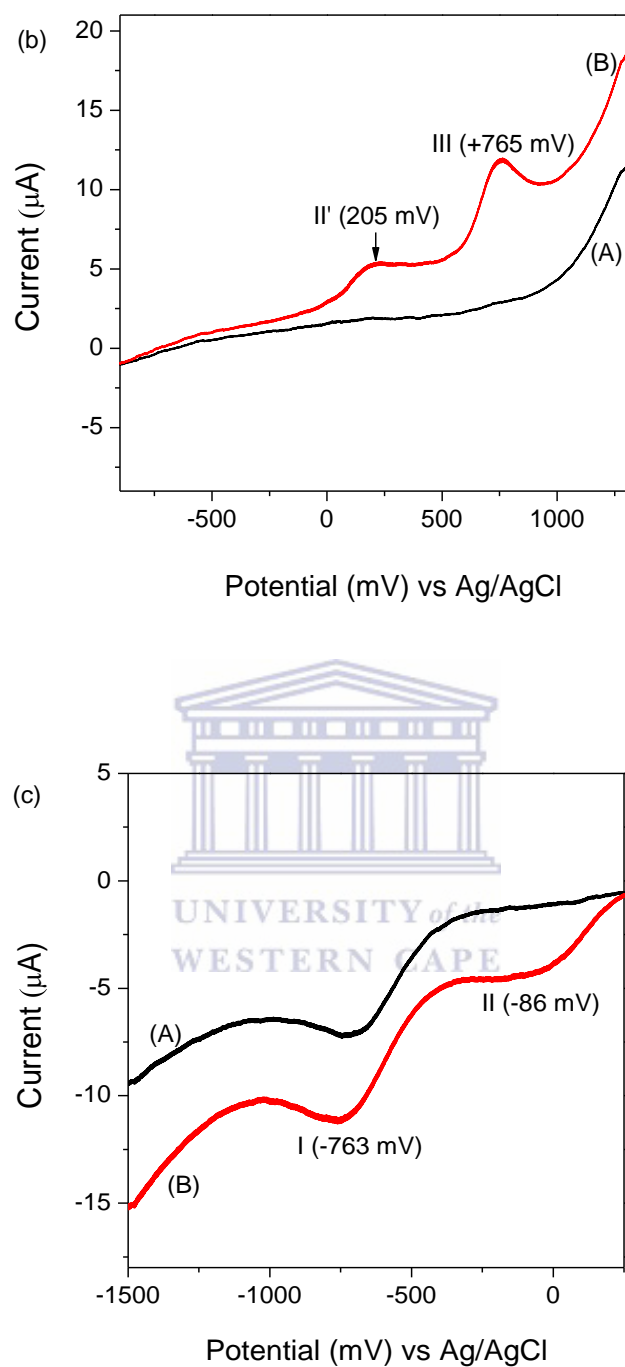
Figure 18: (a) CV, (b) oxidative SWV and (c) reductive SWV profiles demonstrating the performance of the biosensor in (A) absence of BPA and (B) in presence of 0.04 nM BPA.

http://etd.uwc.ac.za

there is an observable increase in current peaks potential shifts of the Mn reduction peak from -740 mV to -765 mV (vs Ag/AgCl), a shift from +250 mV to +190 mV (vs Ag/AgCl) for oxidation of Fe^{2+} to Fe^{3+} and a slight shift from +85 mV to +81 mV (vs Ag/AgCl) for reduction of Fe^{3+} to Fe^{2+}. Potential peak shifts after enzyme immobilization and increased current peaks in presence of BPA have been observed in reported literature [293,297]. These changes are accompanied by formation of a new peak observed at +760 mV (vs Ag/AgCl) that can be assigned to the irreversible oxidation of BPA [298]. All these observations are also evident in the reductive and oxidative SW graphs illustrating a two-fold magnitude of current peaks when compared to the nanobiosensor system in absence of the analyte.
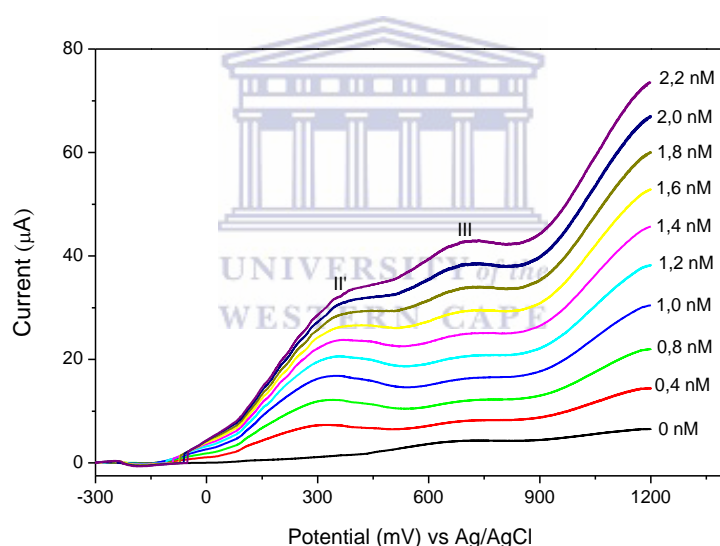
Figure 19: SWV profile portraying the nanobiosensor performance during BPA quantification in 0.1 M PBS (pH 7.4) at 50 mV/s. Detection was conducted through successive additions of 0.4 nM BPA from a minimum concentration of 0.4 nM to a maximum concentration of 2.2 nM.

The nanobiosensor system was then evaluated against increasing concentrations of BPA ranging from 0 nM to 2.2 nM (Figure 19) where it was observed that current peaks for the labelled processes II´ and III, increased with successive additions of higher BPA

concentrations. According to literature BPA has a polymerization tendency [245] and to avoid interference of its polymeric film with the detection signal, peak II´ was considered for the investigation of biosensor parameters and performance. It is worthy to note that at higher concentrations of BPA, the difference in peak currents with successive additions of BPA deteriorates and such behaviour can be correlated to both the hindered charge transfer induced by the insulating poly-BPA film (inferred by the smoothly increasing current peaks with increasing concentrations observed through the peak associated with its oxidation) and saturation of the enzyme associated with decreased availability of binding sites with increased binding of BPA. During performance of enzyme-based biosensors, the apparent Michaelis-Menten constant (K_M^{app}) and the maximum current density *(I_{max})* are crucial kinetic parameters respectively associated with affinity and catalytic activity (saturation) of the enzyme in the presence of its substrate. According to literature, a lower value for the Michaelis-Menten constant identifies stronger affinity between the enzyme and its substrate yielding a stable enzyme-substrate complex that gives the biosensor ability to detect very low concentrations of the substrate with high sensitivity at a constant rate. The *I_{max}* identifies saturation of the enzyme system where a smaller value implies that the system requires less amounts of substrate to saturate and this is linked to a broader analytical linear range
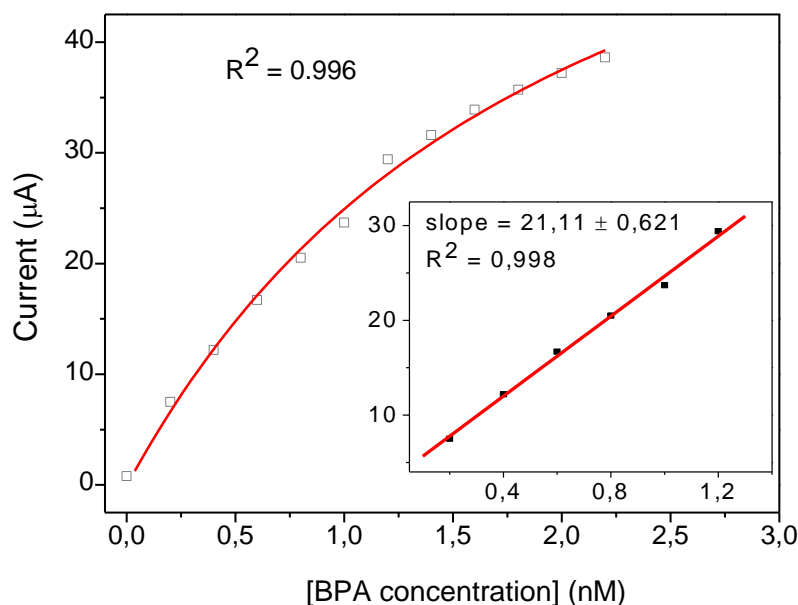
Figure 20: The calibration plot for the biosensor system showing the dependence of current on BPA concentration. Insert graph is the plot of the dynamic linear range.
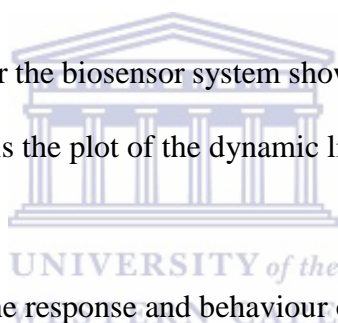
The calibration plot illustrating the response and behaviour of the biosensor during signalling of BPA is shown in Figure 20. By fitting these results into the Michaelis-Menten model, a K_M^{app} value of 0.7 nM and the I_{max} value of 0.03 µA were estimated. The dynamic linear range of the biosensor system was estimated between 0.2 nM and 1.2 nM as illustrated by the linear relationship between BPA concentrations and the current response (Figure 19 insert). From the slope which satisfied Equation 1, a sensitivity of 21.1± 0.621 µA/nM and a detection limit of 0.17 nM were achieved. The detection limit shown by this biosensor is in close proximity with or lower than some sensor systems developed against BPA. For comparison, Table 1 summarizes and compares the performance parameters of this biosensor system with published work on detection of BPA using various sensing elements (aptamer-based sensors, biomolecule-free methods and enzyme-based sensors and transducer materials. [299–306]..

$$i_p = 21.11 \pm 0.621 \times [BPA] + 3.55 \qquad Equation\ 1$$

Table 1: Performance of sensors for detection of using different sensing elements BPA

Sensor components	LOD (pg/mL or M) and linear range	Reference
BPA binding aptamer, its complementary DNA and methylene blue	0.284 pg/mL, 0.1 – 1000 pg/mL	[307]
Tyrosinase onto a nanocomposite of reduced graphene oxide and chitosan	0.74 nM, 0.01 – 50 µM	[307]
Manganese peroxidase enzyme onto a PANI nanocomposite grafted with PMMA and TiO$_2$ nanoparticles	0.17 nM, (0.2 – 1.2 nM)	This study
A nanocomposite of β-cyclodextrin (β-CD), reduced graphene oxide and gold nanoparticles	0.003 µM, 0.01 – 50 µM	[308]

4. Conclusion

A novel polyaniline (PANI) nanocomposite with grafted poly(methyl methacrylate) and titanium dioxide nanoparticles was used as an electron mediator and a receiving support for the enzyme manganese peroxidase, towards construction of a nanobiosensor system for quantification of bisphenol A. The performance of the biosensor system was investigated using cyclic voltammetry and square wave voltammetry where a low detection limit of 0.17

nM (0.039 pg/mL) was achieved at good sensitivity. These results implicate the potential of

the nanobiosensor system towards quantification of BPA in real samples.

UNIVERSITY *of the*

WESTERN CAPE

5. References

224.   Piro, B., Shi, S., Reisberg, S., Noël, V. & Anquetin, G. Comparison of electrochemical immunosensors and aptasensors for detection of small organic molecules in environment, food safety, clinical and public security. *Biosensors.* 6(1), 1-22 (2016).

225.   Srivasava, R.K. & Godara, S. Use of polycarbonate plastic products and human health. *Int. J. Basic Clin. Pharm*. 2(1), 12-17 (2013).

226.   Ng, F., Couture, G., Philippe, C., Boutevin, B. & Caillol, S. Bio-Based Aromatic Epoxy Monomers for Thermoset Materials. *Molecules.* 22, 1-48 (2017).

227.   Roen, E. L., Wang, Y., Calafat, A.M., Wang, S., Margolis, A., Herbstman, J., Hoepner, L.A., Rauh, V. & Perera, F.P. Bisphenol A exposure and behavioral problems among inner city children at 7-9 years of age. *Environ. Res.* 142, 739–745 (2015).

228.   Lee, B.E., Park, H., Hong, Y.C., Ha, M., Kim, Y., Chang, N., Kim, B.N., Kim, Y.J., Yu, S.D. & Ha, E.H.. Prenatal bisphenol A and birth outcomes: MOCEH (Mothers and Children's Environmental Health) study. *Int. J. Hyg. Environ. Health.* 217, 328–334 (2014).

229.   Rancière, F., Lyons, J.G., Loh, V.H., Botton, J., Galloway, T., Wang, T., Shaw, J.E. & Magliano, D.J.. Bisphenol A and the risk of cardiometabolic disorders: a systematic review with meta-analysis of the epidemiological evidence. *Environ. Health* 14**,** 1-23 (2015).

230.   Rochester, J. R. Bisphenol A and human health: A review of the literature. *Reprod. Toxicol.* 42, 132–155 (2013).

231.   Manfo, F. P. T., Jubendradass, R., Nantia, E. A., Moundipa, P. F. & Mathur, P. P. Adverse effects of bisphenol A on male reproductive function. *Rev. Environ. Contam. Toxicol.* 228, 57–82 (2014).

232.   Li, X., Gao, Y., Wang, J., Ji., G., Lu, Y., Yang, D., Shen, H., Dong, Q., Pan, L., Xiao,

H. & Zhu, B. Exposure to environmental endocrine disruptors and human health. *Public Heal. Emerg.* 1, 1-11 (2016).

233.   Chen, Z., Zuo, X., He, D., Ding, S., Xu, F., Yang, H., Jin, X., Fan, Y., Ying, L., Tian, C. & Ying, C. Long-term exposure to a 'safe' dose of bisphenol A reduced protein acetylation in adult rat testes. *Sci. Rep.* 7, 40337 (2017).

234.   Teeguarden, J. G. Twaddle, N.C., Churchwell, M.I., Yang, X., Fisher. J.W., Seryak, L.M., Doerge, D.R. 24-hour human urine and serum profiles of bisphenol A: Evidence against sublingual absorption following ingestion in soup. *Toxicol. Appl. Pharmacol.* 288, 131–142 (2015).

235.   Miao, M, Yuan, W., Yang, F., Liang, H., Zhou, Z., Li, R., Gao, E. & Li, D.K. Associations between bisphenol a exposure and reproductive hormones among female workers. *Int. J. Environ. Res. Public Health.* 12, 13240–13250 (2015).

236.   Vandenberg, L. N., Gerona, R.R., Kannan, K., Taylor, J.A., van Breemen, R.B., Dickenson, C.A., Liao, C., Yuan, Y., Newbold, R.R., Padmanabhan, V., Vom Saal, F.S. & Woodruff, T.J. A round robin approach to the analysis of bisphenol A (BPA) in human blood samples. *Environ. Health* 13, 1-20 (2014).

237.   Xu, J., Li, Y., Bie, J., Jiang, W., Guo, J., Luo, Y., Shen, F. & Sun, C. Colorimetric method for determination of bisphenol A based on aptamer-mediated aggregation of positively charged gold nanoparticles. *Microchim. Acta* 182, 2131–2138 (2015).

238.   Ghazali, F. M. & Johari, W. L. W. The occurrence and analysis of bisphenol A (BPA) in environmental samples – a review. *J. Biochem. Microbiol. Biotechnol.* 3, 30–38 (2015).

239.   McCracken, K. E., Tat, T., Paz, V. & Yoon, J.-Y. Smartphone-based fluorescence detection of bisphenol A from water samples. *RSC Adv.* 7, 9237–9243 (2017).

240.   Arabali, V., Ebrahimi, E., Gheibi, S., Khaleghi, F., Bijad, M., Ali Rudbaraki, A.,

Abbasghorbani, M., Ganjali, M.R.. Bisphenol A Analysis in Food Samples Using Modified Nanostructure Carbon Paste Electrode as a Sensor. *Food Anal. Methods* 9(6), 1763-1769 (2015).

241.   Mikolajewska, K., Stragierowicz, J. & Gromadzinska, J. Bisphenol A - Application, sources of exposure and potential risks in infants, children and pregnant women. *Int. J. Occup. Med. Environ. Health.* 28(2), 209–241 (2016).

242.   Najafi, M., Khalilzadeh, M. A. & Karimi-Maleh, H. A new strategy for determination of bisphenol A in the presence of Sudan i using a ZnO/CNTs/ionic liquid paste electrode in food samples. *Food Chem.* 158, 125–131 (2014).

243.   Omer, L., Ahmed, H & Elbashir, A. Determination of bisphenol A in exposed bottled water samples to direct sun light using multi walled carbon nanotubes as solid phase extraction sorbent. *J. Env. Chem. Ecotoxic.* 8(7), 51–57 (2016).

244.   Hammad, Y., Awad, F.M. & Abdelgadir, W.S.A. Determination Amount of Bisphenol A in Drugs and Water Drinking Container in Khartoum State, Sudan. *Int. J. Nutr. Food Sci.* 4(6), 609-612 (2015).

245.   Ndlovu, T., Arotiba, O. A., Sampath, S., Krause, R. W. & Mamba, B. B. An exfoliated graphite-based bisphenol a electrochemical sensor. *Sensors.* 12, 11601–11611 (2012).

246.   Rizarullah, Suryani, Ambarsari, L. & Maddu, A. Biosensor H_2O_2 by Using Immobilized Horseradish Peroxidase Glutaraldehyde on Carbon Polyaniline Nanofiber Composite. *Enzym. Eng.* 5, 1–5 (2016).

247.   Wang, H., Jiang, H., Hu, Y., Li, N., Zhao, X. & Li, C. 2D MoS_2/polyaniline heterostructures with enlarged interlayer spacing for superior lithium and sodium storage. *J. Mater. Chem. A.* 5, 5383–5389 (2017).

248.   Yu, Y-Y., Zhai, D-D., Si, R-W., Sun, J-Z., Liu, X. & Yong, Y-C. Three-Dimensional

Electrodes for High-Performance Bioelectrochemical Systems. *Int. J. Mol. Sci.* 18(1), 1-25 (2017).

249.   Tiwari, I. & Singh, K. P. In Situ Synthesis of Polymer Nanocomposites from PANI/PAA/MWCNTs: Analysis and Characterization. *Int. J. Polym. Anal. Charact.* 17, 371–380 (2012).

250.   Wang, H., Wen, H., Hu, B., Fei, G., Shen, Y., Sun, L. & Yang, D. Facile approach to fabricate waterborne polyaniline nanocomposites with environmental benignity and high physical properties. *Sci. Rep.* 7, 1-12 (2017).

251.   Vidyadihara, Malipatil, B., Sharanappa, N. & Limbitot, M. Structural Characterization of TiO_2 Doped Polyaniline. *Int. J. Emerg. Tech.* 7, 123–126 (2016).

252.   Jia, X-S., Tang, C-C., Yan, X., Yu, G-F., Li, J-T., Zhang, H-D., Li, J-J., Gu, C-Z. & Long, Y-Z. Flexible Polyaniline / Poly (methyl methacrylate) Composite Fibers via Electrospinning and In Situ Polymerization for Ammonia Gas Sensing and Strain Sensing. 2016, 1-8 (2016).

253.   Zhang, F., Cao, H., Yue, D., Zhang, J. & Qu, M. Enhanced Anode Performances of Polyaniline–TiO_2–Reduced Graphene Oxide Nanocomposites for Lithium Ion Batteries. *Inorg. Chem.* 51, 9544–9551 (2012).

254.   Nunes, D., Pimentel, A., Santos, L., Barquinha, P., Fortunato, E. & Martins, R. Photocatalytic TiO_2 Nanorod Spheres and Arrays Compatible with Flexible Applications. *Catalysts.* 7, 1-18 (2017).

255.   Truppi, A., Petronella, F., Placido, T., Striccoli, M., Agostiano, A., Curri, M.L. & Visible-Light-Active TiO_2-Based Hybrid Nanocatalysts for Environmental Applications. *Catalysts.* 7(4), 1-33 (2017).

256.   Dai, H., Zhang, S., Hong, Z., Li, X., Xu, G., Lin, Y. & Chen, G. Enhanced Photoelectrochemical Activity of a Hierarchical-Ordered TiO_2 Mesocrystal and Its

Sensing Application on a Carbon Nanohorn Support Scaffold. *Anal. Chem.* 86, 6418–6424 (2014).

257.   Lin, Y., Li, D., Hu, J., Xiao, G., Wang, J., Li, W. & Fu, X. Highly Efficient Photocatalytic Degradation of Organic Pollutants by PANI-Modified TiO_2 Composite. *J. Phys. Chem. C.* 116, 5764–5772 (2012).

258.   Amini, N., Mazinani, S., Ranaei-Siadat, S.O., Kalaee, M., Niknam, K. & Adlfar, V. Manufacturing polymethyl methacrylate nanofibers as a support for enzyme immobilization. *Fibers Polym.* 13, 994–998 (2012).

259.   Gautam, R., Singh, R.D., Sharma, V.P., Siddhartha, R., Chand, P.& Kumar R. Biocompatibility of polymethylmethacrylate resins used in dentistry. *J. Biomed. Mater. Res. B Appl. Biomater.* 100(5), 1444–1450 (2012).

260.   Sidwaba, U., Feleni, U., Makelane, H., Nxusani, E., Wilson, L., Qakala, S., Rassie, C., Masikini, M., Waryo, T, Ajayi, R.F., Baker, P. & Iwuoha, E. A Novel Polyaniline Nanocomposite with Doping Effects of Poly (Methyl Methacrylate) and TiO_2 Nanoparticles. 44, 281–292 (2016).

261.   Touhami, A. Biosensors and Nanobiosensors: Design and Applications. *Nanomedicine*. 374–400 (2015). (Ch15).

262.   Abdullah, H. S. Electrochemical polymerization and Raman study of polypyrrole and polyaniline thin films. *Int. J. Phys. Sci.* 7, 5468–5476 (2012).

263.   Hu, Z., Zu, L., Jiang, Y., Lian, H., Liu, Y., Li, Z., Chen, F., Wang, X. & Cui, X.. High specific capacitance of polyaniline/mesoporous manganese dioxide composite using KI-H_2SO_4 electrolyte. *Polymers.* 7, 1939–1953 (2015).

264.   Liu, Y. D., Zhang, K., Zhang, W. L. & Choi, H. J. Conducting Material-incorporated Electrorheological Fluids: Core-shell Structured Spheres. *Aust. J. Chem.* 65, 1195–1202 (2012).

265.   Xu, Y., Shen, G., Wu, H., Liu, B., Fang, X., Zhang, D. & Zhu, J.. Double-layer microwave absorber based on nanocrystalline $CoFe_2O_4$ and $CoFe_2O_4$/PANI multi-core/shell composites. *Mater. Sci.* 35(1), 94–104 (2017).

266.   Radoman, T. S., Dzunuzovic, J.V., Grgur, B.N., Gvozdenovic, M.M., Jugovic, B.Z., Milicevic, D.S. & Dzunuzovic, E.S. Improvement of the epoxy coating properties by incorporation of polyaniline surface treated TiO_2 nanoparticles previously modified with vitamin B6. *Prog. Org. Coatings.* 99, 346–355 (2016).

267.   Babu, V. J., Vempati, S. & Ramakrishna, S. Conducting Polyaniline-Electrical Charge Transportation. *Mater. Sci. Appl.* 4, 1–10 (2013).

268.   Kaitsuka, Y. & Goto, H. UV light induces dedoping of polyaniline. *Polymers.* 8, 4–7 (2016).

269.   Humpolíček, P., Radaszkiewicz, K.A., Kašpárková, V., Stejskal, J., Trchová, M., Kuceková, Z., Vičarová, H., Pacherník, J., Lehocký, . & Minařík, A. Stem cell differentiation on conducting polyaniline. *RSC Adv.* 5, 68796–68805 (2015).

270.   Tanwar, S. & Ho, J. Green Synthesis of Novel Polyaniline Nanofibers: Application in pH Sensing. *Molecules* 20, 18585–18596 (2015).

271.   Gomes, E. C. & Oliveira, M. A. S. Chemical Polymerization of Aniline in Hydrochloric Acid (HCl) and Formic Acid (HCOOH) Media . Differences Between the Two Synthesized Polyanilines. 2, 5–13 (2012).

272.   León, A., Reuquen, P., Garin, C., Segura, R., Vargas, P., Zapata, P. & Orihuela, P.A. FTIR and Raman Characterization of TiO_2 Nanoparticles Coated with Polyethylene Glycol as Carrier for 2-Methoxyestradiol. 7(1), 1–9, 2017.

273.   Grzeszczuk, M., Grańska, A. & Szostak, R. Raman spectroelectrochemistry of polyaniline synthesized using different electrolytic Regimes-Multivariate analysis. *Int. J. Electrochem. Sci.* 8, 8951–8965 (2013).

274.   Tharani, S. & Vinayagam, S. C. Synthesis of novel cerium doped polyaniline
        multiwalled carbon nanotubes and their optical and electrochemical properties for
        supercapacitor applications. *Int. J. Adv. Res.*. 3, 810–822 (2015).

275.   Canales, M., Torras, J., Fabregat, G., Meneguzzi, A. & Alemán, C. Polyaniline
        Emeraldine Salt in the Amorphous Solid State: Polaron versus Bipolaron. *J. Phys. Chem.
        B.* 118, 11552–11562 (2014).

276.   Zeng, F., Qin, Z., Liang, B., Li, T., Liu, N. & Zhu, M. Polyaniline nanostructures
        tuning with oxidants in interfacial polymerization system. *Prog. Nat. Sci. Mater. Int.* 25,
        512–519 (2015).

277.   Mao, Y., Bao, Y., Yan, L., Li, G., Li, F., Han, D., Zhang, X. & Niu, L. pH-switched
        luminescence and sensing properties of a carbon dot–polyaniline composite. *RSC Adv.*.
        5475–5482 (2013).

278.   Chakraborty, P., Kothari, A. & Nagarajan, R. Highly ordered polyaniline as an
        efficient dye remover. *Ads. Sci. Techn.* (2017).

279.   Vedhi, P. R. C., Tga, V. Á., Sem, D. T. A. Á. & Xrd, Á. T. E. M. Á. Electrocatalytic
        properties of polyaniline–TiO_2 nanocomposites. 40, 247–259 (2015).

280.   Arora, R., Srivastav, A. & Mandal, U. K. Polyaniline Based Polymeric Nano
        composite Containing TiO_2 and SnO_2 for Environmental and Energy Applications. 2(4),
        2384-2395 (2012).

281.   Liu, Q., Nayfeh, O., Nayfeh, M. H. & Yau, S. Flexible supercapacitor sheets based on
        hybrid nanocomposite materials. *Nano Energy.* 2, 133–137 (2013).

282.   Radhapyari, K. & Khan, R. Amperometric immuno-sensor for detection of toxin
        aflatoxin B 1 based on polyaniline probe modified with Mc-IgGs- a -AFB 1 antibodies.
        Adv. Mat. Lett. 5, 435–440 (2014).

283.   Xiaomiao, F., Li, R., Ma, Y., Chen, R., Mei, Q., Fan, Q. & Huang, W. Nitrogen-

doped carbon nanotube / polyaniline composite : Synthesis , characterization , and its application to the detection of dopamine. 54, 1615–1621 (2011).

284.   Li, R., Dong, X., He, C., Liu, Z., Huang, L. & Yang, Y. Graphene-Enabled Improved Supercapacitor Performance of Polyaniline Nanofiber Composites. *Int. J. Electrochem. Sci.*. 12, 144–154 (2017).

285.   Barros, S. B. A., da Silva Leite, C.M., de Brito, A.C.F., Dos Santos Junior, J.R., Zucolotto, V. & Eiras, C.. Multilayer Films Electrodes Consisted of Cashew Gum and Polyaniline Assembled by the Layer-by-Layer Technique: Electrochemical Characterization and Its Use for Dopamine Determination. *Int. J. Anal. Chem.* 2012, 1–10 (2012).

286.   Mahla, D. K., Bhandari, S., Rahaman, M. & Khastgir, D. Morphology and cyclic voltammetry analysis of in situ polymerized polyaniline / graphene composites. *Electrochem. Sci. Eng.* 3, 157–166 (2013).

287.   Wu, T., Li, W., Kuo, C., Chou, C., Liao, J., Chen, H. & Tseng, C. Study of Poly (Methyl Methacrylate) -Based Gel Electrolyte for Electrochromic Device. *Int. J. Electrochem. Sci.* 8, 10720–10732 (2013).

288.   Obaid, A., El-Mossalamy, E.H., Al-Thabaiti, S.A., El-Hallag, I.S., Hermas, A.A. & Asiri, A.M. Electrodeposition and characterization of polyaniline on stainless steel surface via cyclic, convolutive voltammetry and SEM in aqueous acidic solutions. *Int. J. Electrochem. Sci.* 9, 1003–1015 (2014).

289.   Mangombo, Z., Key, D., Iwuoha, E. I. & Baker, P. G. L. Development of L-phenylalanine biosensor and its application in the real samples. *Insciences J.* 3, 1–23 (2013).

290.   Fonseca, C. P., Almeida, D. A. de L., Oliveira, M. C. D. de, Baldan, M. R. & Ferreira, N. G. Influence of the polymeric coating thickness on the electrochemical performance of

Carbon Fiber/PAni composites. *Polímeros.* 25, 425–432 (2015).

291.   Peng, J., Feng, Y., Han, X. X. & Gao, Z. N. Simultaneous determination of bisphenol
        A and hydroquinone using a poly(melamine) coated graphene doped carbon paste
        electrode. *Microchim. Acta.* 183, 2289–2296 (2016).

292.   Vikas, V., Swamy, B.E.K., Viswanath, C.C. & Naik, T.S.S. Electrochemical Studies
        of Bisphenol-A at Sodium Alpha Olefin Sulfonate Modified Carbon Paste Electrode : A
        Voltammetric Study. *Anal. Bioanal. Electrochem. 9(2),* 164–173 (2017).

293.   Wang, N., Zhao, H. Y., Ji, X. P., Li, X. R. & Wang, B. B. Gold nanoparticles-
        enhanced bisphenol A electrochemical biosensor based on tyrosinase immobilized onto
        self-assembled monolayers-modified gold electrode. *Chinese Chem. Lett.* 25, 720–722
        (2014).

294.   Zhang, J., Yang, B., Guo, Z., Song, Q., Ye, X. & Zheng, S. Nickel Oxide
        Nanoparticles Immobilized on MWCNTs/PANI Composite Film as an Electron Transfer
        Facilitator for Horseradish Peroxidase: Direct Electron Transfer and H_2O_2 Determination.
        J. Electrochem. Soc. 164(5), B3001–B3007 (2017).

295.   Radhapyari, K. & Khan, R. Biosensor for detection of selective anticancer drug
        gemcitabine based on polyaniline-gold nanocomposite. *Adv. Mater. Lett.* 6, 13–18 (2015).

296.   Sunday, C. E., Masikini, M., Wilson, L., Rassie, C., Waryo, T., Baker, P.G. &
        Iwuoha, E.I. Application on gold nanoparticles-dotted 4-nitrophenylazo graphene in a
        label-free impedimetric deoxynivalenol immunosensor. *Sensors..* 15, 3854–3871 (2015).

297.   Ajayi, R. F., Nxusani, E., Douman, S.F., Jonnas, A., Ntshongontshi, N., Feleni, U.,
        Pokpas, K., Wilson, L. & Iwuoha, E.I. Silver Nanoparticle-Doped Poly(8-Anilino-1-
        Naphthalene Sulphonic Acid)/CYP2E1 Nanobiosensor for Isoniazid - A First Line Anti-
        Tuberculosis Drug. *J. Nano Res.* 44, 229–251 (2016).

298.   Peng, J., Feng, Y., Han, X.-X. & Gao, Z.-N. Simultaneous determination of bisphenol

A and hydroquinone using a poly(melamine) coated graphene doped carbon paste electrode. *Microchim. Acta.* 183, 2289–2296 (2016).

299.   Chen, Z., Tang, C., Zeng, Y., Liu, H., Yin, Z. & Li, L. Determination of Bisphenol A Using an Electrochemical Sensor Based on a Molecularly Imprinted Polymer-Modified Multiwalled Carbon Nanotube Paste Electrode. *Anal. Lett.* 47(6), 996–1014 (2014).

300.   Ezoji, H. & Rahimnejad, M. Electrochemical Determination of Bisphenol A on Multi-Walled Carbon Nanotube/ titanium dioxide Modified Carbon Paste Electrode. **7,** 242–246 (2016).

301.   Zheng, Z., Liu, J., Wang, M., Cao, J., Li, L., Wang, C. & Feng, N. Selective Sensing of Bisphenol A and Bisphenol S on Platinum/Poly(diallyl dimethyl ammonium chloride)-diamond Powder Hybrid Modified Glassy Carbon Electrode. *J. Electrochem. Soc.* 163, B192–B199 (2016).

302.   Ntsendwana, B., Mamba, B. B., Sampath, S. & Arotiba, O. A. Electrochemical Detection of Bisphenol A Using Graphene- Modified Glassy Carbon Electrode. *Int. J. Electrochem. Sci.* 7, 3501–3512 (2012).

303.   Zhu, Y., Cai, Y., Xu, L., Zheng, L., Wang, L., Qi, B. & Xu, C. Building An Aptamer/Graphene Oxide FRET Biosensor for One-Step Detection of Bisphenol A. *ACS Appl. Mater. Interfaces* **7,** 7492–7496 (2015).

304.   Yildirim, N., Long, F., He, M., Shi, H.-C. & Gu, A. Z. A portable optic fiber aptasensor for sensitive, specific and rapid detection of bisphenol-A in water samples. *Environ. Sci. Process. Impacts* 16, 1379–1386 (2014).

305.   Portaccio, M., Tuoro, D.D., Arduini, F., Moscone, D., Cammarota, M., Mita, D.G. & Lepore, M. Laccase biosensor based on screen-printed electrode modified withthionine-carbon black nanocomposite, for Bisphenol A detection. *Electrochim. Acta* 109, 340–347 (2013).

http://etd.uwc.ac.za

306. Dong, X., Qi, X., Liu, N., Yang, Y. & Piao, Y. Direct Electrochemical Detection of Bisphenol A Using a Highly Conductive Graphite Nanoparticle Film Electrode. *Sensors* 17(4), 1-10 (2017).

307. Xue, F., Wu, J., Chu, H. Mei, Z., Ye, Y., Liu, J., Zhang, R., Peng, C., Zheng, L. & Chen, W. Electrochemical aptasensor for the determination of bisphenol A in drinking water. 180, 109-115 (2012).

308. Yun, Y. Electrochemical Sensor for Ultrasensitive Determination of Bisphenol A based on Gold Na noparticles / β -cyclodextrin Functionalized Reduced Graphene Oxide Nanocomposite. *Int. J. Electrochem. Sci.* 11, 2778–2789 (2016).

UNIVERSITY *of the*
WESTERN CAPE

103

Chapter 4

Gold nanoparticles amplified properties of poly(3,4-propylenedioxythiophene)

ABSTRACT

A poly(3,4-propylenedioxythiophene) (PProDOT) nanocomposite with gold nanoparticles, achieved by exploiting the gold-thiol surface chemistry between the two components is reported. A distinct change is observed in the PProDOT prepared in absence and presence of a surfactant, sodium dodecyl sulfate. The effects of AuNPs on optical and electrochemical behaviour of the PProDOT were investigated using UV-Vis, voltammetry (CV and DPV) and chronocoulometry. The better reversibility and improved electrical conductivity observed for the nanocomposite are attributed to the incorporated high surface area gold nanoparticles.

KEYWORDS: poly(3,4-propylenedioxythiophene), conducting polymer nanocomposite, gold nanoparticles, electrical conductivity

1. Introduction

Conducting polymers (CPs) in composite form with nanomaterials still have undivided attention emanating from the superior performance of their devices induced by the synergistic effect of combining the unique properties of each component. Ever since the emergence of the 'nano' technology, various efforts have been carried out towards synthesis of nanoscaled polymers as the nano-dimensions give materials outstanding properties. Besides the easy, cost-effective and easily accessible preparation methods of CPs, their chemical structures allow facile functionalization with a wide range of materials through various coupling mechanisms including covalent bonding and electrostatic interaction [309,310]. Hence, the different materials, especially nanomaterials, are incorporated into CPs to further enhance the properties of CPs and manufacture special material for specific applications [311–314].

Poly(3,4-propylenedioxythiophene) (PProDOT) is a conducting polymer derived from polythiophene as an addressing measure to overcome the limitations of polythiophene, amongst which is insolubility. However, there came an era where the properties of the PProDOT itself became unsatisfactory for certain applications. As a result, various strategies have been developed to enhance its properties. One of these strategies includes further functionalization of the monomer, catered for by the propyl group extending the thiophene ring. A library of monomers derived from the monomer 3,4-propylenedioxythiophene (ProDOT) functionalized or substituted with various molecules, based on satisfying certain needs towards various applications, have been reported [162, 188, 315, 316]. Other strategies include co-polymerization with other monomers and incorporation of nanomaterials such as manganese oxide, tin oxide and titanium dioxide nanoparticles [138,195, 317, 318].

Gold nanostructures are noble gold metal nanoparticles characterized by unique properties such biocompatibility, high electrical conductivity and signature surface plasmon resonance. They can be easily prepared through different methods into various shapes including

nanoparticles (or nanospheres), nanorods, nanotubes and nanostars [319]. Gold nanoparticles (AuNPs) are among the most applied gold nanostructures due to their biocompatibility and shape which merits their cellular internalization as therapeutic agents. Thus, AuNPs have been applied in energy devices, sensors, nanomedicine and therapeutics [319,320].

During biosensor fabrication, CP nanocomposites have shown excellent behaviour as electron shuttles and biomolecule hosts. Herein, a gold nanoparticles-based PProDOT nanocomposite is presented as a proof of concept that will be further investigated in the future to explore different properties and parameters including the type and amount of surfactant, cycling stability of the nanocomposite, effect of AuNPs amount in the nanocomposite performance and preparation using other polymerization methods.

2. **Experimental section**

2.1. Reagents

All reagents used were of analytical grade and purchased from Sigma Aldrich (South Africa) and used without further purification: 3,4-propylenedioxythiophene (ProDOT), gold chloride trihydrate (HAuCl$_4$·3H$_2$O), acetonitrile, sodium citrate trihydrate, sodium dodecyl sulfate (SDS), hydrochloric acid (HCl) and lithium perchlorate (LiClO$_4$).

2.2. Morphological view

The morphology of the polymer and its nanocomposite was investigated using a Hitachi S3000N scanning electron microscope at an acceleration voltage of 5 kV and a Tecnai G2 F20X-Twin MAT high resolution transmission electron microscope (HR-TEM) at an acceleration voltage of 200 kV. SEM studies do not only give estimated nature and size of the material but also have the potential to clearly show how the dopants are attached to the polymer

106

backbone while the TEM gives an internal view of such arrangements at different magnifications.

2.3. Energy absorption

The ultraviolet-visible (UV-Vis) spectra of PProDOT and its nanocomposite were recorded on a Nicolet Evolution 100 spectrophotometer within wavelength limits between 230 nm and 950 nm in ethanol. PProDOT has been proven to exhibit high optical activity where it absorbs energy at different wavelengths of the spectrum and has gained application in electrochromic devices following the tuning of its optical properties through incorporation of different chromophores to its backbone and functionalization of the monomer. Therefore, this technique will allow identification of incorporated or foreign chromophores to PProDOT based on alterations in its absorbance wavelengths.

2.4. Electron transfer capability

Electrochemical measurements investigating the electron transfer behaviour of PProDOT and the nanocomposite were performed using a CHI 760E electrochemical workstation and a conventional three-electrode system with a glassy carbon working electrode (GCE; surface area = 0.071 cm^2), Ag/AgCl (3 M NaCl) reference electrode and a platinum wire counter electrode. Prior to use, the working electrode was pre-conditioned by polishing in micro-alumina slurries of 1.0 µm, 0.3 µm and 0.05µm, followed by ultrasonication for five minutes in ethanol and water, respectively. All experiments were conducted in 6-ml electrolyte solutions.

The electrochemical transitions of the nanocomposite were explored by CV cycling between -800 mV and +1300 mV (vs Ag/AgCl) at varying rates from 1 mV/s and 8 mV/s. Using electrochemistry, electrode interface significant parameters such as the diffusion coefficient, surface concentration and the number of electrons transferred during reduction-

107

oxidation processes can be determined as these parameters play a crucial role towards performance of different devices employing them.

2.5. Oxidative chemical polymerization of PProDOT

2.5.1.   Template-free synthesis of PProDOT

An acetonitrile solution of ProDOT was mixed with a 0.1 M HCl solution to a final solution yielding a clear solution containing 26.7 mg/mL of ProDOT. The solution was slowly stirred at room temperature, followed by addition of 15 mM auric chloride solution. The solution immediately turned to green with visible precipitates forming. The reaction was stopped after 1 hour. The polymer was obtained as a bluish green powder. To investigate the effect of temperature, the same procedure was followed by heating the ProDOT monomer solution to boil at 116 ºC (the optimum temperature for the synthesis of AuNPs) followed by addition of the oxidizing agent.

2.5.2.   Surfactant-templated PProDOT polymerization at room temperature

Sodium dodecyl sulfate was chosen as a surfactant towards preparation of a growth-directed PProDOT. The SDS was mixed with the monomer solution to a final concentration of 0.04 M. After addition of the oxidizing auric chloride, the solution changed from clear to dark purplish blue. It was also noted that a higher yield was obtained than with the surfactant-free PProDOT. This polymer will be referred to as SDS-PProDOT. The schematic presentation for the polymerization of PProDOT from its monomer is shown in Figure 21.
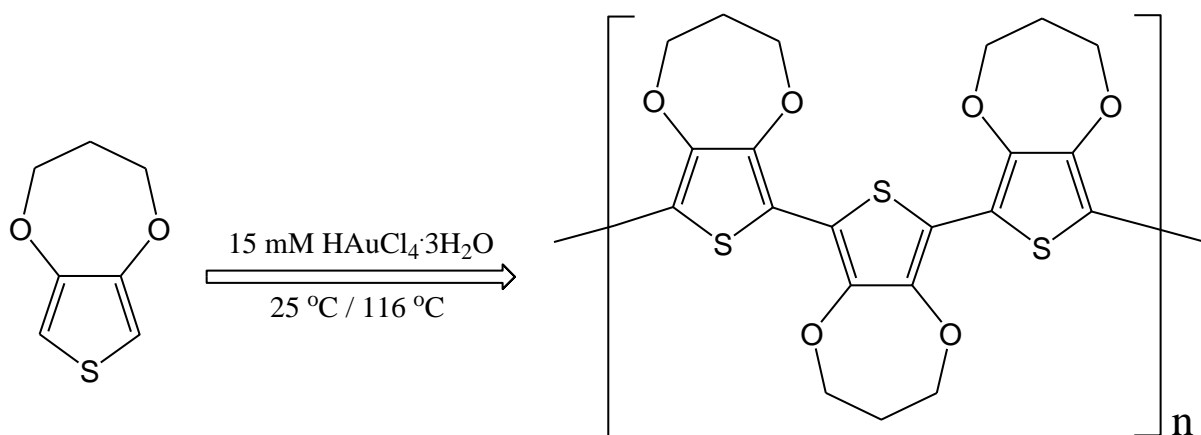
Figure 21: General schematic presentation for the polymerization of PProDOT to its neutral state.

2.6. Synthesis of citrate stabilized gold nanoparticles

Gold nanoparticles (AuNPs) were prepared through the citrate reduction method as documented in literature. An auric chloride solution of 0.25 mM in 50 mL purified water was heated to boil. This solution showed a clear yellow colour. Under continuous stirring, 1mL of 0.1 M sodium citrate was rapidly added. The solution first changed from clear yellow to purple and then to wine red. The AuNPs colloidal solution was purified and kept at 4 ºC.

2.7. One-pot polymerization of the PProDOT-AuNPs nanocomposite

The nanocomposite was prepared at room temperature in the presence of readily prepared AuNPs and SDS under the same conditions as for the SDS-PProDOT. The AuNPs and ProDOT were mixed together for 1 hour under ultrasonication to get adsorption between the two starting materials. The ProDOT initial concentration was maintained at 0.04 M.

109

2.8. Fabrication of the PProDOT and PProDOT-AuNPs film

All electrochemical characterizations were conducted on the SDS-templated PProDOT. Films of the SDS-PProDOT and the PProDOT-AuNPs were drop casted onto glassy carbon electrodes from pastes of the polymer powders in acetonitrile which was chosen because of its high evaporation rate. Layers of 3 µL were fabricated once and twice, to observe any effects of film thickness on its properties. During the investigation of such properties, the single layered and double layered films are denoted as PProDOT-*m* and PProDOT-b, with the letters *m* and *b* representing the first letters of monolayer and bilayer, respectively. For comparison with the nanocomposite, the SDS-PProDOT will only be referred to as PProDOT while in composite form with AuNPs it will be referred to as PProDOT-AuNPs.

3.   Results and discussion

3.1. PProDOT

3.1.1.   Morphological view

3.1.1.   (a). Surfactant-free PProDOT

The surface morphologies of the PProDOT samples prepared without a surfactant or template at room temperature and at 116 ºC were investigated using SEM and TEM. SEM and TEM images of the room temperature-prepared PProDOT (which will be referred to as PProDOT-RT) are shown in Figure 22 below. The SEM image reveals a tubular morphology that might result from closely packed spheres as can be seen from the ends of the tubular structures. The TEM reveals structures resembling short sticks with sharp ends. These sticks have defined mean diameters (≤ 20 nm) and lengths (ranging between 60 nm and 150 nm). Vertically aligned sticky nanofibres of superhydrophobicity have been prepared from ProDOT derivatives using cyclic voltammetry as a polymer deposition tool [321].
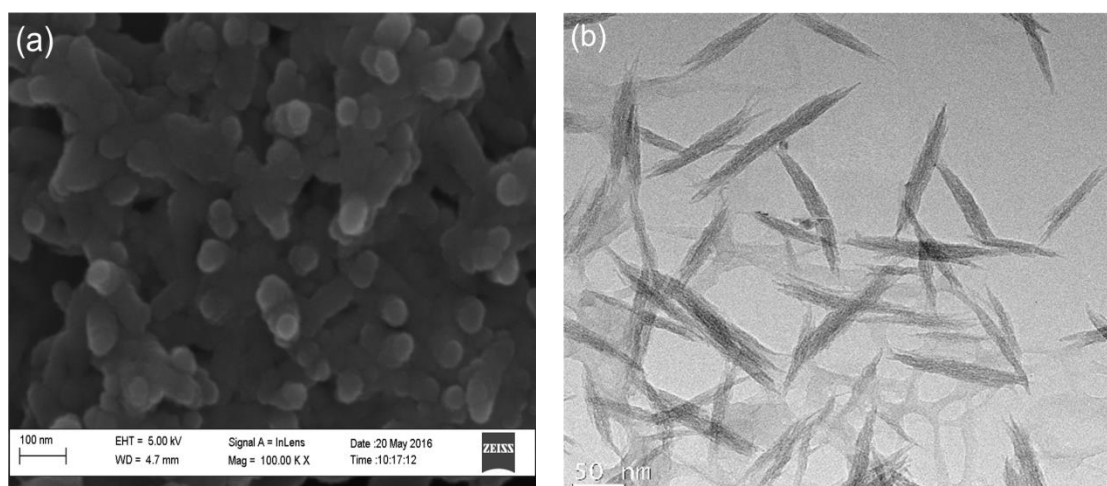
Figure 22: (a) SEM and (b) TEM images of the surfactant-free PProDOT prepared at room temperature.

A similar morphology (Figure 23) is revealed by the PProDOT prepared at 116 ℃ (which will be referred to as PProDOT-116). The SEM image of PProDOT-116 reveals some kidney-shaped and elliptical structures which are broader than the PProDOT-RT tubular structures and spheres. The TEM confirms changes induced by heat where PProDOT-116 exhibits pod-shaped structures of approximately ≤25 nm in width and lengths ranging between 50 nm and 125 nm. From the SEM results, it may be concluded that a higher temperature prevents chain formation or causes the polymer to degrade, provided that the tubular structures in the PProDOT-RT were polymer chains while the TEM results shows that PProDOT exposure to a temperature higher than room temperatures yields well defined pod-like structured polymer. Should this phenomenon be associated with polymer degradation, the result would be in agreement with literature [322] but further investigations are still needed.
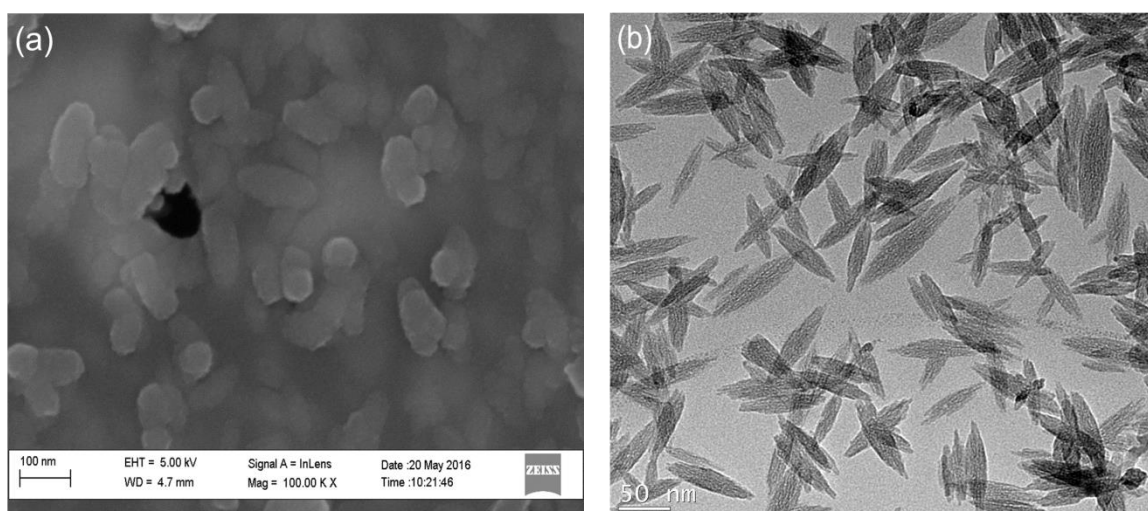
Figure 23: SEM (a) and TEM (b) images of the surfactant-free PProDOT prepared at 116 °C.

3.1.1.   (b). SDS-templated PProDOT

Some of the key limitations of CPs have been their insolubility in certain solvents, poor thermal

stability and their compact structures that retard ion diffusion hence minimizing the

performance of relative energy devices [323,324]. Hence, strategies such as designing the

morphology of the structures by using templates and incorporation of surfactants into CPs
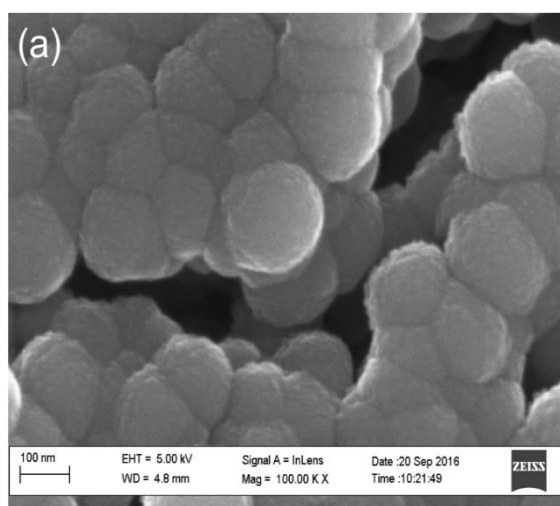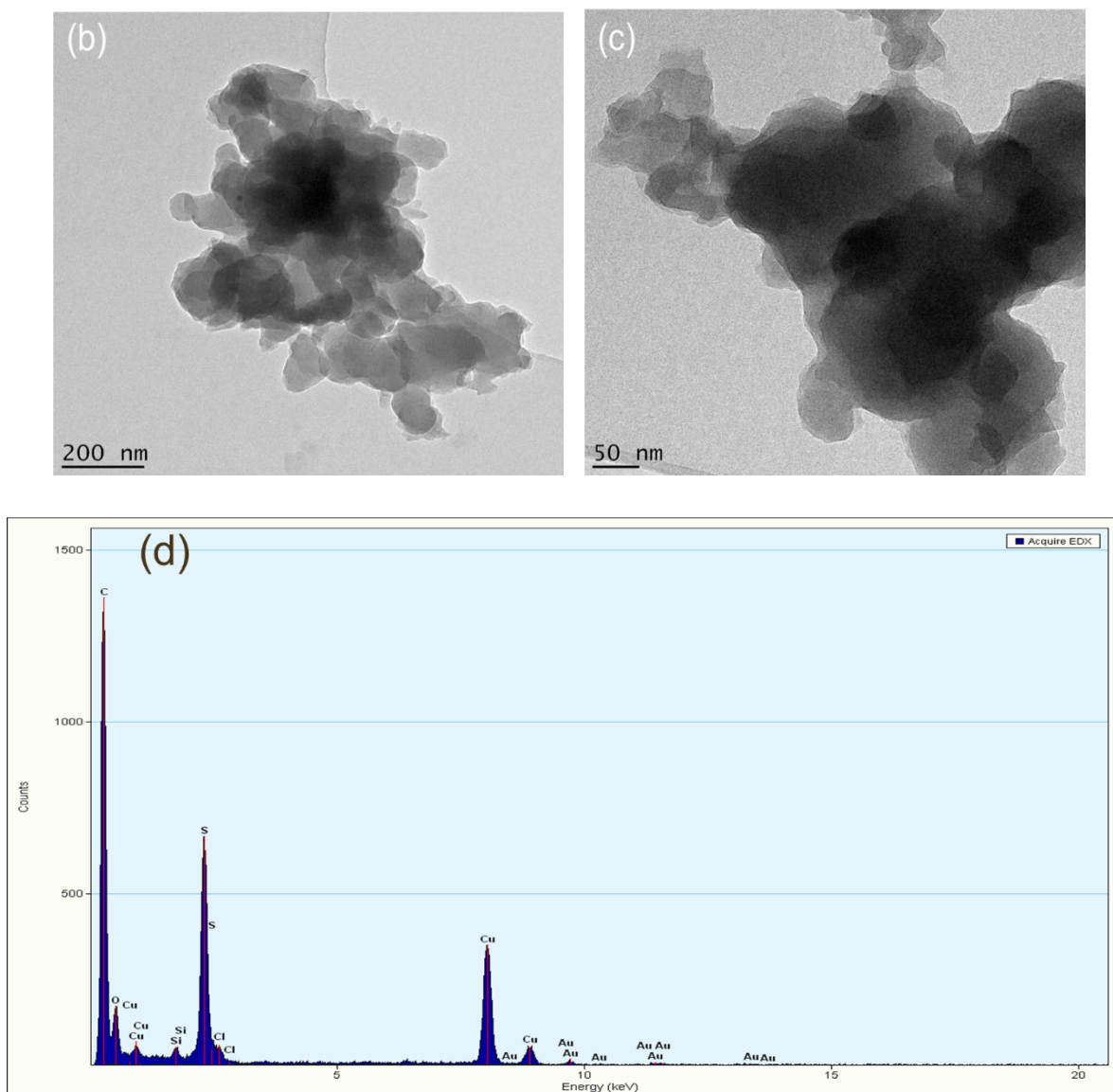
Figure 24: (a) SEM image, (b), (c) TEM images under different magnifications and (d) EDS spectrum of the SDS-templated PProDOT.

addressed the limitations mentioned here [325,326]. Sodium dodecylsulfate (SDS)-templated PProDOT (SDS-PProDOT) shows a totally different morphology from both PProDOT-RT and PProDOT-116 prepared without a surfactant or template. The SEM image (Figure 24(a))) shows globular particles of around 125 nm being closely packed in such a way that squeezes the middle ones into irregular-shaped structures. From the TEM (Figure 24(b) and (c)), an irregular sponge-like morphology was revealed. The nanospherical morphology revealed by

113

the SEM is accredited to the SDS incorporation which confines the morphology of the resulting polymer [327,328]. Similar irregular morphologies investigated by TEM have been evidenced in literature for PProDOT [183] while spherical nanoparticles have found for a polyaniline nanocomposite prepared in the presence of sodium dodecylbenzene sulfonate (SDBS) as a surfactant and a template [193].The energy dispersive X-ray spectrum (Figure 24(d)) depicted presence of gold (Au) in the SDS-PProDOT (Silicon (Si) and copper (Cu) came from the preparation grids). Then, the back-scattered electron detector was employed to investigate metal distribution. The subsequent back-scattered electron SEM image (Figure 25(a)) shows the bright spots corresponding to Au in the sample. This was further confirmed by the TEM at higher magnification (Figure 25(b)) in which evenly distributed dots of approximately 2.5 nm diameters are evident. From the distribution of these particles, it was then concluded that during synthesis, bulk Au got attached to the thiophene ring of PProDOT following the gold-thiol (Au-S) chemistry while the chloride ions reside closely to the carbon atom. The proposed polymer structure is shown in Figure 26.
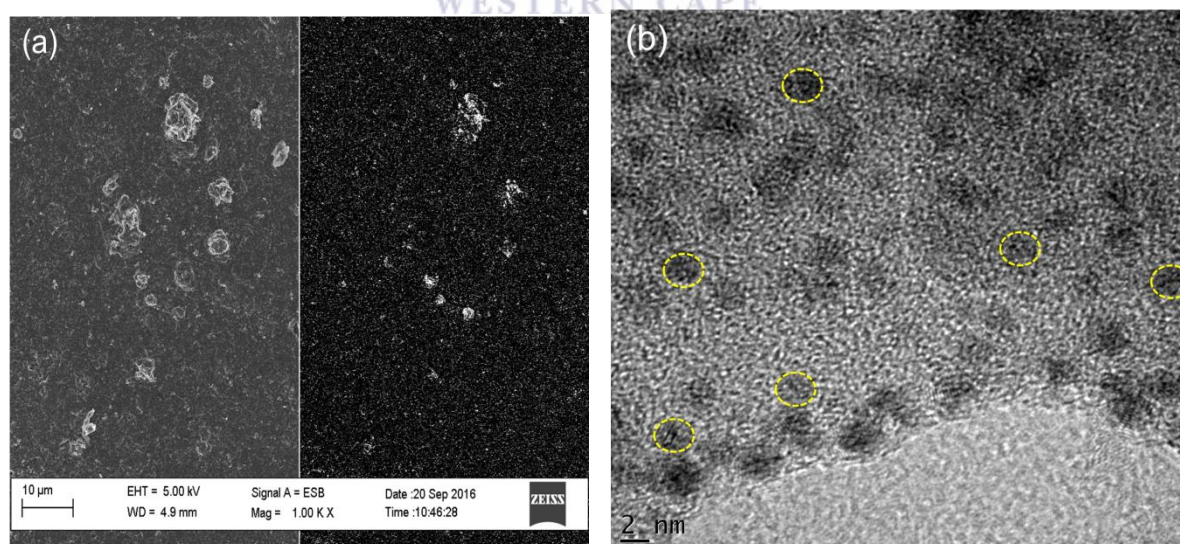

Figure 25: (a) Back scatted electron SEM image and (b) a high magnification TEM image of the SDS-PProDOT obtained in the presence of SDS.
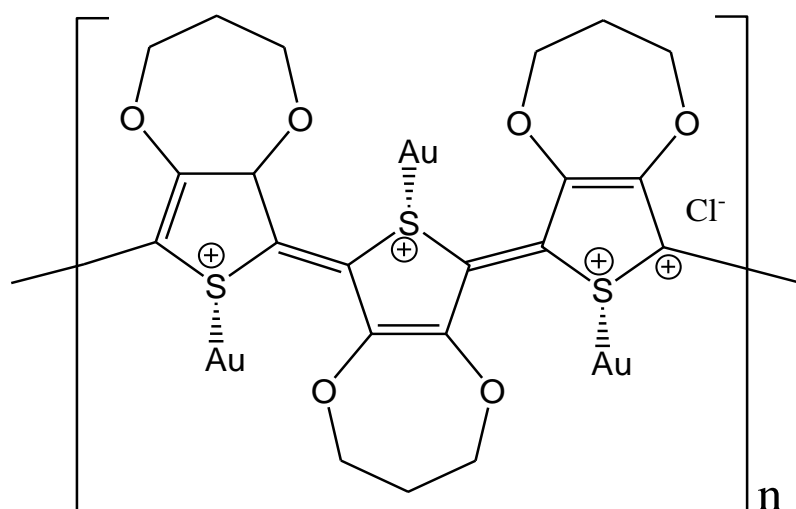
Figure 26: The proposed structural backbone of the SDS-PProDOT depicting the Au-S bonding and the chloride anion acting as a dopant residing closely to the carbon proton.

3.1.2. Energy absorption properties

The absorbance properties of PProDOT-RT are shown in Figure 27. Within the chosen wavelength range, PProDOT exhibits characteristic absorbance bands of carbon-carbon double bonds inducing the π-π* transitions appearing as a shoulder at 355 nm while the transitions of polarons and bipolarons induce the transitions at 477 nm and 759 nm, respectively [329]. With reference to similar conjugated polymers, these transitions are ascribed to the aromatic (red) and quinoid (blue) units forming the polymer backbone [330,331] depicted by different colours in the insert in Figure 27 (a).

PProDOT-116 exhibits slight deviations by absorbing light at 358 nm resulting from π-π* transitions. Polaron transitions show maximum absorbance at 410 nm and 497 nm, a phenomenon that may be associated with the polymer segments of different conjugation lengths, hence distributing the polarons at different sites along the conjugated polymer chain. Similarly to PProDOT-RT, PProDOT-116 also shows the free-carrier tail centred around 750-850 nm, resulting from bipolaronic transitions [183,332]. Therefore, it may be deduced that the

PProDOT obtained using both preparation routes was obtained in its protonated conducting state.
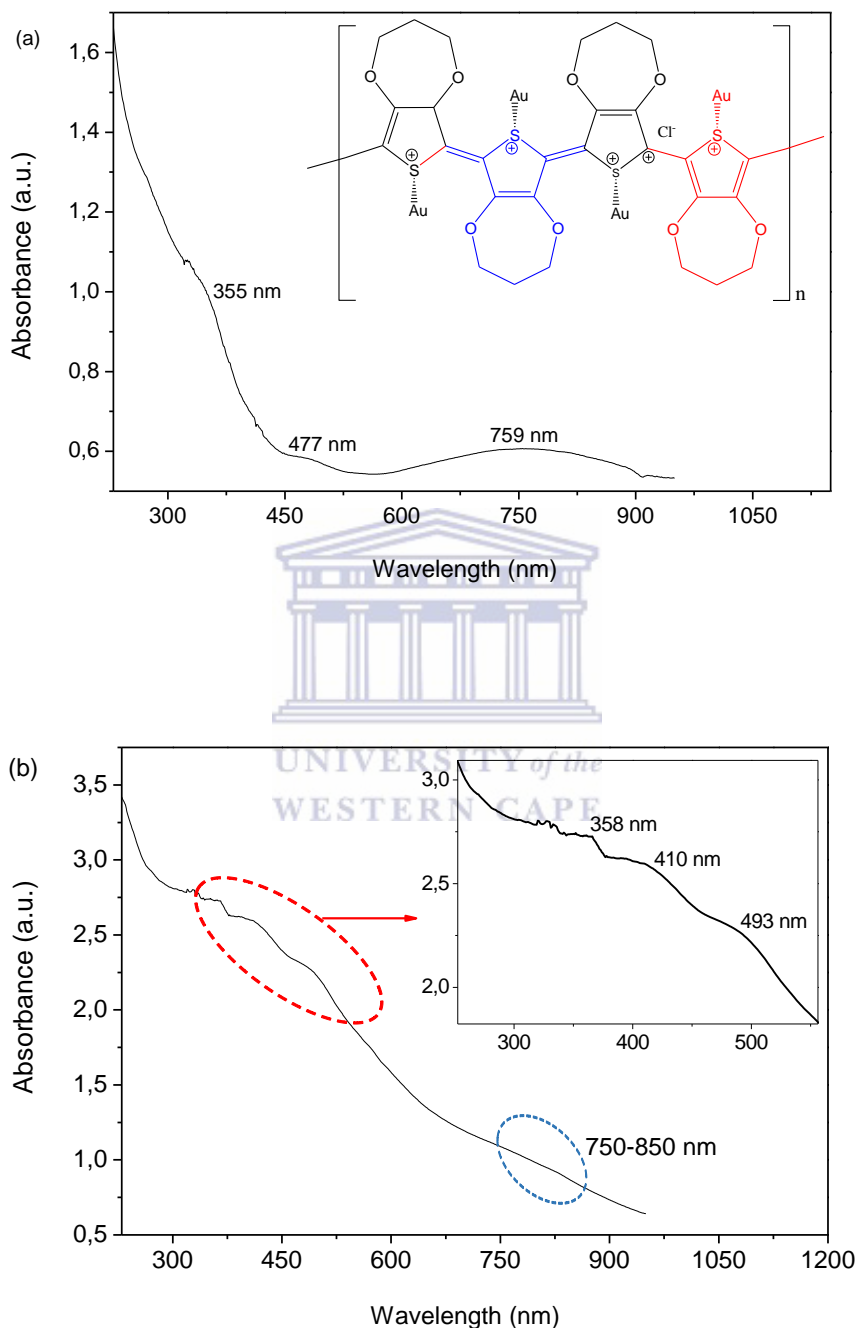

Figure 27: Energy absorption properties of (a) PProDOT-RT (insert graph represents the proposed chemical structure showing the Au-S bonding and (b) PProDOT-116 (insert graph represent is the magnified view of the red-circled area.

http://etd.uwc.ac.za

The SDS polymer (Figure 28) shows similar energy absorption bands to the PProDOT-RT which may be ascribed to the similar preparation conditions. SDS-PProDOT exhibits a pair of absorption bands with maxima at 259 nm and 296 nm, associated with the π-π* transitions and the characteristic polaron transition band at 425 nm. A zoomed-in view of the free-carrier tail shows various absorption bands at 796 nm, 878 nm and 918 nm that can be ascribed to the presence of charge carriers being distributed along the polymer chain comprising units of different conjugation lengths [142,332].
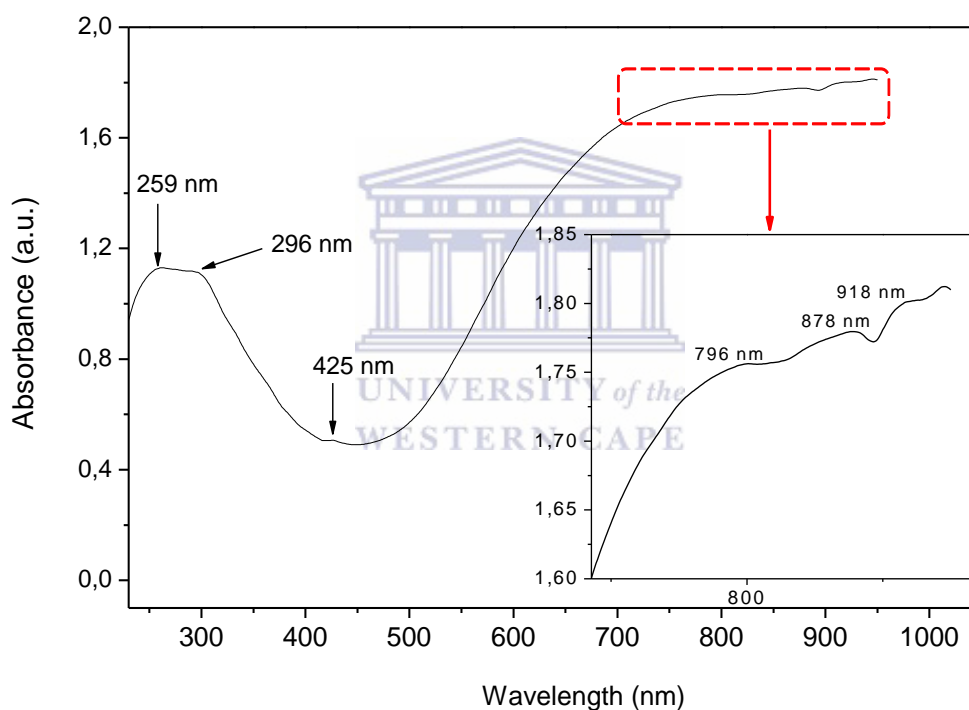
Figure 28: Energy absorption properties of the SDS-PProDOT which absorbs light at 259 nm, 296 nm and 425 nm. The free-carrier tail (the magnified view of the red-marked area shown in the insert graph) absorbs light at 796 nm, 878 nm and 918 nm..

http://etd.uwc.ac.za

3.1.3. *Electron transfer and charge storage capability of SDS-PProDOT*

The capability of the SDS-PProDOT to transfer electrons and store energy was evaluated using various electrochemical techniques including cyclic voltammetry (CV), square wave voltammetry (SWV) and chronocoulommetry (CC). The CV graph depicting the electron transfer capability of PProDOT-*m* and PProDOT-*b* is shown in Figure 29(a). Both films exhibit redox pairs labelled I/I′ and II/II′ centred at 56 mV/677 mV and 785 mV/1110 mV (vs Ag/AgCl). These peaks I/I′ are assigned to transitions between the polaron and bipolaron states of the polymer [142] as depicted by the schematic in Figure 29(b) while the peaks II/II′ are suspected to be the redox transitions between Au^{3+} and Au^0 [333] as it has been depicted earlier that Au got attached to the sulphur element of PProDOT during polymerization.

(b)

(c)
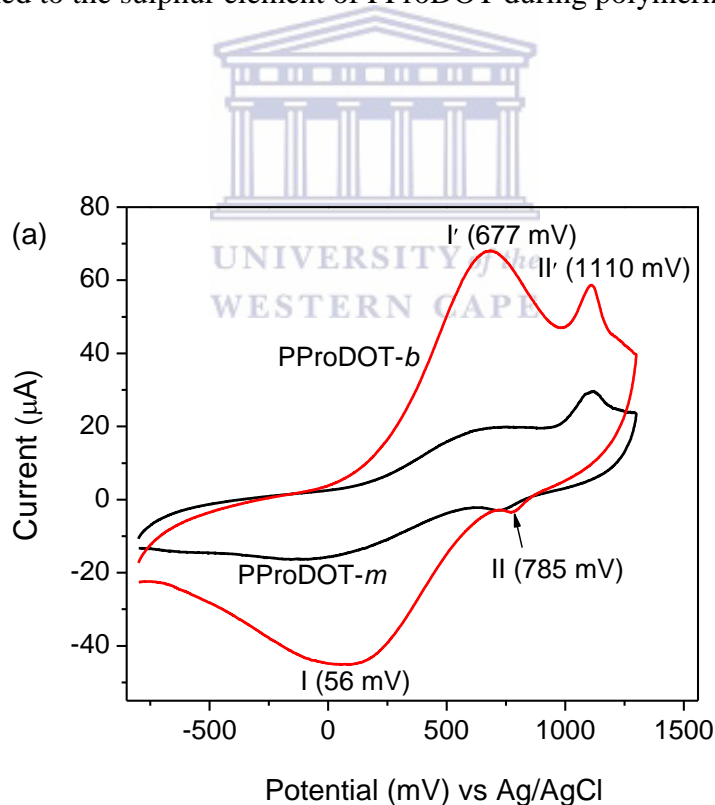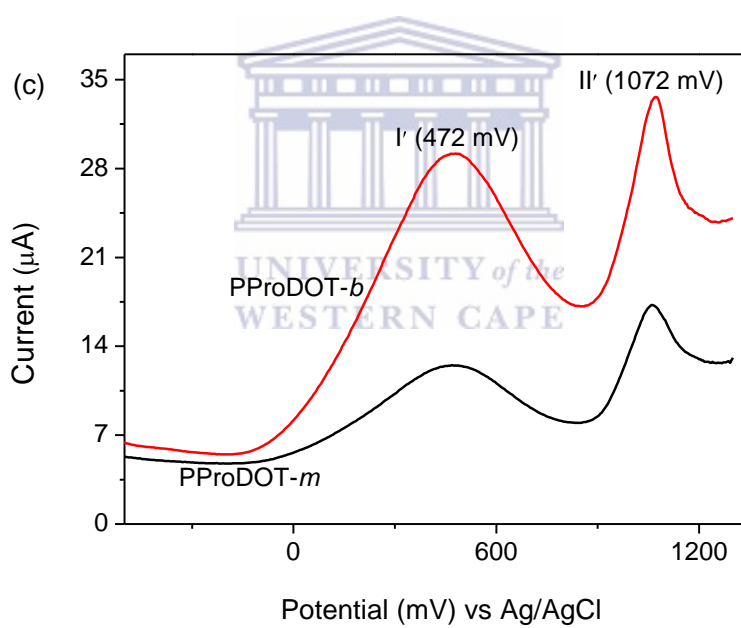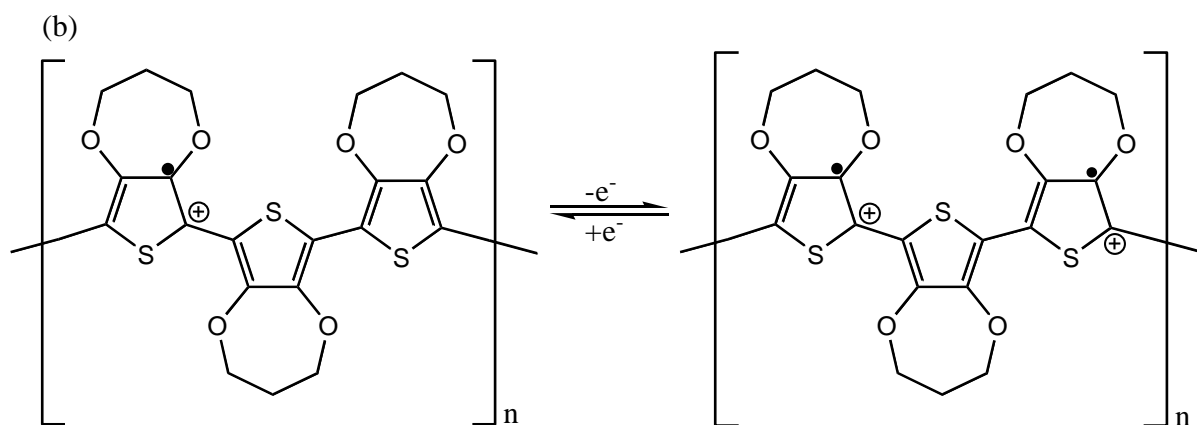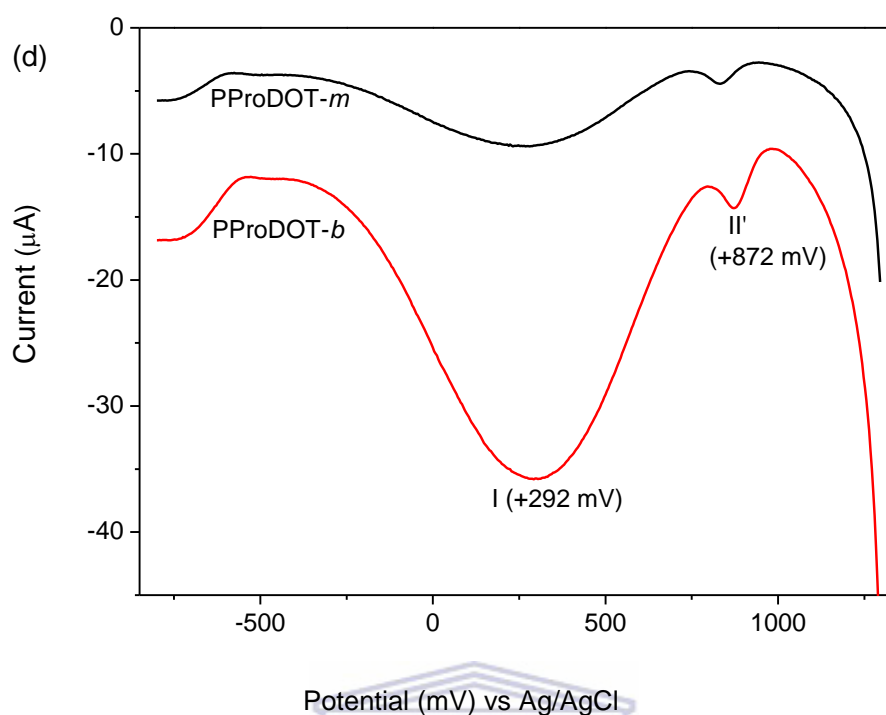
Figure 29: Electron transfer capability profiles for the PProDOT in 0.1 M LiClO4 at 30 mV/s investigated using (a) CV, (c) oxidative DPV and (d) reductive DPV. (b) shows the structural units giving rise to the polaronic transitions of the polymer.

The DPV graphs (Figure 29 (c) and (d)) confirm the observations revealed from the CV as two oxidation peaks (at 472 mV and 1072 mV) and two reduction peaks (at 292 mV and 872 mV) (vs Ag/AgCl) are evident. From both techniques, the PProDOT-*b* exhibits higher peak currents than the PProDOT-*m*. This behaviour may be associated with increased surface area the casting of another layer of the porous conducting nanopolymer which results in an increased amount of AuNPs, hence the observed increase in electrical conductivity [334]. Chronocoulometry was also used to investigate the amount of charge transported during the reduction-oxidation processes [335]. Again, the PProDOT-*b* shows a three-fold magnitude of

charge than the PProDOT-*m* (Figure 30). This further confirms that the casted monolayer was less efficient for charge transfer.
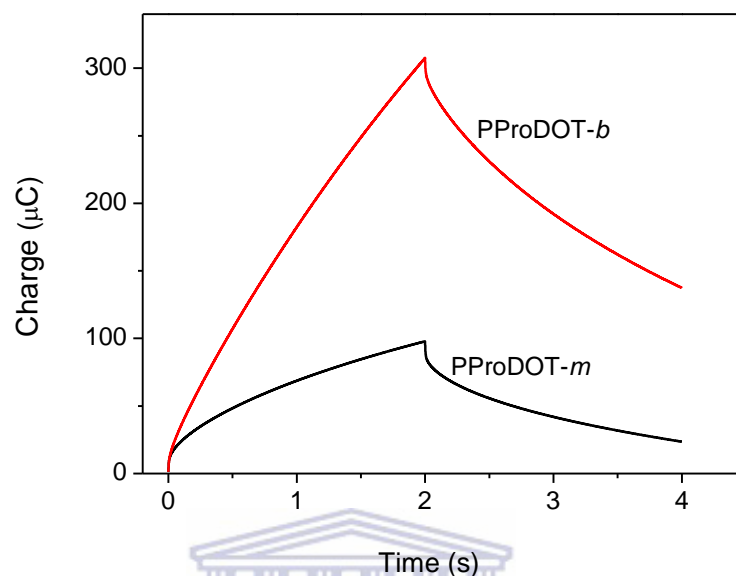

Figure 30: Chronocoulometric profiles of PProDOT-*m* and PProDOT-*b*. A thicker surface of PProDOT (PProDOT-*b*) reveals better charge storage efficiency than the thinner surface (PProDOT-*m*).

PProDOT is amongst the most potential applicants in electrochromic and energy storage devices. Hence, its energy storage capability was observed in 0.1 M LiClO$_4$ in which the redox processes are associated with lithium ion insertion and removal which, in turn, correspond to charge-discharge processes. Using chronocoulometry, an amount of charge induced by a potential step is plotted as a function of time. During these potential steps, the amount of charge passing at a certain time is related to bleaching and coloration processes or charge-discharge processes corresponding to ion intercalation and de-intercalation [336,337]. From the charge-time curves of both PProDOT-*m* and PProDOT-*b,* it can be observed that the discharging profile does not go to the starting point, implying that the PProDOT-b has not

undergone oxidation completely within the given time. The PProDOT-*b* also has a higher charge storage capacity than the PProDOT-*m*, depicted by the area under the curve corresponding to a 3-fold charge magnitude for the PProDOT-*b* as compared to the PProDOT-*m*. These results are in agreement with the CV and DPV observations.

3.2. Citrate-stabilized gold nanoparticles (AuNPs)

To observe the alterations brought by the incorporated AuNPs onto PProDOT, autographic absorbance properties and morphology of the AuNPs alone were investigated (Figure 31). The TEM micrograph shows spherical nanoparticles of diameters ranging between 15 nm and 20 nm. Nanoparticles in this diameter range are usually obtained from the citrate reduction method with small variations in size induced by the starting concentration of the gold salt, amount of reducing agent and the temperature at which the boiling colloidal solution is maintained [338,339]. The TEM image also reveals multiple lattice fringes corresponding to the interplanar lattice spacing of the (111) plane [340,341]. The AuNPs exhibit the characteristic surface plasmon absorbance band observed at 518 nm [342].

Amongst the size-dependent properties of AuNPs is the band gap whose magnitude determines the conductivity nature of the material categorized as conducting, semiconducting and non-conducting. Using the formula in equation 4.1, the AuNPs show an energy band gap of 2.4 eV which falls within the range for semiconducting material [342].

$$E = \frac{hc}{\lambda} \qquad\qquad Equation\ 4.1$$

In the above equation, E denotes the band gap, h is Plancks constant, c is the speed of light and λ is the wavelength.
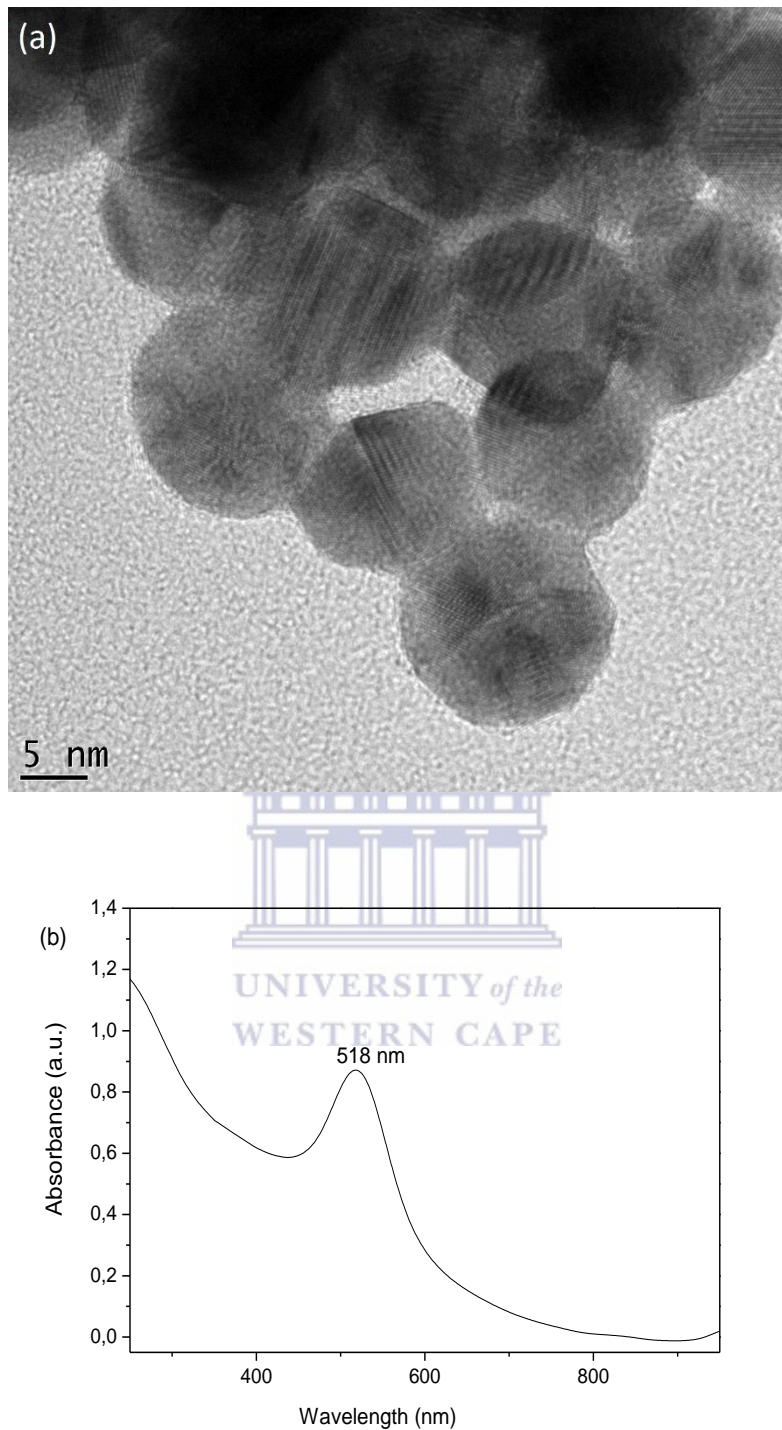
Figure 31: (a) TEM morphological view and (b) the autographic surface plasmon resonance absorption spectrum of the AuNPs respectively revealing spherical nanoparticles (of dimaeter ranging between 15 nm and 20 nm) absorbing energy at 518 nm.

3.3. The PProDOT-AuNP nanocomposite

3.3.1. Morphological view

The nanocomposite was achieved through a one-pot synthetic procedure exploiting the thiol-gold chemistry between the sulfur element of the PProDOT and the gold element of the AuNPs. The SEM image (Figure 32(a) shows a similar morphology to the PProDOT-RT sample by revealing closely-packed spherical particles of around 100 nm diameters. However, this film exhibits less agglomerated particles than the SDS-PProDOT and this may be attributed to the incorporated gold nanoparticles confining the growth of the polymer units [325].


124
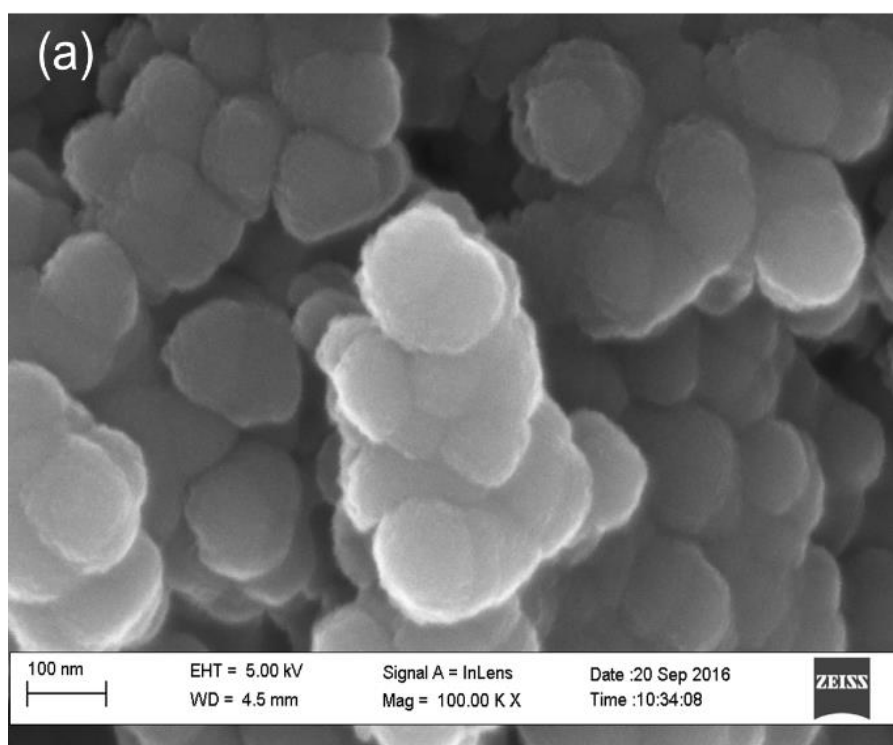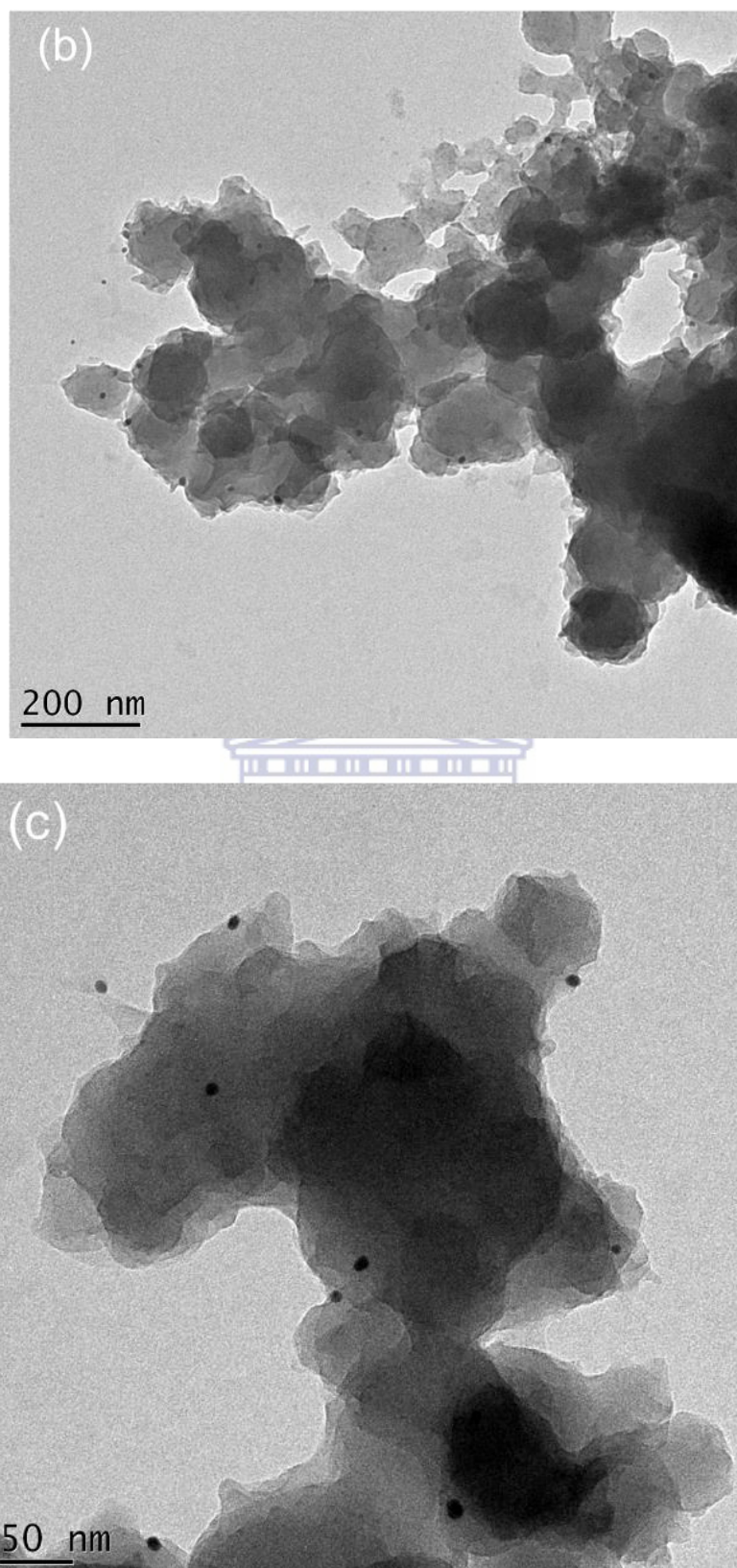
Figure 32: (a) SEM image of PProDOT-AuNPs reveals a spherical particles of approximately 100 nm. (b) and (c) TEM images of the PProDOT-AuNPs nanocomposite at different magnifications. AuNPs (small dark particles) are well distributed in the PProDOT network..

125

The TEM (Figure 32 (b) and (c)) shows the AuNPs attached to the PProDOT at both lower and higher magnifications. The back-scattered electrons micrograph also shows evenly distributed metal particles (Figure 33). At even higher magnification, the dots with diameters around 2.5 nm are still evident. The bigger particles of diameter around 10 nm are associated with the AuNPs, hence confirming their incorporation into the polymer.
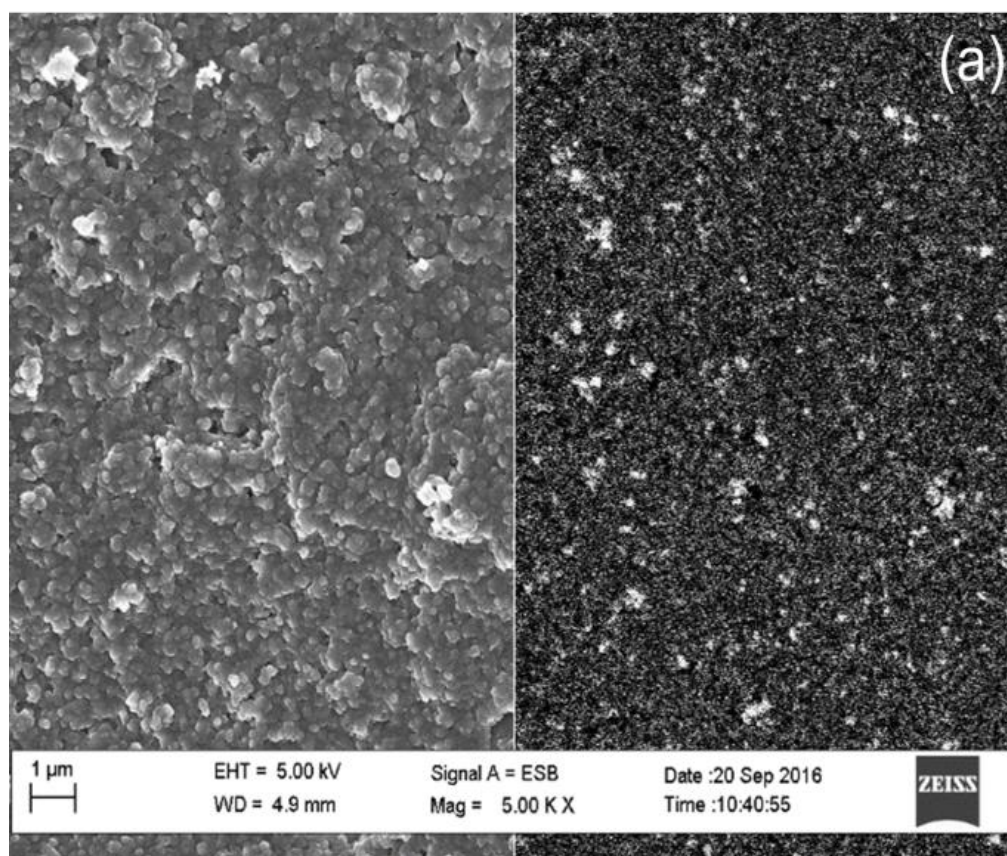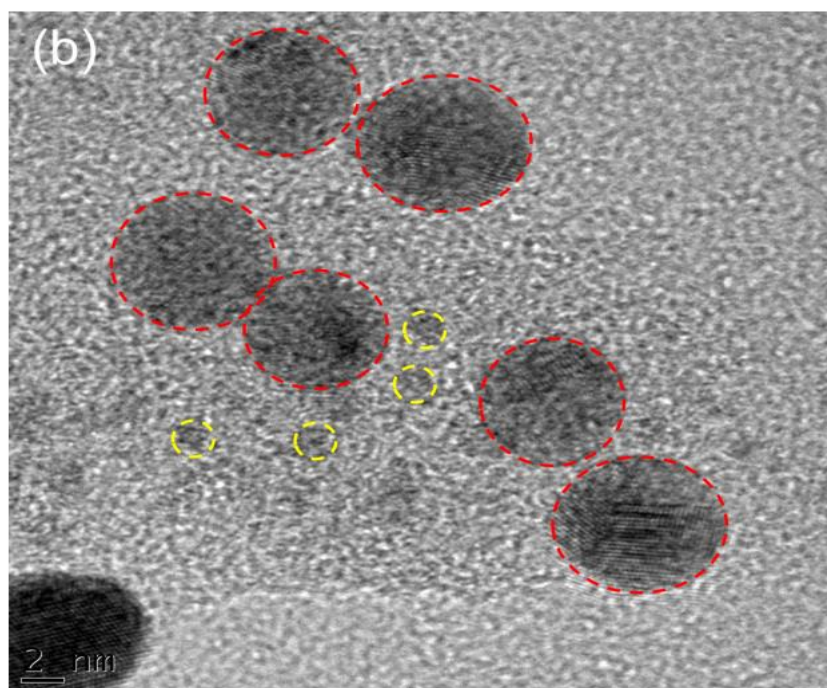
Figure 33: (a) Back scattered electron SEM image and (b) high magnification TEM image of the PProDOT-AuNPs nanocomposite showing the distribution of AuNPs within the PProDOT polymer matrix.
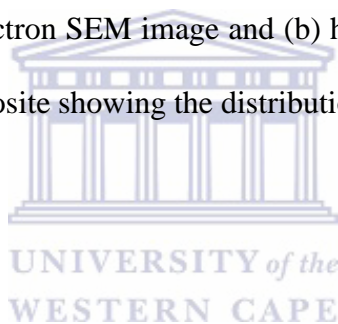
3.3.2. *Energy absorption properties of the nanocomposite*

The UV-Vis spectra of the PProDOT-AuNPs nanocomposite is shown in Figure 34. The spectrum shows absorbance maxima at different wavelengths. The peaks at 269 nm and 369 nm correspond to the autographic π-π* transitions induced by the C=C bonds of the benzenoid and quinoid units of conjugated polymers. Polaronic transitions are also evident at 476 nm. When compared to the SDS-PProDOT, these peaks are red-shifted to higher wavelengths while the free-carrier tail is blue-shifted to 769 nm and 830 nm. These shifts are evidence of interactions between PProDOT and the AuNPs in which the AuNPs incorporation increases and decreases conjugation lengths of the aromatic and benzenoid polymer units [343] The peak at 549 nm can be solely assigned to the surface plasmon absorption band of the AuNPs, further confirming their presence in the nanocomposite.
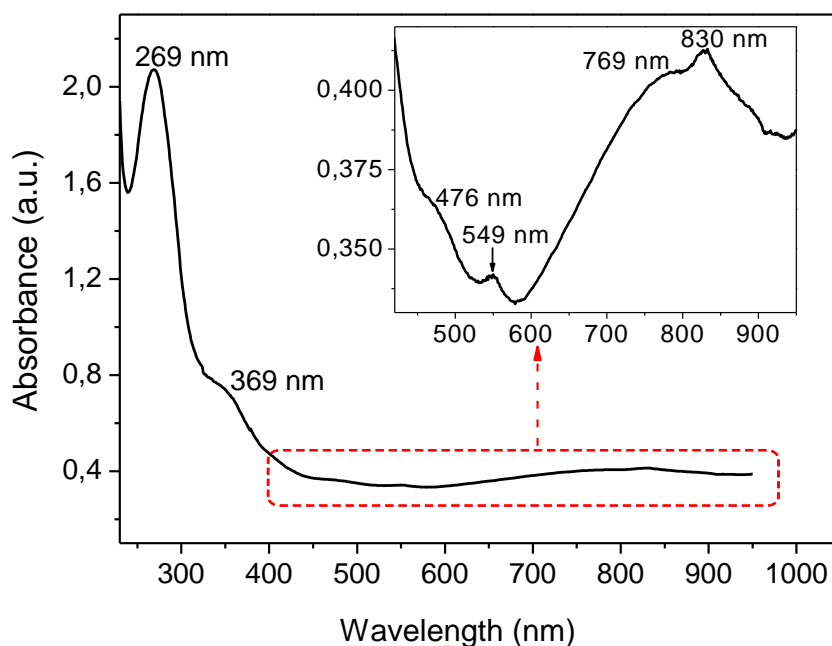
Figure 34: UV-Vis absorption spectrum revealing energy absorption by the PProDOT-AuNPs nanocomposite. The insert figure is a magnified view of the red-marked spectral range. AuNPs incorporation is confirmed by the absorption band at 549 nm.

3.3.3. Electron transfer and charge transport properties

The CV graph of the nanocomposite (Figure 35(a)) shows two redox pairs as was observed for the PProDOT. However, the oxidation peak (peak I´) attributed to the polaronic transitions of PProDOT shows quenched electroactivity into a broad peak around +500 mV (vs Ag/AgCl). This may be associated with the incorporated AuNPs masking the oxidation of PProDOT while their prominence is witnessed by the enhanced current peak for its oxidation (labelled peak II´) observed at +1090 mV (vs Ag/AgCl). Both reduction peaks show increased peak currents attributed to the increased surface area induced by incorporation of the AuNPs into the polymer

matrix [334]. The peaks are observed at +320 mV and +762 mV (vs Ag/AgCl) and are respectively assigned to reduction of the PProDOT polymer and Au.

http://etd.uwc.ac.za
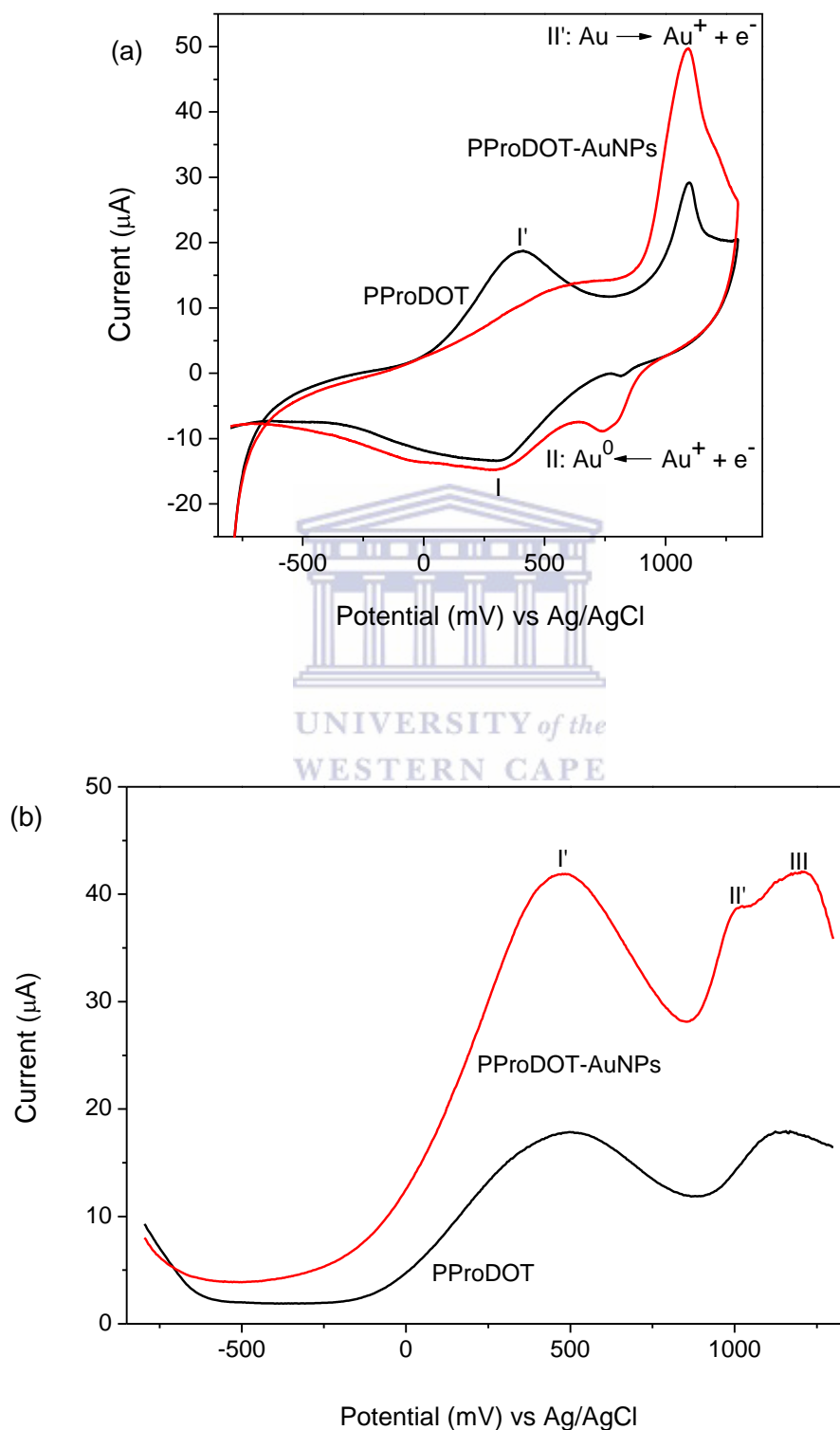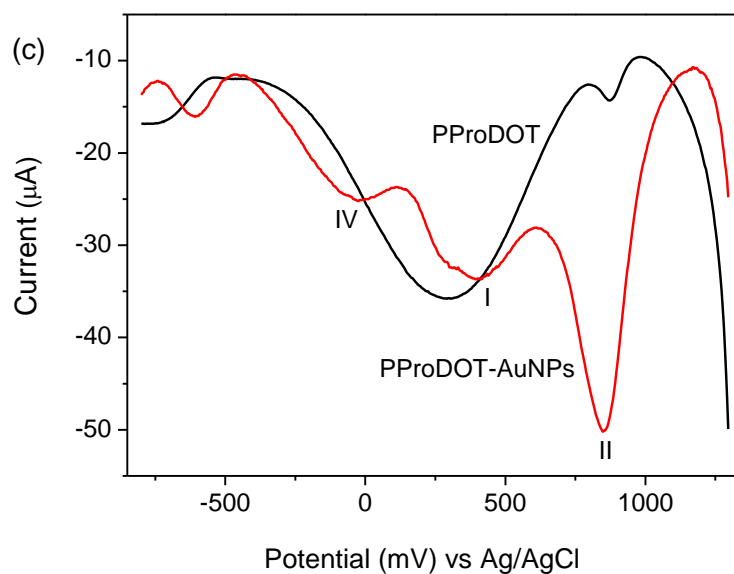
Figure 35: Electron transfer capability profiles of the PProDOT-AuNPs investigated using (a) CV, (b) oxidative DPV and (c) reductive DPV scans. Experiments were conducted in 0.1 M LiClO$_4$ at 30 mV/s.
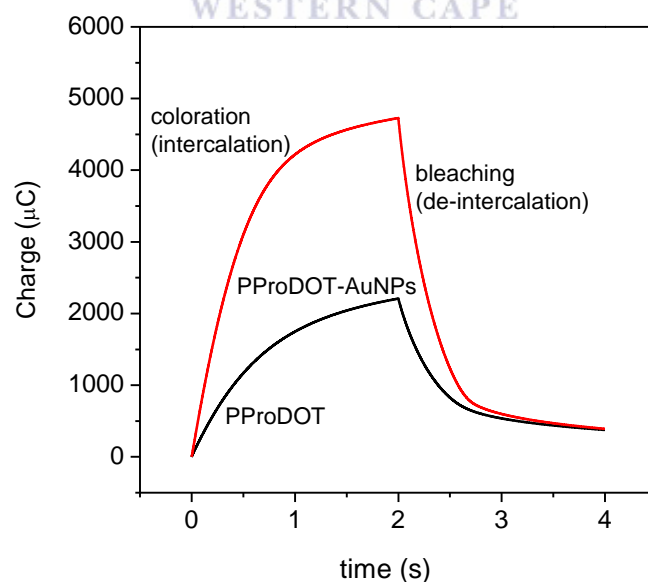

Figure 36: Charge-time chronocoulometric profile of the PProDOT-AuNPs nanocomposite revealing better charge storage capability (almost 5000 µC) than the PProDOT (2200 µC).

The DPV graphs (Figures 35(b) and (c)) show additional oxidation and reduction peaks when compared to the CV. Similarly to CV, the peak labelled III (+1142 mV vs Ag/AgCl) may be associated with further oxidation of the Au^{3+} to Au^0 [333,344]. Peak IV (-83 mV vs Ag/AgCl) may be attributed to the presence of oxygen moieties in the nanocomposite matrix which may be from the citrate molecule stabilizing the AuNPs enhancing the signal for the oxygen from the dioxypropyl molecule of PProDOT.

The nanocomposite also reveals symmetric chronocoulometric profile as shown in Figure 36. This profile shows a three-fold magnitude for the amount of charge transported during the ion intercalation and de-intercalation processes when compared to PProDOT. This increase in charge is ascribed to an increased charge induced by the incorporated AuNPs carrying a high negative charge on their surface [345,346]. Another important property displayed by this profile is the total symmetry of the forward and reverse scans whose ratio (Q_i/Q_d) equals one [347] (subscripts i and d denote intercalation and de-intercalation, respectively). This relationship explains better reversibility of the nanocomposite as the intercalation and de-intercalation processes occur at the same rate.

4. Conclusion

A highly electroconductive polymer based on the conducting polymer poly(3,4-propylenedioxythiophene) and gold nanoparticles has been prepared in the presence of sodium dodecyl sulphate acting as both a template and a surfactant. The templating ability of the SDS is evidenced by the nanospherical particles of PProDOT achieved in its presence when compared to the pod-shaped nanostructutes of the surfactant-free PProDOT.

The transmission electron microscopy studies confirm incorporation of the gold nanoparticles into the nanocomposite by showing the spherical nanoparticles of mean diameter around 10 nm. The synergistic effect of the incorporated gold nanoparticles is witnessed by the enhanced electrical conductivity of the nanocomposite depicted in its voltammetric profiles. In addition, the nanocomposite also shows potential for application in electrochromic and energy storage devices.

UNIVERSITY *of the*

WESTERN CAPE

5. References

309. Xu, X.-N., Guan, X.-N., Zhou, H.-H. & Zhu, Y.-F. One-Step Reduction and Surface Modification of Graphene Oxide by 3-Hydroxy-2-Naphthoic Acid Hydrazide and Its Polypropylene Nanocomposites. *Nanomaterials.* 7, 1-17 (2017).

310. Chen, Z., Krishnamachary, B. & Bhujwalla, Z. Degradable Dextran Nanopolymer as a Carrier for Choline Kinase (ChoK) siRNA Cancer Therapy. *Nanomaterials.* 6(2), 1-8 (2016).

311. Brostow, W., Lobland, H., Hnatchuk, N. & Perez, J. Improvement of Scratch and Wear Resistance of Polymers by Fillers Including Nanofillers. *Nanomaterials.* 7**,** 1-12 (2017).

312. Bramhill, J., Ross, S. & Ross, G. Bioactive nanocomposites for tissue repair and regeneration: A review. *Int. J. Environ. Res. Public Health* 14, 1-45(2017).

313. Müller, K., Bugnicourt, E., Latorre, M., Jorda, M., Echegoyen, S.Y., Lagaron, J.M., Miesbauer, O., Bianchin, A., Hankin, S., Bölz, U., Pérez, G., Jesdinszki, M., Lindner, M., Scheuerer, Z., Castelló, S. & Schmid, M. Review on the Processing and Properties of Polymer Nanocomposites and Nanocoatings and Their Applications in the Packaging, Automotive and Solar Energy Fields. *Nanomaterials* 7(4), 1-97 (2017).

314. Huh, D. S. & Basavaraja, C. Improving electron transport and mechanical properties of polyaniline-based composites. (2016), http://www.4spepro.org/pdf/006131/006131.pdf

315. Godeau, G., Darmanin, T. & Guittard, F. Superhydrophobic/highly oleophobic surfaces based on poly(3,4-propylenedioxythiophene) surface post-functionalization. *J. Polym. Res.* 23, (2016).

316. Jamal, R., Zhang, L., Wang, M., Zhao, Q. & Abdiryim, T. Synthesis of poly(3,4-propylenedioxythiophene)/MnO_2 composites and their applications in the adsorptive removal of methylene blue. *Prog. Nat. Sci. Mater. Int.* 26, 32–40 (2016).

317. Otley, M. T., Alamer, F.A., Zhu, Y., Singhaviranon, A., Zhang, X., Li, M., Kumar, A

& Sotzing, G.A. Acrylated Poly(3,4-propylenedioxythiophene) for Enhancement of Lifetime and Optical Properties for Single-Layer Electrochromic Devices. *ACS Appl. Mater. Interfaces.* 6(3), 1734–1739 (2014).

318.   Sezer, A.D. & Cevher, E. The Visible Light Activity of the TiO_2 and TiO_2 :V4 + Photocatalyst. IntechOpen (2012).

319.   Venditti, I., Fontana, L., Scaramuzzo, F.A., Russo, M.V., Battocchio, C., Carlini, L., Gonon, L., Mareau, V.H. & Fratoddi, I. Nanocomposite Based on Functionalized Gold Nanoparticles and Sulfonated Poly(ether ether ketone) Membranes: Synthesis and Characterization. *Materials..* 10, 1-14 (2017).

320.   Mendes, R., Fernandes, A.R. & Baptista, P.V. Gold Nanoparticle Approach to the Selective Delivery of Gene Silencing in Cancer—The Case for Combined Delivery? *Genes,* 8, 1-16 (2017).

321.   Kuzmanović, M., Delva, L., Cardon, L. & Ragaert, K. The effect of injection molding temperature on the morphology and mechanical properties of PP/PET blends and microfibrillar composites. *Polymers.* 8, 13–18 (2016).

322.   Shi, Y., Peng, L., Ding, Y., Zhao, Y. & Yu, G. Nanostructured conductive polymers for advanced energy storage. *Chem. Soc. Rev.* 44, 6684–6696 (2015).

323.   Li, Y. Organic Optoelectronic Materials. Springer (2015).

324.   Su, N. Improving Electrical Conductivity, Thermal Stability, and Solubility of Polyaniline-Polypyrrole Nanocomposite by Doping with Anionic Spherical Polyelectrolyte Brushes. *Nanoscale Res. Lett.* 10, 1-20 (2015).

325.   Mahalakshmi, B. & Vedhi, C. Synthesis and Characterization of Perfluorooctanoic Acid Anionic Surfactant Doped Nanosize Polyaniline. *Open J. Synth. Theory Appl.* 3, 57–68 (2014).

326.   Farell, T.P. Nanostructured Conducting Polymers for Applications in Water Treatment

and Aerospace Coatings. *Thesis*. (2013).

327.   Boeva, Z. A. & Sergeyev, V. G. Polyaniline: Synthesis, properties, and application. *Polym. Sci. Ser. C.* 56, 144–153 (2014).

328.   Abdiryim, T., Ali, A., Jamal, R., Osman, Y. & Zhang, Y. A facile solid-state heating method for preparation of poly(3,4-ethelenedioxythiophene)/ZnO nanocomposite and photocatalytic activity. *Nanoscale Res. Lett.* 9(1), 1-18 (2014).

329.   Vijayakumar, B., Anjana, K. O. & Rao, G. R. Polyaniline/clay nanocomposites: Preparation, characterization and electrochemical properties. *IOP Conf. Ser. Mater. Sci. Eng.* 73, 1-9 (2015).

330.   Shao, W., Jamal, R., Xu, F., Ubul, A. & Abdiryim, T. The effect of a small amount of water on the structure and electrochemical properties of solid-state synthesized polyaniline. *Materials (Basel).* 5, 1811–1825 (2012).

331.   Linganathan, P., Sundararajan, J. & Samuel, J. M. Synthesis, Characterization, and Photoconductivity Studies on Poly (2-chloroaniline) and Poly(2-chloroaniline)/CuO Nanocomposites. 2014, 1-10 (2014).

332.   Wang, J., Gong, J., Xiong, Y., Yang, J., Gao, Y., Liu, Y., Lu, X. & Tang, Z. Shape-dependent electrocatalytic activity of monodispersed gold nanocrystals toward glucose oxidation. *Chem. Commun.* 47, 6894–6896 (2011).

333.   Zhou, Y., Sharma, S. K., Peng, Z. & Leblanc, R. M. Polymers in carbon dots: A review. *Polymers (Basel).* 9(2), 1-20 (2017).

334.   Atta, N. F., Galal, A. & Ali, S. M. Determination of the diffusion coefficients for charge transfer through homo- , bilayered- and co-polymers of 3-methyl-. 7, 785–805 (2012).

335.   Kharade, R. R., Mali, S.S. Mohitem S.S., Kondalkar, V.V., Patil, P.S. & Bhosale, P.N. Hybrid Physicochemical Synthesis and Electrochromic Performance of WO_3/MoO_3 Thin Films. *Electroanalysis.* 26, 2388–2397 (2014).

336.   Usha, K. S., Sivakumar, R., Sanjeeviraja, C., Sathe, V., Ganesand, V. & Wange, T.Y. Improved electrochromic performance of a radio frequency magnetron sputtered NiO thin film with high optical switching speed. *RSC Adv.* 6, 79668–79680 (2016).

337.   Verma, H. N., Singh, P. & Chavan, R. M. Gold nanoparticle: Synthesis and characterization. *Vet. World.* 7, 72–77 (2014).

338.   Ahmad, T. & Khan, W. Size Variation of Gold Nanoparticles Synthesized Using Tannic Acid in Response to Higher Chloroauric Acid Concentrations. *World J. Nano Sci. Eng.* 3, 62–68 (2013).

339.   Suvarna, S., Das, U., Sunil, K.C., Mishra,S., Sudarshan, M., Saha, K.D., Dey, S., Chakraborty, A. & Narayana, Y. Synthesis of a novel glucose capped gold nanoparticle as a better theranostic candidate. 12(6), 1–15 (2017).

340.   Bhattarai, N., Khanal, S., Pudasaini, P. R., Pahl, S., & Romero-Urbina, D. Citrate Stabilized Silver Nanoparticles : Study of Crystallography and Surface Properties Citrate Stabilized Silver Nanoparticles : Study of Crystallography and. 3(3) 15-28 (2011).

341.   Kiran, K. MSA-capped gold nanoparticle-supported alumina for the determination of Pb and Cd in various environmental water samples. *Appl. Nanosci.* 5, 795–800 (2015).

342.   Sprick, R. S., Bonillo, B., Sachs, M., Clowes, R., Durrant, J.R., Adams, D.J. & Cooper, A.I. Extended conjugated microporous polymers for photocatalytic hydrogen evolution from water. *Chem. Commun.* 52, 10008–10011 (2016).

343.   Rodriguez, P., Kwon, Y. & Koper, M. T. M. The promoting effect of adsorbed carbon monoxide on the oxidation of alcohols on a gold catalyst. *Nat Chem.* 4, 177–182 (2012).

344.   Miao, P., Han, K. & Tang, Y. Electrochemical detection of aqueous Ag^+ based on Ag^+-assisted ligation reaction. *Sci. Rep.* 5, 1-11 (2015).

345.   Tortello, M., Sola, A., Sharda, K., Paolucci, F., Nair, J.R., Gerbaldi, C., Daghero, D. & Gonnelli, R.S. Huge field-effect surface charge injection and conductance modulation in

metallic thin films by electrochemical gating. *Appl. Surf. Sci.* 269, 17–22 (2013).

346.   Orellana, M., Arriola, P., Del Rio, R., Schrebler, R., Cordova, R., Scholz, F. & Kahlert, H. Chronocoulometric study of the electrochemistry of Prussian blue. *J. Phys. Chem. B* 109, 15483–15488 (2005).

347.   Jayalakshmi, M . & Gomathi, H. Electrochemical behaviour of prussian blue deposits in presence of some non-aqueous background solutions. Bulletin Electrochem. 16(3), 123-129 (2000).

UNIVERSITY *of the*

WESTERN CAPE

Chapter 5

Electrochemical Poly(3,4-propylenedioxythiophene) DNA Aptamer Biosensor for Signalling Interferon Gamma (IFN-ɣ) TB Biomarker

ABSTRACT

It is worth noting the incredible commitment of the world, united through the World Health Organization, towards eradicating tuberculosis (TB). However, this disease persists as a burden whose early diagnosis is very crucial as early treatment initiation can combat its morbidity and, hence resulting in a reduction of its negative impact. This study reports on a novel aptameric biosensor system developed towards early TB diagnosis by electrochemically signalling its biomarker, interferon gamma (IFN-γ). The sensing platform is a ternary system exploiting the gold-thiol surface chemistry towards a stable covalently bonded system achieved by immobilising a thiolated anti- IFN-γ DNA aptamer onto a nanocomposite platform comprising poly(3,4-propylenedioxythiophene) (PProDOT) and gold nanoparticles (AuNPs). The nanocomposite showed high electrical conductivity which was not lost after binding of the aptamer, thereby exhibiting potential as electron shuttles to signal the aptamer- IFN-γ binding. The biosensor showed admirable sensitivity during IFN-γ detection in pleural fluid samples with a mean detection limit of 2.2 pg/mL. This detection limit, alongside its linear range from 0.6 pg/mL to 2.2 pg/mL falls below the current cut-off limit of 15 pg/mL hence highlighting feasibility of the aptasensor system for signalling IFN-γ in clinical samples.

KEYWORDS: electrochemical impedance spectroscopy, interferon gamma, tuberculosis, detection limit, aptamer

1. Introduction

Tuberculosis is a highly infectious disease whose severity is aggravated by co-infections with other pathogens, communicable and non-communicable diseases including diabetes mellitus and human immunodeficiency virus (HIV) [27,105,348]. Although the disease and its infection (latent TB infection shortened as LTBI) can be prevented and cured, low sensitivities of current diagnostic methods which delay early TB diagnosis also delay treatment initiation [349], giving the disease bacteria a chance to replicate while gene mutations cause development of antibiotic-resistant strains [12,24]. Other factors that influence LTBI progression to the active TB disease include dietary deficiency, weakened immune systems due to medications or infections with other pathogens, the deceitful behaviour of the bacteria by residing in the human system for a long time until immunological response presents [30,350–352]. As a result, the disease kills an estimated 1.7 million individuals per year.

According to the latest World Health Organization (WHO) global TB report, South Africa is among the high burden countries (HBCs) adapting the name from their worst TB related cases [353]. With specific reference to South Africa, such cases may be associated with the high treatment default rate and crowded living spaces, especially prisons which hold large populations in which individuals are in confined frequent exposure to active-TB individuals thereby increasing their probability of acquiring LTBI infection [102,103,354,355].

The world has shown incredible devotion towards eradicating the TB epidemic by endorsing the advanced diagnostic methods with superior performance than the conventional sputum smear microscopy and tuberculin skin test. These techniques include the interferon gamma release assays (IGRAs) and the GeneXpert MTB/RIF, the MTBDRplus and the Line Probe Assay which also detect organism resistance to rifampicin and isoniazid therapy drugs. However, each of these assays has a limitation associated with it. Their combined limitations can be summarized as the inability to discriminate LTBI from active, post-BCG and non-

139

tuberculous organism interference and inability to discriminate viable from non-viable bacteria hinging on other techniques [16–19]. Moreover , it has been reported that the performance of these techniques is affected by T cell counts which are low in immune-suppressed individuals and over-expressed in BCG-vaccinated individuals [55,71,72]. Therefore, highly sensitive techniques for early TB diagnosis are still on demand.

Electrochemical nanobiosensors are amongst the most advanced techniques which display potential as point-of-care devices to address the limitations of conventional techniques mentioned earlier. Electrochemical nanobiosensors are also characterized by fast response times, portability and easy operation [359], giving them promising characteristics as first-generation devices that would be able to perform diagnostic and treatment-monitoring outputs. Electrochemical biosensors have been shown to lose sensitivity in the presence of analytes in real matrices [360] hence, current research on electrochemical nanobiosensors is devoted to addressing the limitations associated with their sensitivity.

Different strategies include use of analyte-specific molecules such as aptamers and use of signal amplifiers. Aptamers are artificial single-stranded (*ss*) deoxyribonucleic acid (DNA) or ribonucleic acid (RNA) molecules that are selected *in vitro* against specific targets (that can be any molecule including oligosaccharides, peptides, proteins and cells) using the Systematic Evolution of Ligands by Exponential (SELEX) enrichment process [361]. The technique is easily accessible, easy to operate and most importantly, allows modification and labelling of the aptamers with different materials at precise site-specific positions for different applications, based on the high affinity and specificity binding in the presence of their targets [362]. Aptamers are characterized by high thermostability, low or no immunogenicity and reversible denaturation resistance [117] and have considerable applications as biosensor, diagnostic and therapeutic agents [361,363]. Amongst the variety of targets, aptamers have been selected against pathogens and disease biomarkers including hepatitis (hepatitis C virus (HCV)), TB (interferon

gamma (IFN-γ) and 10-kDa culture filtrate protein (CFP-10)), HIV (HIV glycoprotein 120 (HIV gp120)) and Burkitt lymphoma (Ramos cells) [113–117].

This study saw need to develop an aptasensor system for early detection of TB based on signalling of its biomarker, interferon gamma (IFN-γ). IFN-γ is a cytokine expressed as immunological response to TB infection and its levels are associated with the level of TB infection. The current cut-off limit for positive TB infection is 15 pg/mL IFN-γ. In biosensors, the use of biomarkers is believed to automatically avoid false results induced by interference while aptamers minimize non-specific binding. To improve sensitivity a highly electroconductive nanocomposite of poly(3,4-propylenedioxythiophene) (PProDOT) and gold nanoparticles was used as both a charge transfer mediator and a receiving matrix for the aptamer. The system proposed here is a next-generation point-of-care device hoped to rapidly identify TB infection allowing early initiation of treatment and protection measures. Due to the easy handling, room temperature operation and fast response of electrochemical aptasensors, this system would practically benefit all end-users (medical practitioners and the society).

2. Experimental section

2.1. Reagents

Pleural fluid and an IFN-γ binding aptamer, modified with a 5ThiolMCS-D group was supplied by the by the Lung Infection and Immunity Unit (University of Cape Town). The aptamer sequence was 5′-CGG CGA AGG CAC GTG TGG GGT GGT CGC GT-3. All other reagents were purchased from Sigma Aldrich (South Africa) and used without further purification: 6-mercapto-1-hexanol (MCH), 3,4-propylenedioxythiophene (ProDOT), sodium dodecyl sulfate (SDS), acetonitrile (ACN), gold(III) chloride and sodium citrate trihydrate. A 0.1 M phosphate buffer solution (adjusted to pH 7.4 and used through the study) was prepared from Na$_2$HPO$_4$·2H$_2$O and Na$_2$HPO$_4$·2H$_2$O.

2.2. Morphological characterization of the nanocomposite

The morphology of the PProDOT-AuNPs nanocomposite was investigated using a Tecnai G2 F20X-Twin MAT high resolution transmission electron microscope (HR-TEM) at an acceleration voltage of 200 kV. For clear observations, morphologies of the PProDOT without AuNPs were also investigated.

2.3. Electrochemical measurements

Electrochemical measurements were performed using a CHI 760E electrochemical workstation and a conventional three-electrode system with a glassy carbon working electrode (GCE; surface area = 0.071 cm^2), Ag/AgCl (3 M NaCl) reference electrode and a platinum wire counter electrode. Prior to use, the working electrode was pre-conditioned by polishing in micro-alumina slurries of 1.0 µm, 0.3 µm and 0.05µm, followed by ultrasonication for five minutes in ethanol and water, respectively. All experiments were conducted in 6-ml electrolyte solutions.

Cyclic voltammograms (CV) were acquired within the potential limits between -800 mV and +1300 mV (vs Ag/AgCl) at 30 mV/s and a sensitivity of 1 mA/mV. The CV was the first technique used to monitor the aptasensor fabrication steps and was complemented with electrochemical impedance spectroscopy (EIS). The EIS measurements were acquired at a frequency range between 1 Hz - 100 kHz.

2.4. Synthesis and fabrication of the nanocomposite

The nanocomposite comprising poly(3,4-propylenedioxythiophene) (PProDOT) and gold nanoparticles (which will be denoted as PProDOT-AuNPs) was synthesized chemically from a monomer solution containing 0.04 M ProDOT and AuNPs in acetonitrile (1:0.5 v/v). After allowing an adsorption time of 1 h facilitated by ultrasonic radiation, a 15 mM auric chloride solution was introduced. The polymer nanocomposite was collected as a greenish blue powder

which was made into a paste using acetonitrile. Two layers of 3 uL PProDOT-AuNPs nanocomposite paste were drop casted onto glassy carbon electrodes.

2.5. Aptasensor fabrication and application

The aptasensor was fabricated onto the PProDOT-AuNPs nanocomposite based on exploitation of the gold-thiol chemistry between the three components. Before immobilization, the 5µ M aptamer solution was heated at 90 ºC for 2 minutes. Then, 5 uL of the aptamer solution were dropped onto the nanocomposite-modified electron and left to react for 4 h. Unbound aptamer was removed by carefully rinsing the electrode in phosphate buffer solution (pH 7.4). This aptasensing platform will be denoted as PProDOT-AuNPs-Apt. To avoid non-specific adsorption, mercapto-1-hexanolphosphate (MCH ~ 5 µM) was used as a blocking agent. The resulting aptasensing platform will be denoted as PProDOT-AuNPs-Apt-MCH. For detection of IFN-γ in real samples, pleural fluid was diluted to a working stock solution of 25 ng/mL in the buffer solution.
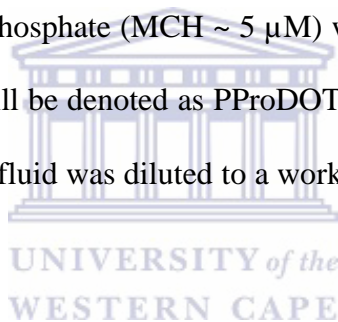
3. Results and discussion

3.1. Morphological view of the hosting nanocomposite

The morphology of the nanocomposite was investigated using transmission electron microscopy (TEM) (Figure 37). The TEM image reveals a morphology resembling that of its components in which the irregular sponge-like morphology is ascribed to the PProDOT [183] while the small nanospheres confirm the presence of AuNPs [338] that are evenly distributed and attached to the polymer.
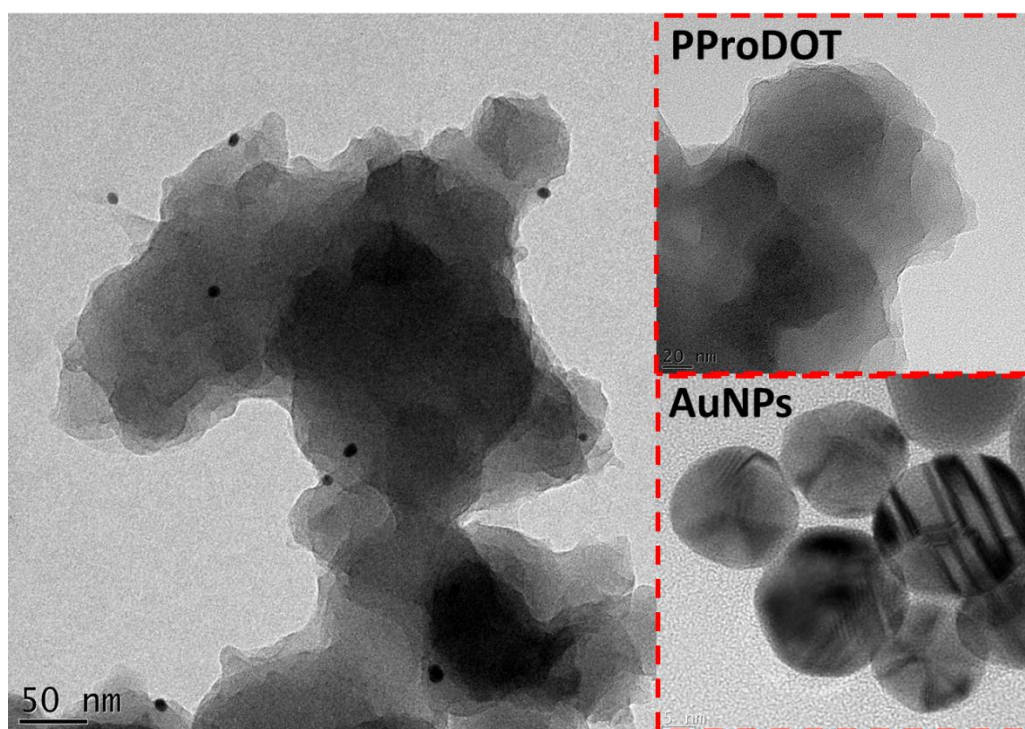
Figure 37: TEM image revealing the attachment of AuNPs onto the PProDOT polymer. Insert graphs show morphologies of PProDOT and AuNPs individually.
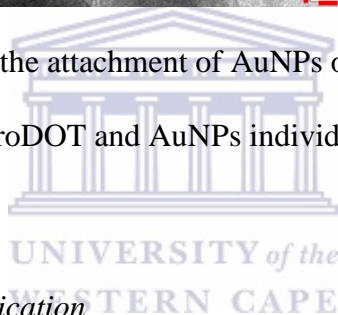
3.2. Stepwise aptasensor fabrication

The aptasensing platform presented here is a ternary system exploiting the gold-thiol chemistry between the sulfur elements of PProDOT and the aptamer and the gold element of the AuNPs. The first step was CV and EIS characterization to investigate how the aptamer affected the behaviour of the nanocomposite. From the CV graph (Figure 38), the nanocomposite shows a well-resolved redox pair at 100 mV/370 mV which is associated with transitions between polaron and polaron states of PProDOT while the broad peak at 1100 mV comes from oxidation of Au^{3+} to Au^0 [142,333]. For comparison, the CV profile of PProDOT is shown and has suppressed peak currents, confirming the incorporation of the AuNPs into PProDOT. However, a drop in peak current is observed after binding of the aptamer to the PProDOT-AuNPs. This

is accompanied by appearance of a new peak which may be assigned to reduction of the thiol

group used as a label in the aptamer.
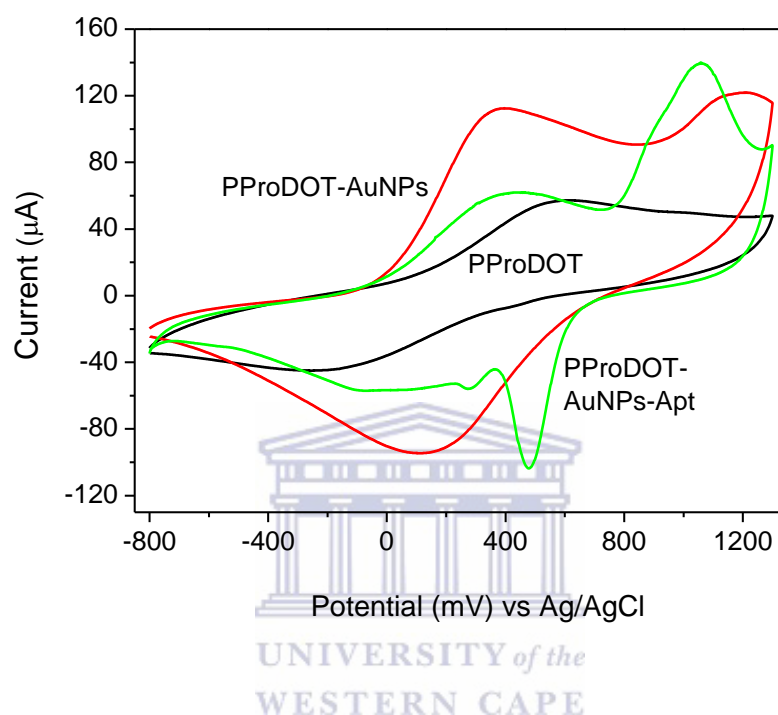
Figure 38: CV graph investigating the effect of aptamer binding on electroactivity of the

PProDOT-AuNPs nanocomposite at 30 mV/s. PProDOT shows a redox pair for its oxidized

and reduced state with a 40 µA current response. AuNPs enhanced the electroconductivity with

a current response of 100 µA accompanied by a new oxidation peak related to its oxidation.

After incubation with the thiol-modified aptamer, new peaks assigned to reduction of its

modifying group are observed while an enhancement in the oxidation/reduction of Au is also

noticed.
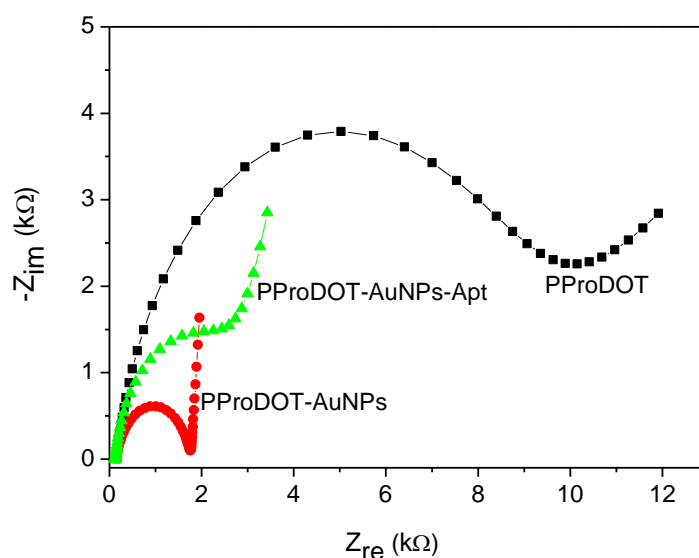
Figure 39: EIS Nyquist plots depicting charge transfer changes throughout the fabrication step. PProDOT (Rct = 8.4 kΩ) was conjugated with AuNPs, yielding the binary PProDOT-AuNPs nanocomposite (Rct = 1.6 kΩ). The thiolated aptamer was immobilized onto PProDOT-AuNPs, yielding the ternary system (3.1 kΩ).

EIS measurements were also conducted to supplement the information collected from the CV. From the Nyquist plot (Figure 39), all films exhibit semicircles associated with charge transfer and the linear parts denoting diffusion processes [364]. PProDOT displays a high charge transfer impeding behaviour with a charge transfer resistance (R_{ct}) value of 8.4 kΩ. The incorporation of AuNPs dramatically increased the electroconductivity of the PProDOT, leading a faster charge-transfer process with a smaller R_{ct} value of 1.6 kΩ. However, after aptamer binding, the R_{ct} value increases 3.1 kΩ and this is associated with a slow electron transfer resulting from the nonconductive protein and, hence, this confirms its immobilization [282].
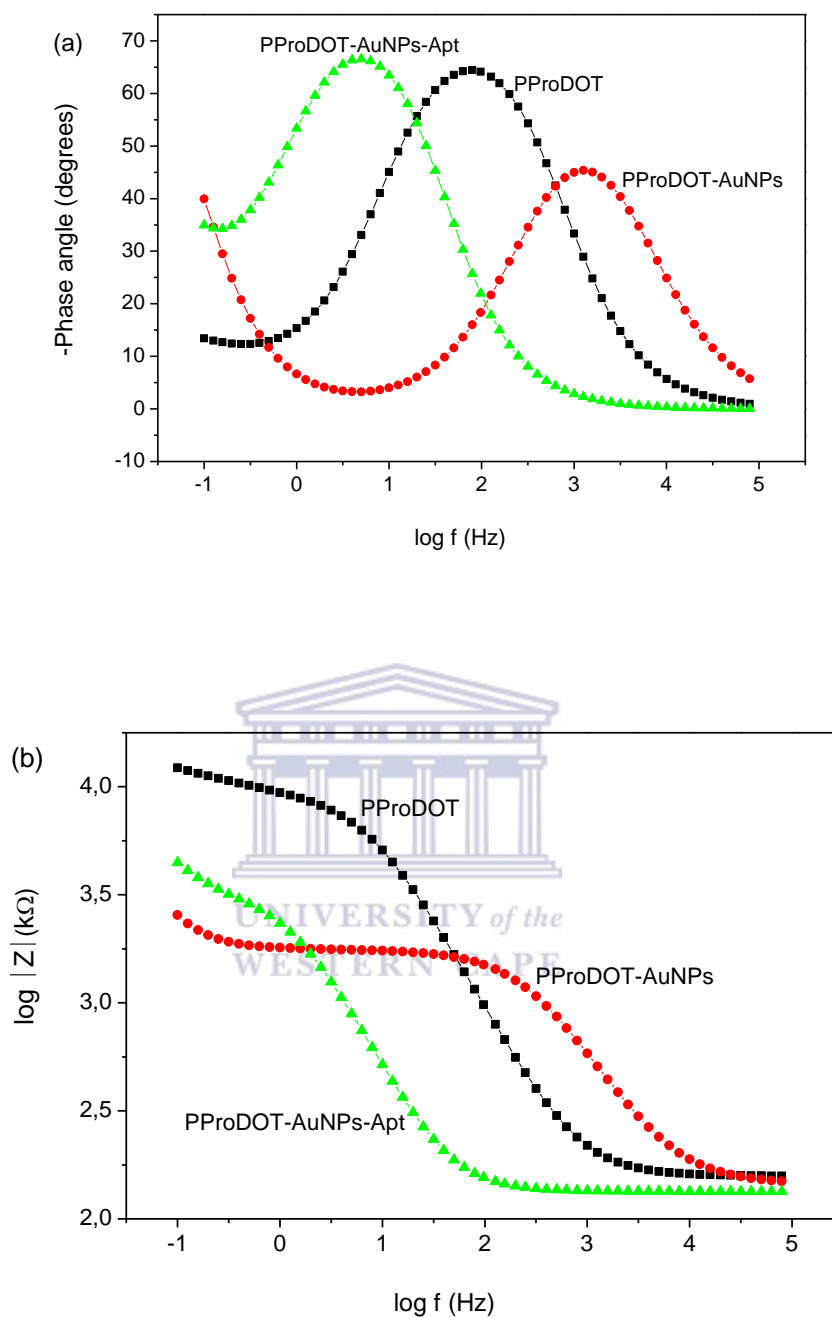
Figure 40: EIS Bode plot results for the fabrication process of the aptasensor. Plotted as a function of frequency, (a) phase angle and (b) impedance changes for PProDOT, PProDOT-AuNPs and PProDOT-AuNPs-Apt were monitored.

The typical bode plots for the films are shown in Figure 40. and are in agreement with the results obtained from the Nyquist plot. PProDOT displays a phase angle of 65º at 100 Hz and an impedance magnitude of 4.1 kΩ. The enhancing effect of the AuNPs is witnessed by the lower impedance of the PProDOT-AuNPs nanocomposite (3.4 kΩ) and a phase angle shift to 45 º suggesting its high conductivity at a higher frequency of 1585 Hz. This also confirms that the incorporated AuNPs facilitate charge transfer properties of the PProDOT which in turn can resist induced chemical changes [365]. As expected, the PProDOT-AuNPs-Apt exhibit a higher impedance (3.7 kΩ) and a phase angle shift to 67º at a low frequency (5 Hz). These changes are induced by the bound aptamer which hinders the charge transport [366].

3.3. Feasibility of the PProDOT-AuNPs –Apt towards IFN-γ detection

The electrochemical behaviour of the sensing platform, PProDOT-AuNPs-Apt was evaluated in the presence of IFN-γ to investigate its feasibility towards detection of the biomarker (Figure 41). The CV graph shows an increase in the peak currents except for the peak associated with reduction of Au^+ at +500 mV (vs Ag/AgCl). To account for the increase in peak current, it is assumed that aptamer-IFN-γ interactions induce conformational changes orientated in a manner that does not interfere with the electron transfer efficiency of the nanocomposite. The decrease in in the reduction peak of Au^+ mat be associated with blocked electron transfer induced by aptamer-analyte affinity binding interactions which occur after addition of IFN-γ. These observations are confirmed by the EIS Nyquist plot which reveals a higher charge transfer resistance indicated by the increase in the semicircle diameter. In absence of the analyte, the PProDOT-AuNPs-Apt shows a phase angle of 62 º at a frequency of 7 Hz. Bode plots show that presence of the analyte hinders charge transfer inducing shifts to a higher impedance, a higher phase angle (66 º) at lower frequency of 5 Hz. These results imply recognition of the analyte and its binding to the aptamer [367].

http://etd.uwc.ac.za
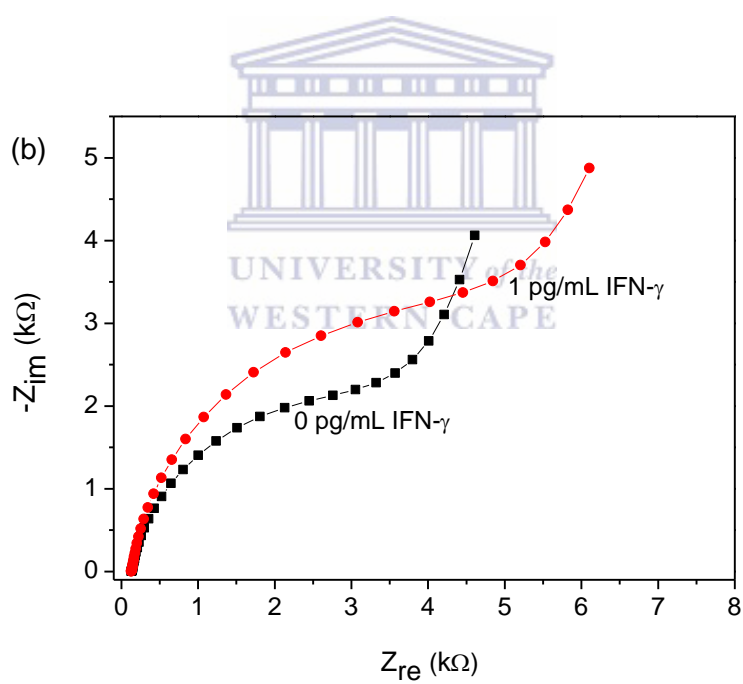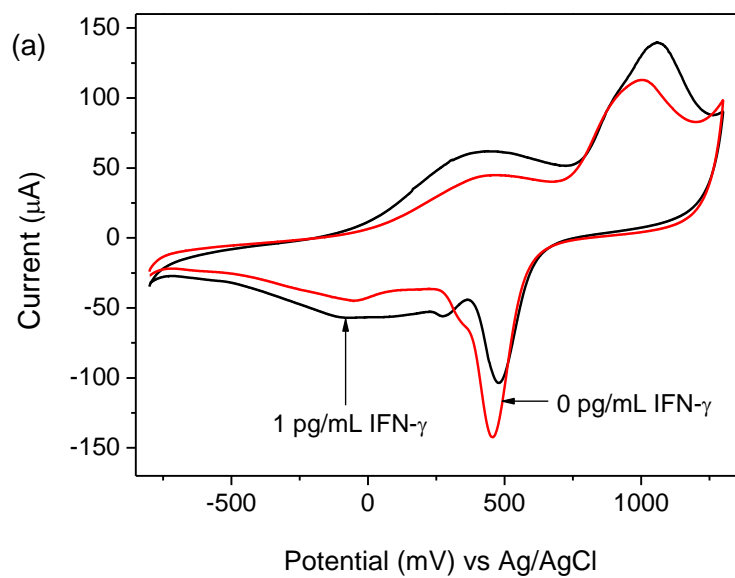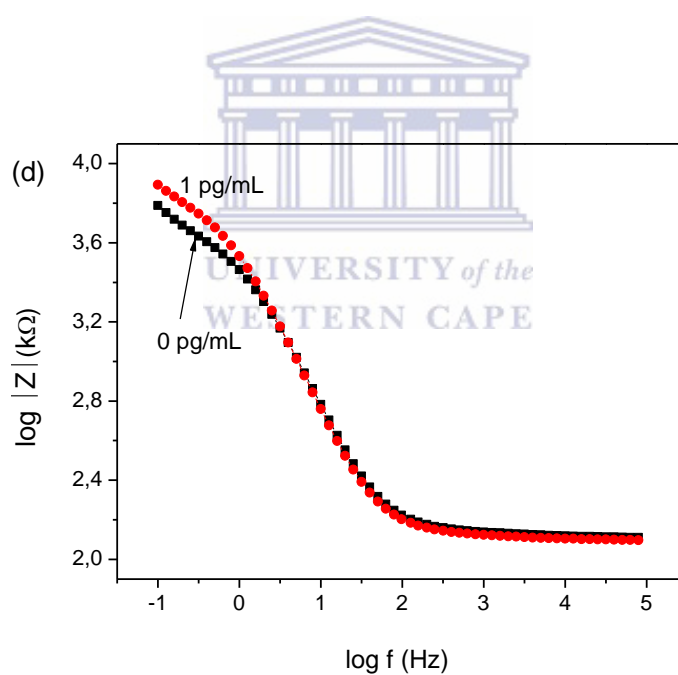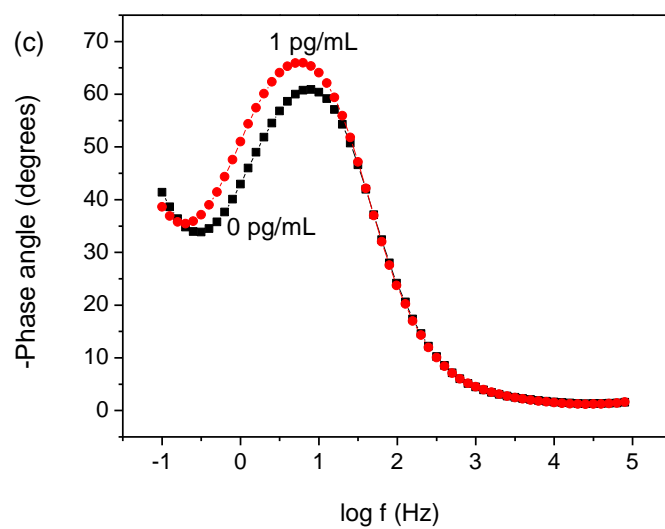
Figure 41: (a) CV and (b-d) EIS profiles revealing feasibility of the PProDOT-AuNPs-Apt platform towards IFN-γ detection.

3.4. Blocking agent effect

According to literature, blocking the remaining sites of the platform hosting the biomolecule is necessary to avoid defects in the recognition layer and, among the potential agents, 6-mercapto-1-hexanol (MCH) is widely used due to its ability to penetrate the biomolecule and reach exposed reactive groups on the hosting platform [368,369]. So, CV and EIS were further used to investigate the effect of MCH (Figure 42). A higher peak current is observed for the MCH-blocked platform using the CV and this result is complemented by the Nyquist and Bode plots which show better resistance of the platform to impedance changes, slightly faster charge transfer efficiency and lower charge transfer resistance than the PProDOT-AuNPs-Apt platform. Hence, the PProDOT-AuNPs-Apt-MCH sensing platform was used in all experiments in the following sections.

http://etd.uwc.ac.za

http://etd.uwc.ac.za
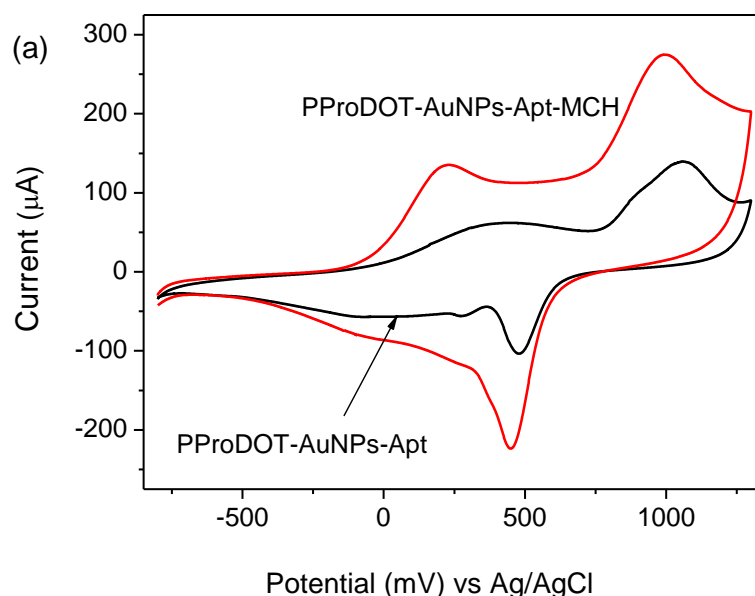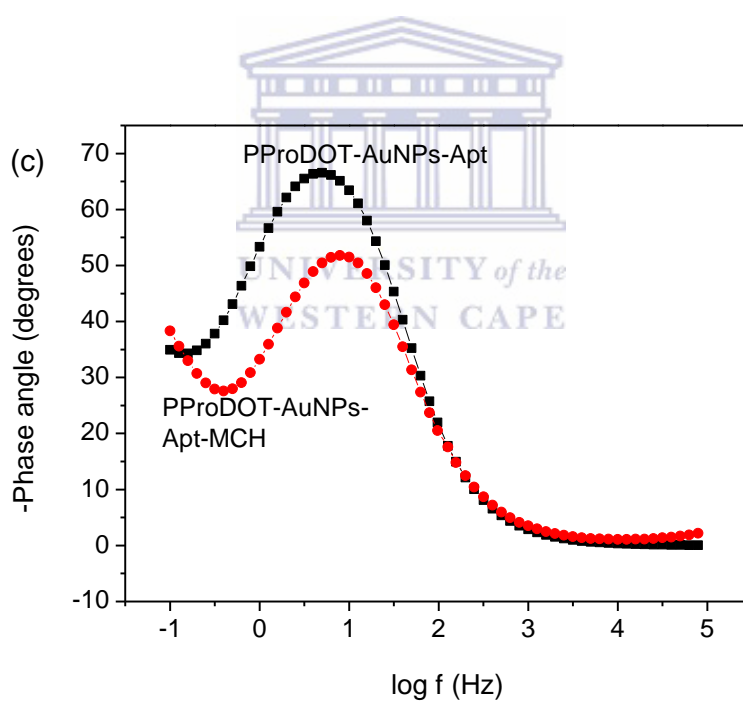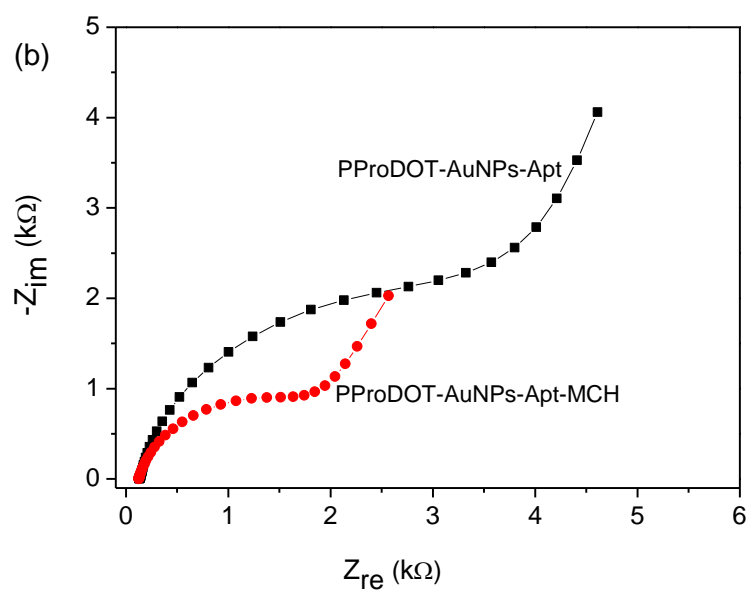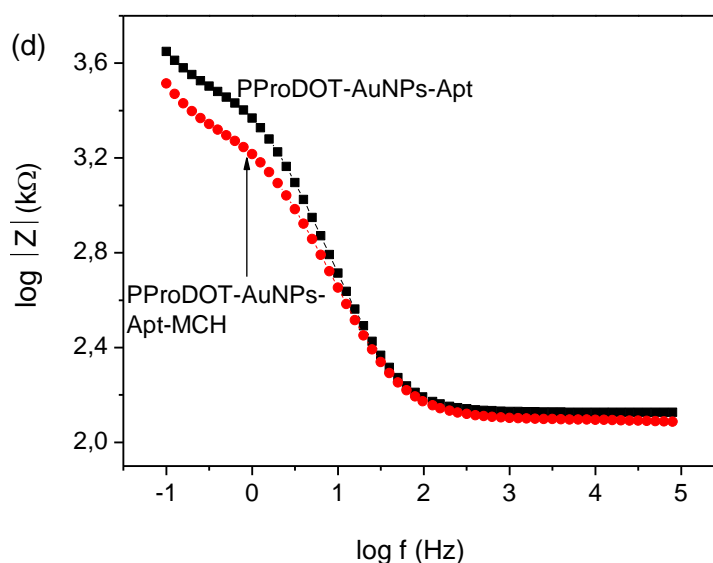
Figure 42: EIS experiments investigating the effect of blocking unreactive sites to minimize non-specific adsorptions. After blocking, the sensing platform shows improved charge transfer resistance and impedance properties.
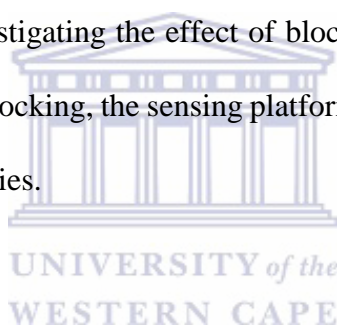
The feasibility of this sensing platform was evaluated in the presence of 1 pg/mL of IFN-γ using EIS (Figure 43). The performance of this platform was compared with that of the PProDOT-AuNPs-Apt. From the Nyquist plot, the PProDOT-AuNPs-Apt-MCH shows a lower charge transfer resistance than its counterpart suggesting that this platform has a potential to maintain charge transport during signalling of the aptamer/IFN-γ binding interactions. This suggestion is further confirmed by the Bode plots which reveal a lower phase angle shifted to higher frequency inducing a lower impedance modulus observed for the PProDOT-AuNPs-Apt-MCH platform when compared to the PProDOT-AuNPs-Apt. As expected, the PProDOT-AuNPs-Apt-MCH platform shows a higher charge transfer resistance in the presence of IFN-γ when compared to its absence. This confirms the ability of the aptamer to recognize and bind

its analyte as the observed charge transfer alterations are induced by the conformational

changes that occur during recognition and binding of the analyte [370,371].

http://etd.uwc.ac.za
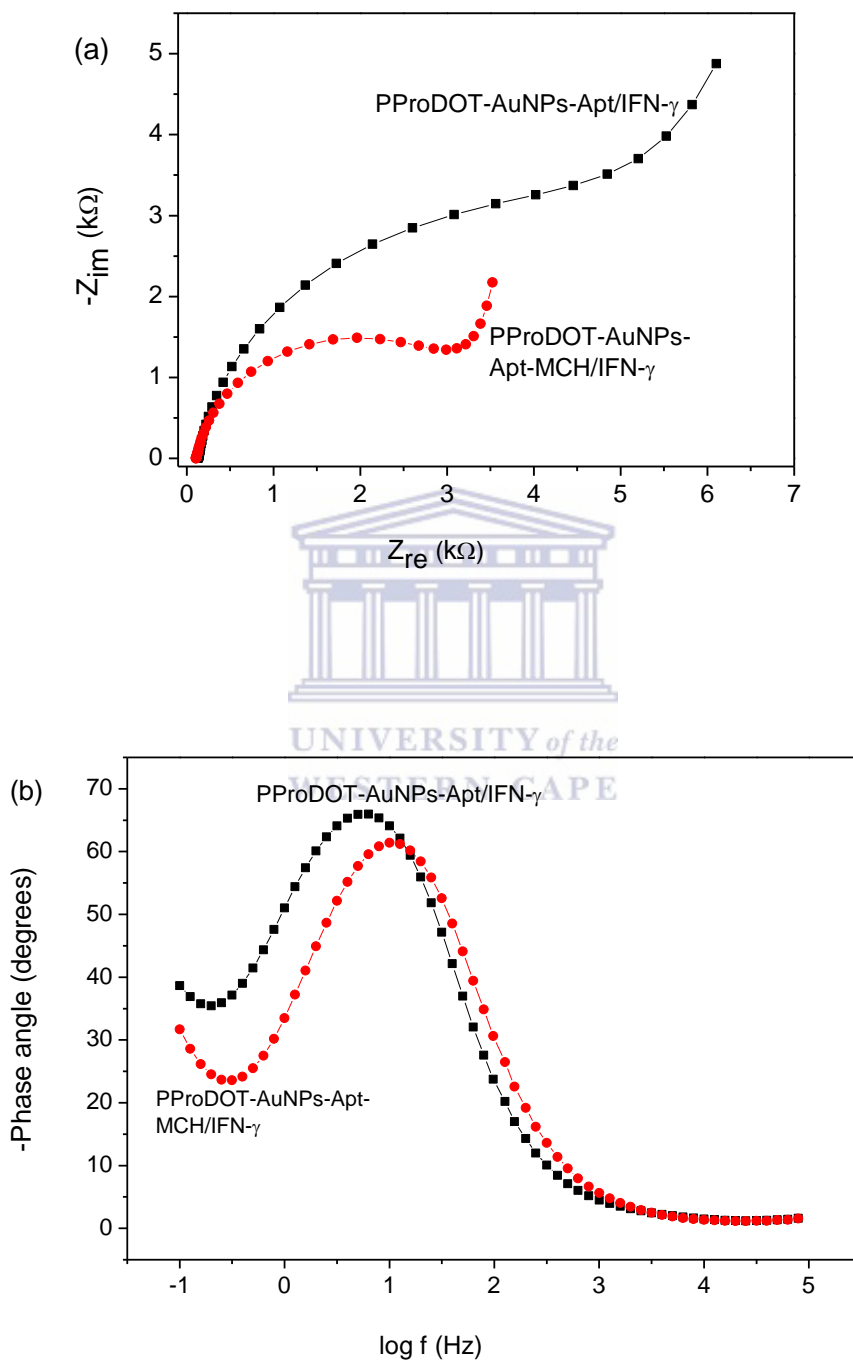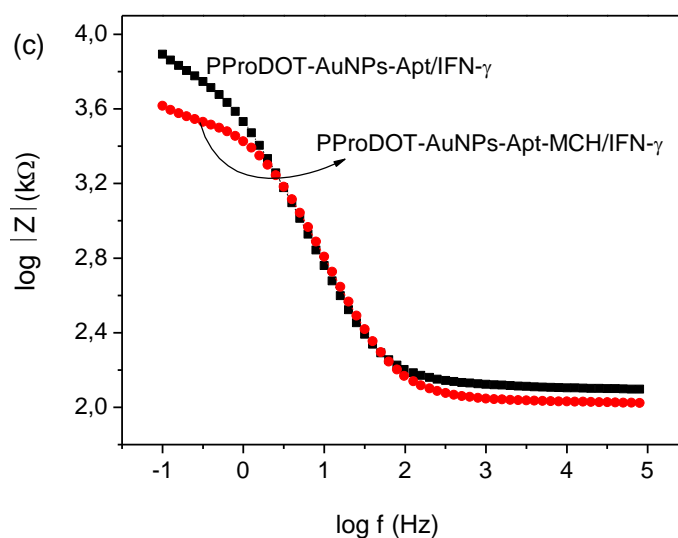
Figure 43: EIS measurements comparing the feasibility of the PProDOT-AuNPs-Apt-MCH sensing platform which shows better potential (than the PProDOT-AuNPs-Apt) towards IFN-γ detection.
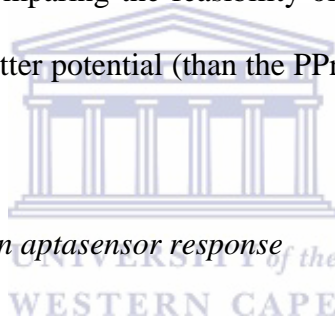
3.5. Effect of electrolyte pH on aptasensor response

The effect of electrolyte pH on the aptasensor response during IFN-γ signalling was investigated using CV and the result is shown in Figure 44(a). The experiments were conducted in acidic (pH = 5.4), neutral (pH = 7.4) and basic (pH = 10.4) solutions. The peak currents at which the aptasensor showed maximum response as a function of each solution pH is shown in Figure 44(b). The results illustrate that under acidic and basic conditions, the aptasensor shows poor performance which may be associated with distorted aptamer conformations while optimum performance is achieved at pH 7.4. Similar behaviour of a DNA molecule was observed by Mansor and co-researchers where they attributed the poor performance under acidic and basic conditions to decreased DNA hybridization associated with protonation of the DNA molecule [372]. Hence, phosphate buffer solutions of pH 7.4 were used throughout the biomarker detection experiments.

155
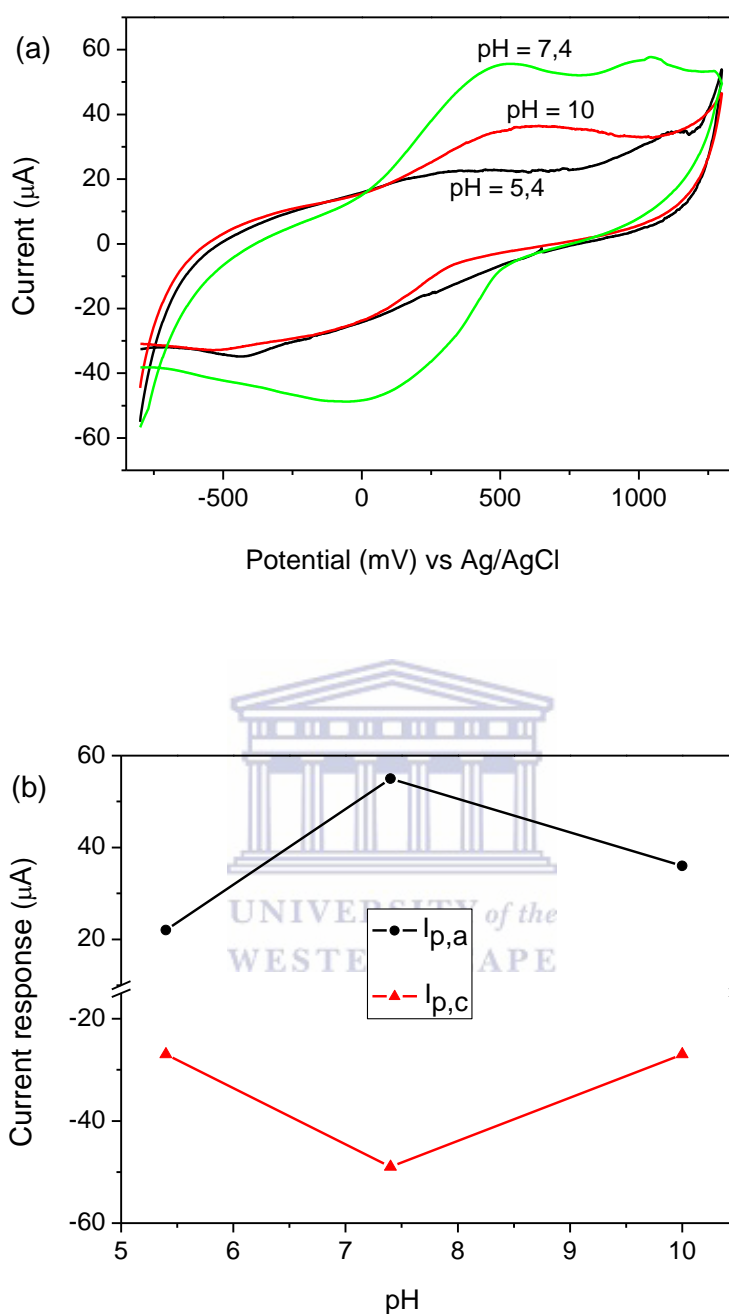
Figure 44: (a) CV graphs showing response of the PProDOT-AuNPs-Apt-MCH sensing platform in the presence of IFN-γ under different pH conditions and (b) the current response as a function of pH.

http://etd.uwc.ac.za

3.6. Aptasensor performance during signalling of IFN-γ in PBS

3.6.1.   PProDOT-AuNPs-Apt-MCH sensing platform in PBS

The performance of the PProDOT-AuNPs-Apt-MCH sensing platform was first assessed in phosphate buffer solutions at varying concentrations of IFN-γ using EIS. The Nyquist plot (Figure 45) illustrates a behaviour explained earlier (section 3.4) where the presence of the analyte decreases the charge transfer efficiency of the platform induced by the aptamer/IFN-γ conformational occurring during recognition and binding between them [373]. This trend continues with increasing concentrations of IFN-γ indicating occupation of more aptamer binding sites.
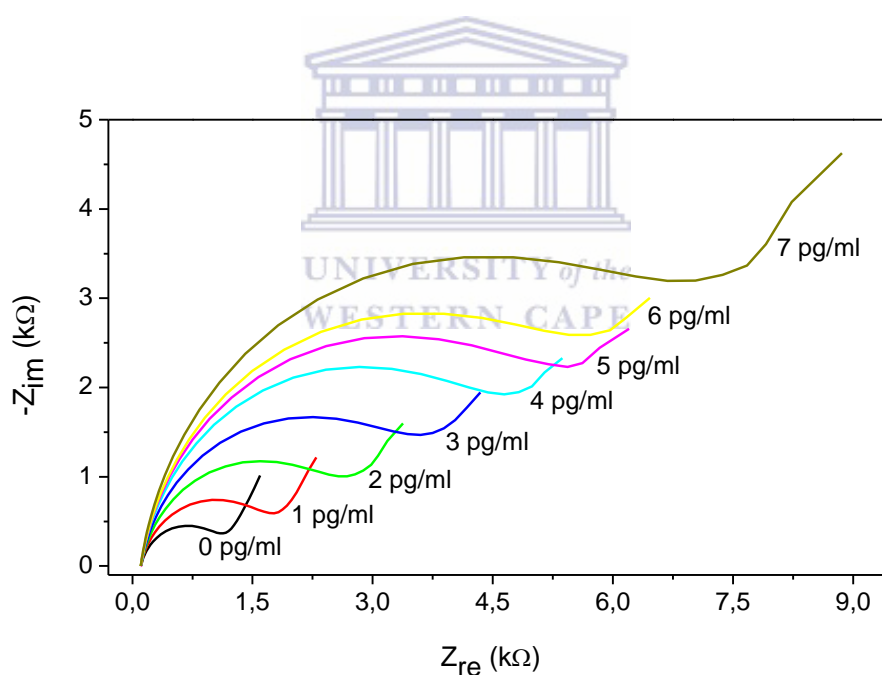

Figure 45: EIS Nyquist plot for the electrochemical signalling of IFN-γ. The Nyquist plot monitors phase angle shifts induced by IFN-γ binding from 0 pg/mL to 7 pg/mL (at increments of 1 pg/mL).

The Bode plot illustrating phase angle shifts as a function of frequency was also used to confirm this observation (Figure 46). With onset addition of the analyte, the system shows a shift to a higher phase angle (towards lower frequency. The calibration curve (Figure 47) shows a shifting to higher phase angles with increasing concentrations of IFN-. The plot illustrates a linear region between 0 pg/mL and 2 pg/mL. At concentrations higher than this range, the graph starts to plateau due to commencing saturation of the aptamer [374]. From the results, a limit of detection of 0.14 pg/mL at a sensitivity of 5º·mL/pg was determined.
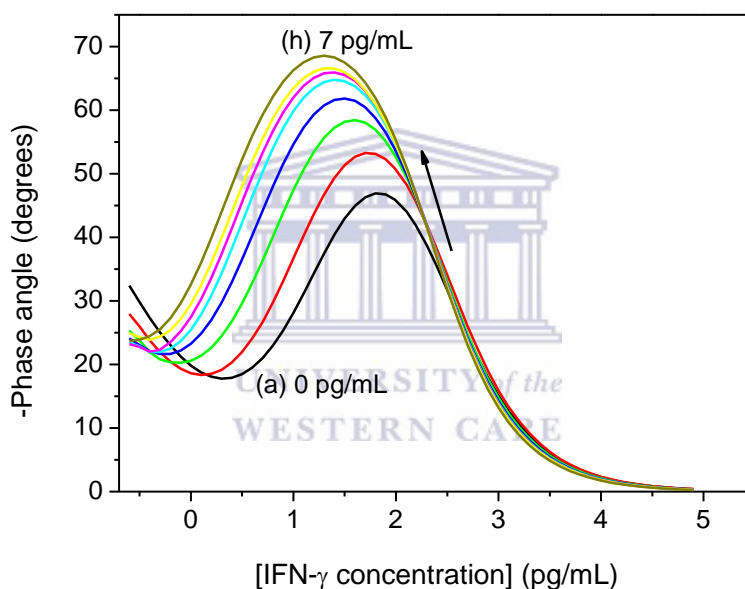

Figure 46: Electrochemical detection of IFN- γ by monitoring shifts in the phase angle with incremental IFN-γ concentrations of 1, 2, 3, 4, 5, 6 and 7 pg/mL in 0.1 M PBS (pH 7.4).
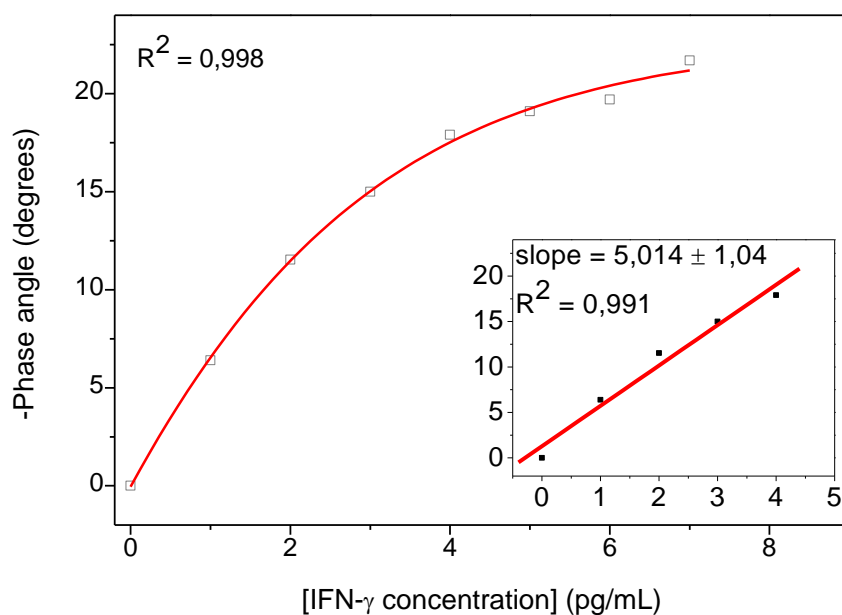
Figure 47: The calibration plot for performance of PProDOT-AuNPs-Apt-MCH sensing platform towards IFN-γ in 0.1 M PBS. The insert graph represents the analytical linear range.
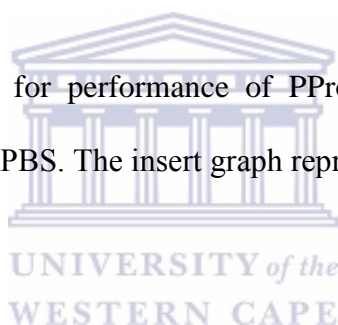
3.7. *Aptasensor performance during signalling of IFN-γ in pleural fluid*

3.7.1. *PProDOT-AuNPs-Apt sensing platform*

Although the blocking agents are associated with increased sensitivity of fabricated biosensor, MCH has been shown to interfere by replacing the aptamer binding (in the case of thiolated aptamers) due to the thiol group. So, the feasibility of both the MCH-blocked and unblocked sensing platforms towards IFN- signalling were both investigated. Figure 48 shows the Nyquist and Bode plot results for the response of the PProDOT-AuNPs-Apt sensing platform at IFN-γ concentrations between 0 pg/mL and 2.2 pg/mL. The sensitivity and limit of detection for this platform were estimated to be 14.4 5°·mL/pg and 0.19 pg/mL, respectively.

(a)

(b)

http://etd.uwc.ac.za
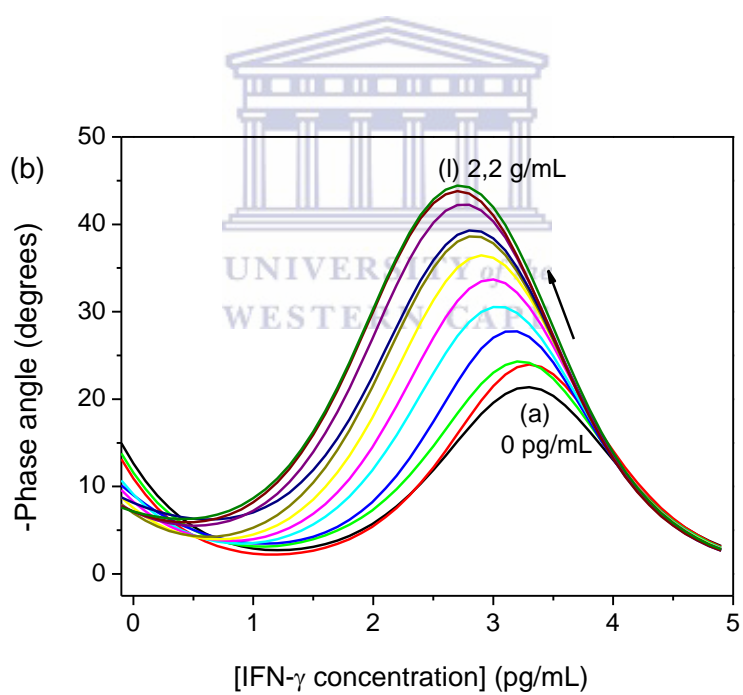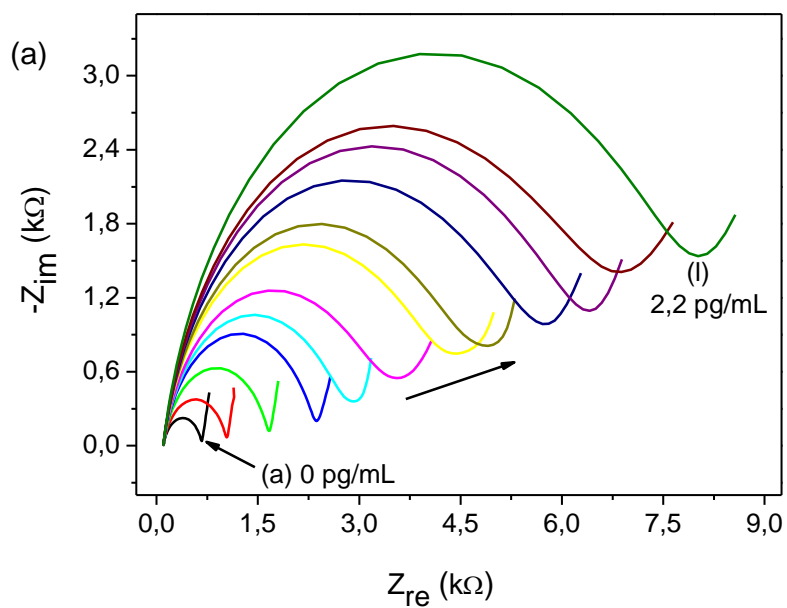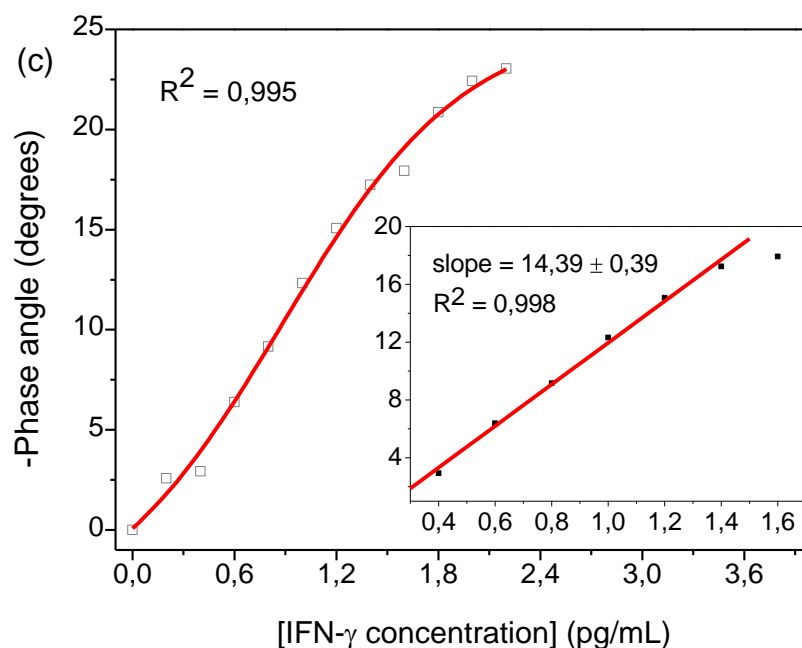
Figure 48: EIS results for the PProDOT-AuNPs-Apt platform during signalling of IFN-γ from 0 pg/mL to 2.2 pg/mL (at increments of 0.2 pg/mL). (a) Nyquist plot, (b) phase angle shifts as a function of IFN-γ concentration and (c) the calibration curve for the aptasensor performance (insert graph represents the analytical linear range).

3.7.2.   *PProDOT-AuNPs-Apt-MCH sensing platform*

The Nyquist and Bode plot results for the response of the PProDOT-AuNPs-Apt-MCH sensing platform at IFN-γ concentrations between 0 pg/mL and 2.2 pg/mL is shown in Figure 49. The sensitivity and limit of detection for this platform were estimated to be 6.34 5º·mL/pg and 0.2 pg/mL, respectively. It is very important to note that the MCH-free (unblocked) sensing platform shows a steeper curve than the MCH-blocked sensing platform. This may be attributed to interferences resulting from the exposed active groups of the nanocomposite hosting the aptamer, leading to the observed lower detection limit. The MCH-blocked sensing platform

shows a curve that starts plateauing after 1.0 pg/mL indicating the less available binding sites

and, hence, its saturation commences.

http://etd.uwc.ac.za
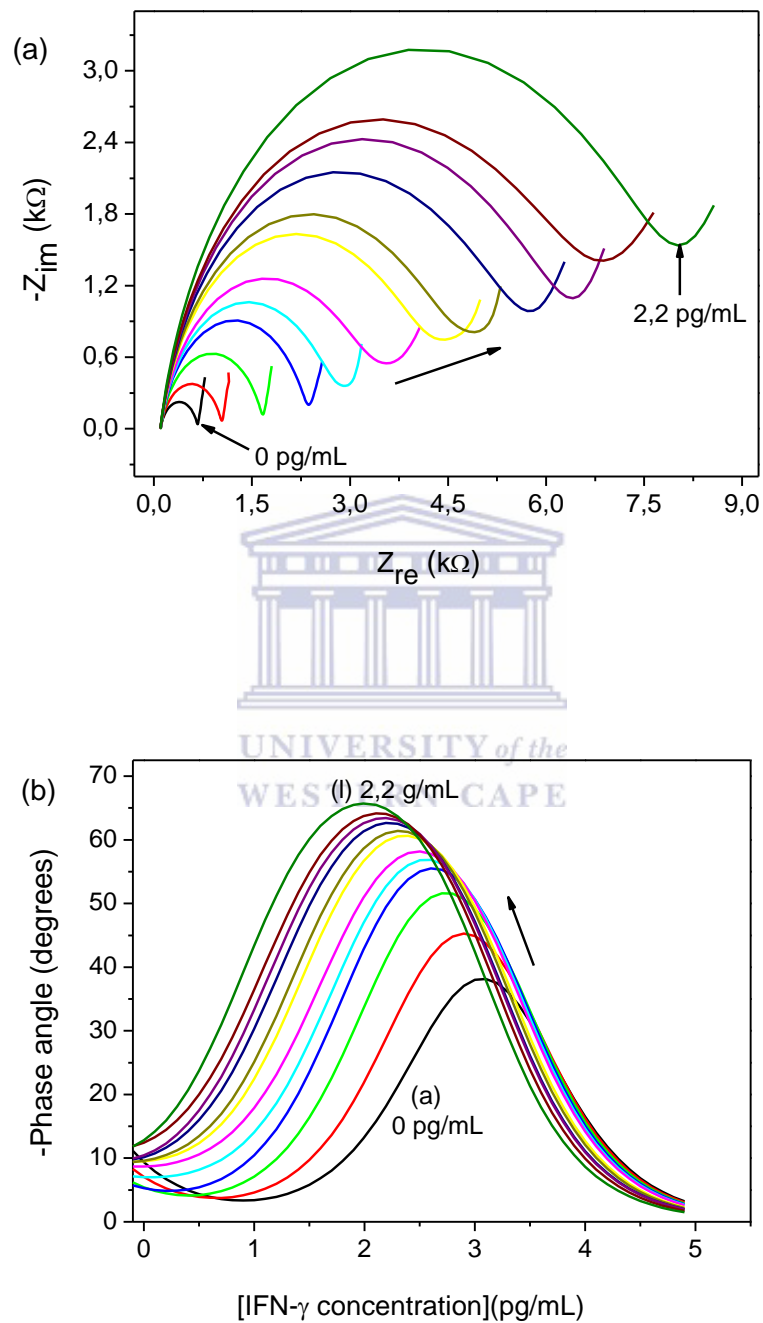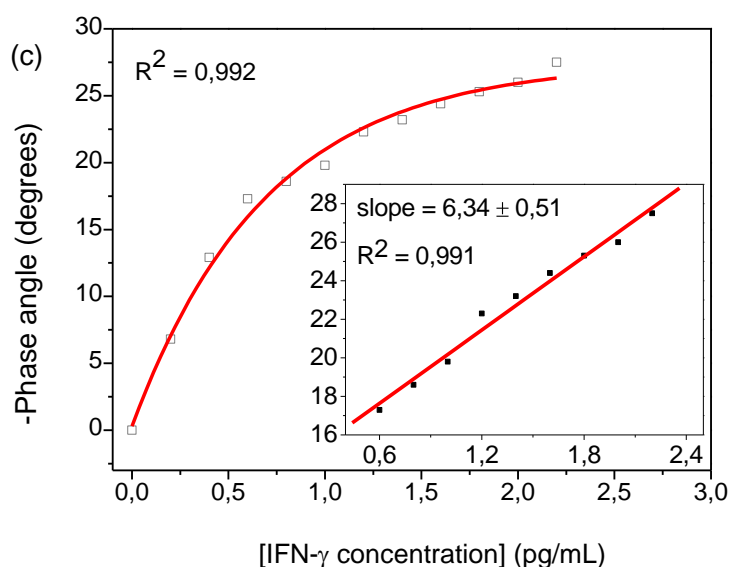
Figure 49: EIS results for the PProDOT-AuNPs-Apt-MCH platform during signalling of IFN-γ from 0 pg/mL to 2.2 pg/mL (at increments of 0.2 pg/mL). (a) Nyquist plot, (b) phase angle shifts as a function of IFN-γ concentration and (c) the calibration curve for the aptasensor performance (insert graph represents the analytical linear range).
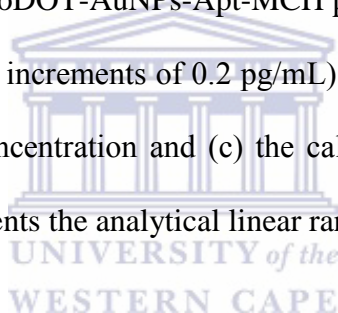
The performance of this aptasensor is within reported literature range for different detection methods aimed towards early diagnosis of TB. For clear comparison, Table summarizes different sensors employing various biomolecules, nanomaterials and signalling methods for detection of TB through signalling of its identifiers such as the *MTb* strains and, mostly, its specific antigens.

Table 2: Detection limit performance of sensors fabricated for early detection of TB by signalling its cytokines using various methods.

Sensor components	Signalling method	Target analyte	Sample; LOD (M/ g/mL)	Reference
Silica nanotraps and trypsin	MALDI-TOF-MS	CFP-10	MTb culture; 1.4 nM	[375]
Anti-IFN-γ antibodies onto a gold monolayer with signal amplification of quantum dots and methylene blue	SWASV	IFN-γ	Serum; 0.34 pg/mL	[376]
Anti-IFN-γ aptamer onto a PProDOT-AuNPs nanocomposite	EIS	IFN-γ	PLF; 0.2 pg/mL	This study
Protein conjugates of silica-coated quantum dots and gold nanorods with antibodies	SPR	Ag85B	PBS; 13 pg/mL	[377]

4. Conclusion

This work reports on electrochemical signalling of interferon gamma using its specific DNA aptamer. The aptamer was hosted by a highly electroconductive nanocomposite of poly(3,4-propylenedioxythiophene) and gold nanoparticles. The nanocomposite is a binary system achieved through the covalent bonding between the sulfur element of PProDOT and the gold element of the gold nanoparticles. Immobilization of the thiolated DNA aptamer onto the

http://etd.uwc.ac.za

nanocomposite led to a ternary system in which the electron charge transfer efficiency was maintained, although there was an observable decrease in the presence of the aptamer.

In accord with literature, a blocking agent was employed as a blocking agent to minimise non-specific adsorptions. The presence of the blocking agent, mercaptohexanol, slightly increased the charge transfer efficiency of the sensing platform. Feasibility of the of both the MCH-blocked and unblocked sensing platforms as signalling assays for the tuberculosis biomarker, interferon gamma, was evaluated using electrochemical impedance spectroscopy.

After observing a positive response after single-shot additions of IFN-γ, the assays were evaluated against various concentrations of. Firstly, the MCH-blocked sensing platform was evaluated against concentrations of IFN-γ in phosphate buffer. The performance was satisfactory and in agreement with calibration profiles of electrochemical biosensor system by showing the polynomial profile whose plateau is defines saturation of the biomolecule. An estimated detection limit of 0.14 pg/mL was achieved. When applied in pleural fluid-spiked samples, the sensing platform still showed satisfactory performance with a detection limit of 0.2 pg/mL. The performance of this sensing platform was compared with that of the unblocked platform which displayed detection limit of 0.19 pg/mL. This behaviour was associated with the complexity of the matrices like the pleural fluid used here. Most importantly, both the detection limits and analytical linear ranges of the sensing platforms fall below the cut-off concentration of 15 pg/mL for IFN-γ, hence highlighting the potential use of these platforms in clinical samples towards early diagnosis of the disease tuberculosis.

5. References

348.   Achkar, J. M., Cortes, L., Croteau, P., Yanofsky, C., Mentinova, M., Rajotte, I., Schirm, M., Zhou, Y., Junqueira-Kipnis, A.P., Kasprowicz, V.O., Larsen, M., Allard, R., Hunter, J. & Paramithiotis, E. Host Protein Biomarkers Identify Active Tuberculosis in HIV Uninfected and Co-infected Individuals. *EBioMedicine.* 2(9), 1160–1168 (2015).

349.   Osei, E., Akweongo, P. & Binka, F. Factors associated with DELAY in diagnosis among tuberculosis patients in Hohoe Municipality, Ghana. *BMC Public Health.* 15, 1-11 (2015).

350.   Chaves, A. S., Rodrigues, M. F., Mattos, A. M. M. & Teixeira, H. C. Challenging Mycobacterium tuberculosis dormancy mechanisms and their immunodiagnostic potential. *Brazilian J. Infect. Dis.* 19, 636–642 (2015).

351.   Ai, J.W., Ruan, Q.L., Liu, Q.H. & Zhang, W.H. Updates on the risk factors for latent tuberculosis reactivation and their managements. *Emerg. Microbes Infect.* 5(2), 1-8 (2016).

352.   Bibbins-Domingo, K., Grossman, D.C., Curry, S.J., Bauman, L., Davidson, K.W., Epling, J.W. Jr., García, F.A., Herzstein, J., Kemper, A.R., Krist, A.H., Kurth A.E., Landefeld, C.S., Mangione, C.M., Phillips, W.R., Phipps, M.G., Pignone, M.P. Screening for Latent Tuberculosis Infection in Adults US Preventive Services Task Force Recommendation Statement. *JAMA .* 95, 962-969 (2017).

353.   Penn-Nicholson, A., Scriba, T. J., Hatherill, M., White, R. G. & Sumner, T. A novel blood test for tuberculosis prevention and treatment. *South African Med. J.* 107(1), 4-5 (2016).

354.   Kigozi, G., Heunis, C., Chikobvu, P., Botha, S. & van Rensburg, D. Factors

influencing treatment default among tuberculosis patients in a high burden province of South Africa. *Int. J. Infect. Dis.* 54, 95–102 (2017).

355.   Kalonji, G. M., De Connick, G., Ngongo, L.O., Nsaka, D.K., Kabengele, T., Kandolo, F.T., Ilunga-Ilunga, F., Adelin, A. & Giet, D. Prevalence of tuberculosis and associated risk factors in the Central Prison of Mbuji-Mayi, Democratic Republic of Congo. *Trop. Med. Health.* 44, 1-18 (2016).

356.   Pai, M. & Schito, M. Tuberculosis diagnostics in 2015: Landscape, priorities, needs, and prospects. *J. Infect. Dis.* 211, S21–S28 (2015).

357.   Cudahy, P. & Shenoi, S. Diagnostics for pulmonary TB. *Postgrad. Med. J.* 92(1086), 187–193 (2016).

358.   Leylabadlo, H. E., Kafil, H. S., Yousefi, M., Aghazadeh, M. & Asgharzadeh, M. Pulmonary tuberculosis diagnosis: Where we are? *Tuberc. Respir. Dis. (Seoul).* 79, 134–142 (2016).

359.   Yamanaka, K., Vestergaard, M. C. & Tamiya, E. Printable electrochemical biosensors: A focus on screen-printed electrodes and their application. *Sensors.* 16, 1–16 (2016).

360.   Hammond, J. L., Formisano, N., Estrela, P., Carrara, S. & Tkac, J. Electrochemical biosensors and nanobiosensors. *Essays Biochem.* 60, 69–80 (2016).

361.   Mallikaratchy, P. Evolution of Complex Target SELEX to Identify Aptamers against Mammalian Cell-Surface Antigens. *Molecules.* 22, 215 (2017).

362.   Wolter, O. & Mayer, G. Aptamers as Valuable Molecular Tools in Neurosciences. *J. Neurosci.* 37, 2517-2523 (2017).

363.   Parashar, A. Aptamers in therapeutics. *J. Clin. Diagnostic Res.* 10, BE01-BE06 (2016).

364.   Cardoso, A. R., Moreira, F. T. C., Fernandes, R. & Sales, M. G. F. Novel and

simple electrochemical biosensor monitoring attomolar levels of miRNA-155 in breast cancer. *Biosens. Bioelectron.* 80, 621–630 (2016).

365.   Olowu, R.A., Williams, A., Ndangili, P.M., Ngece, R.F., Mailu, S.N., Baker, P. & Iwuoha, E. Impedimetry and microscopy of electrosynthetic poly (propylene thiophenoimine)-co-poly(3,4 ethylene dioxythiophene) dendritic star copolymer. *Int. J. Electrochem..* 6, 1855–1870 (2011).

366.   Jin, S., Ye, Z., Wang, Y. & Ying, Y. A Novel Impedimetric Microfluidic Analysis System for Transgenic Protein Cry1Ab Detection. *Sci. Rep.* 7, 43175 (2017).

367.   Fomo, G., Waryo, T.T., Sunday, C.E., Baleg, A.A., Baker, P.G. & Iwuoha, E.I.. Aptameric Recognition-Modulated Electroactivity of Poly(4-Styrenesolfonic Acid)-Doped Polyaniline Films for Single-Shot Detection of Tetrodotoxin. *Sensors* 15, 22547–22560 (2015).

368.   Khalilzadeh, B., Shadjou, N., Afsharan, H., Eskandani, M., Nozad, C.H. & Rashidi, M.R. Reduced graphene oxide decorated with gold nanoparticle as signal amplification element on ultra-sensitive electrochemiluminescence determination of caspase-3 activity and apoptosis using peptide based biosensor. *BioImpacts.* 6, 135–147 (2016).

369.   Chen, W., Liu, Y.H., Li, H.N., Liu, A.L., Lin, X.H. & Chen, Y.Z. Ultrasensitive and facile electrochemical deoxyribonucleic acid biosensor based on the conformational change of the recognition interface. *Anal. Chim. Acta*. 748, 89–94 (2012).

370.   Zhang, A., Chang, D., Zhang, Z., Li, F., Li, W., Wang, X., Li, Y. & Hua, Q. In vitro selection of DNA aptamers that binds geniposide. *Molecules.* 22(3), 1–12 (2017).

371.   Masikini, M., Williams, A.R., Sunday, C.E., Waryo, T.T., Nxusani, E., Wilson, L., Qakala, S., Bilibana, M., Douman, S., Jonnas, A., Baker, P.G.L. & Iwuoha, E.I.

Label free poly(2,5-dimethoxyaniline)-multi-walled carbon nanotubes impedimetric immunosensor for fumonisin B1 detection. *Materials..* 9(4), 1-14 (2016).

372.   Mansor, N. A., Zain, Z.M., Hamza, H.H., Noorden, M.S.A., Jaapar, S.S., Beni, V. & Ibupoto, Z.H. Detection of Breast Cancer 1 (BRCA1) Gene Using an Electrochemical DNA Biosensor Based on Immobilized ZnO Nanowires. *Open J. Appl. Biosens.* 3, 9–17 (2014).

373.   Aliakbarinodehi, N., Jolly, P., Bhalla, N., Micheli, D., Estrela, P. & Carrara, S. Aptamer-based Field-Effect Biosensor for Tenofovir Detection. *Sci. Rep.* **7,** 1-10 (2017).

374.   Ocaña, C., Pacios, M. & del Valle, M. A reusable impedimetric aptasensor for detection of thrombin employing a graphite-epoxy composite electrode. *Sensors.* 12, 3037–3048 (2012).

375.   Wu, H-J., Li, Y., Fan, J., Deng, Z., Hu, Z., Liu, X., Graviss, E.A., Ferrari, M,m Ma, X. & Hu, Y. Antibody-Free detection of Mycobaterium tuberculosis Antigen Using Customized Nanotraps. *Anal. Chem.* 86, 1988-1996 (2014).

376.   Huang, H., Li, J., Li, S., Yan, Y., Zhang, M., Wang, P., Zeng, G. & Jiang, Z. Detection of Interferon-Gamma for Latent Tuberculosis Diagnosis Using an Immunosensor Based on CdS Quantum Dots Coupled to Magnetic Beads as Labels. *Int. J. Electrochem. Sci.* 10, 2580 – 2593 (2015).

377.   Kim, E.J., Kim, E.B., Lee, S.W., Cheon, S.A., Kim, H-J., Lee, J., Lee, M-K., Ko, S. & Park, T.J. An easy and sensitive sandwich assay for detection of Mycobacterium tuberculosis aAg85B antigen using quantum dots and gold nanorods. *Biosens. Bioelectron.* 87, 150-156 (2017).

Chapter 6

Concluding remarks and future perspectives

The study reports on two biosensor platforms fabricated using an enzyme and an aptamer onto different conducting polymer nanocomposites. The sensors were used for quantification of bisphenol A (an endocrine disrupting chemical associated with negative human health effects and environmental pollution) and interferon gamma (a cytokine produced as an immunological response to tuberculosis infection). All concluding and future perspectives concerning this study will be identified separately starting with the preparation of the nanocomposites to fabrication and application of the biosensor systems.

(a). The poly(methyl methacrylate) and titanium dioxide-grafted polyaniline nanocomposite
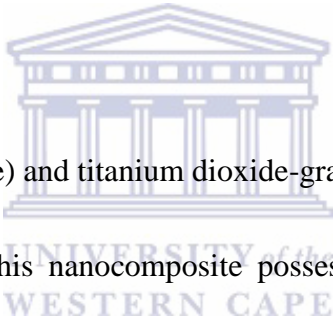
The individual components of this nanocomposite possess properties which gained them undivided attention for applications in various fields. Poly(methyl methacrylate) is a biocompatible hydrogellic polymer which also has a swelling behaviour which gained it applications in the biomedical field. Its biocompatibility has shown to non-destructively host biomolecules during biosensor fabrication. Hence it was employed here to play the biocompatible host for the enzyme manganese peroxidase.

Polyaniline (PANI) is an electroconductive polymer with reversible activity that can be further enhanced by incorporation of different molecules to overcome its undesirable loss of electroconductivity in neutral environments. Different molecules (including polymers and nanomaterials) have been incorporated to PANI, yielding nanocomposites and nanohybrids with outstanding properties and performance reflecting the synergistic effect of the combined components. Titanium dioxide (TiO_2) nanoparticles have been shown to tune different

properties of PANI towards improving the performance of dye-sensitized solar cells and photocatalysts. Hence, this study sought to prepare a nanocomposite that would reflect all the properties of PANI, PMMA and TiO_2. Although the amounts of both PMMA and TiO_2 nanoparticles were kept at a minimum, electrochemical characterization using cyclic and square wave voltammetry shows that the dopants (individually and combined) significantly increased the electroconductivity of PANI. Moreover, this phenomenon was attained in neutral pH phosphate buffer electrolyte (at pH 7.4) and this was attributed to the effect of the incorporated PMMA and TiO_2 increasing charge carriers and their delocalization along the polymer backbone, hence the observed electrical conductivity with a fifty-fold magnitude increase for the nanocomposite peak currents when compared to pristine PANI. The nanocomposite showed good reversible charge transfer efficiency investigated and confirmed by CV at varying scan rates.

Through UV-Vis spectroscopy, the nanocomposite was characterized to have an absorption peak in the visible spectral range and exhibited a lower energy band gap, hence implying improved biocompatibility when compared to PANI. This alone implies the possible application of the nanocomposite in energy-harvesting devices which require narrow band gaps. Based on the fixed amount of dopants used here, it would be necessary to further investigate the following aspects:

i.   The effect of varying the amounts of dopants on optical properties of PANI based on the electron donating behaviour of PANI and the electron withdrawing behaviour of PMMA while the electron transfer from the highest occupied molecular orbital of PANI to the lowest unoccupied molecular orbital of TiO_2 alleviates the electron-hole recombinations of TiO_2.

ii.   Thermal and cycling stability of the nanocomposite for trial in battery electrode and supercapacitor materials following the portrayed electrical conductivity and porosity necessary for enhanced charge diffusion and charge-discharge efficiency.

iii.   Direct quantification of bisphenol A using the nanocomposite which is expected to have minimal electrode fouling effect usually observed during direct oxidation of BPA on bare electrodes, induced by its polymerization.

iv.   Biodegradation studies of the nanocomposite into the less toxic carbon and nitrogen compounds which would widen the application scope of the nanocomposite into the biomedical field.

(b). Bisphenol A quantification

The step-wise fabrication of the biosensor system was confirmed by CV where the decrease in peak currents was observed after introduction of the enzyme into the system. This was correlated to the binding between the amine groups of PANI and the carboxyl groups from the C-terminus of the amino acids in the enzyme or through hydrogen bonding between the amine group from the N-terminus of the amino acids and the hydroxyl group from TiO_2 and the carboxyl group from the PMMA (as proposed in Figure 10). After an onset introduction of the target analyte, BPA, into the system, a catalytic redox pair with a formal potential of +136 mV (vs Ag/AgCl) was ascribed to the transitions of the iron heme group of the enzyme, coupled to formation of the oxygenated complex induced by binding of BPA while a peak in the far positive potentials (at +760 mV vs Ag/AgCl) conferred polymerization of BPA, forming an insulating film that hindered charge transfer as witnessed by the subsequent drop in peak current differences with increasing concentrations of BPA.

The biosensor system reported here was first-of-a-kind, based on manganese peroxidase for quantification of BPA, an endocrine disrupting chemical whose negative impact on human

health led to the minimum instated tolerable daily intake value of 4 µg/kg bodyweight by the .

The biosensor system portrays the signature polynomial profile associated with the behaviour

of many biomolecule-based sensors where the steep linear part correlates to the analytical linear

range while the plateau which commences at higher concentrations is associated with saturation

of the biomolecule. By monitoring changes in current (induced by binding of bisphenol A to

the enzyme active site) an estimated detection limit of 0.17 nM was obtained with a sensitivity

of 21.1 ± 0.621 µA/nM. These values are in accord with other electrochemical biosensor-based

techniques in which the sensitivity has been tuned by different strategies including the use of

BPA-specific aptamers and nanoparticle–based signal amplifiers. However, parameters such

as the concentration of the enzyme, specificity of the biosensor system, the binding affinity of

BPA to the enzyme, amount and nature of blocking agent, investigation of the sensor system

in real samples, reproducibility and validation using other methods still need further

investigation to widen the linear range, increase the sensitivity and broaden the application

scope of the nanobiosensor system for quantification of various analytes towards

environmental protection, human health protection and wildlife preservation.

(c). The poly(3,4-propylenedioxythiophene)-gold nanoparticles composite

Poly(3,4-propylenedioxythiophene) (PProDOT) was prepared from its monomer through the

chemical oxidative polymerization route using tetrachloro-auric solution as an oxidizing agent.

The procedure was a simple reaction performed at room temperature with a slight stirring

impact. The SEM and TEM images identified pod-like structures when the preparation

conditions were adjusted to a higher temperature while at room temperature irregular sticks

were observed. Similarly to other conducting polymers, PProDOT has been shown to have

poor solubility in most solvents, an undesirable behaviour that opened doors to the widely

investigated PProDOT analogues based on functionalization or modification of the monomer

to tune its hydrophobicity and/or hydrophilicity. The chemical polymerization and solid-state milling methods are the most investigated deposition methods, following the challenges of electrochemically depositing PProDOT onto various substrates. All the polymerization routes yield polymers with different morphologies and subsequently, varying properties. To enhance different properties of PProDOT, especially its electroconductivity, a nanocomposite with Au-S linking resulting from incorporation of gold nanoparticles was hypothesized. Gold nanoparticles are among the most versatile metallic nanoparticles that can be easily prepared through various methods, including the green chemistry approaches and can be functionalized with different molecules for specific purposes. For example, gold nanoparticles have been used in biomedicine as therapy vehicles to deliver agents such as drugs and silencing aptamers to targeted sites. Considering the semiconductive nature of the polymer related to its biocompatibility, this nanocomposite could also potentially be tested for therapeutic applications.
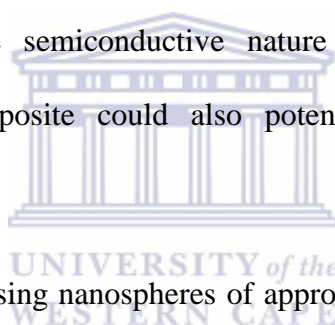
Indeed, a nanocomposite comprising nanospheres of approximately 100 nm in diameter was achieved and the TEM clearly showed the AuNPs being attached and distributed within the PProDOT polymeric network. It was noted that very small nanoparticles of 2.5 nm diameters were revealed by the TEM at higher magnification, suggesting possibility of a novel preparation route towards carbon dots. Specifically withdrawing from this observation, this study will be extended to investigate these nanoparticles and adapt to the other deposition methods while continuously and precisely spotting the effects of different parameters including the amount of oxidizing agent, solvent effects and a preparation method that would correlate to better performance of the nanocomposite.

The nanocomposite was tested as an electron mediator and biomolecule host for fabrication of an aptamer assay for signalling a tuberculosis biomarker. The nanocomposite showed good charge transfer efficiency and also demonstrated better reversibility during the charge-

discharge processes and this was correlated to faster charge diffusion kinetics attributed to the porous nanostructured morphology revealed by the scanning electron microscopy which facilitates charge diffusion. This fast behaviour could be beneficial towards rapid analysis of different pathogens, toxins and pollutants.

(d). Interferon gamma signalling

The stepwise fabrication method of the aptasensor permitted precise determination of induced current, charge transfer resistance, phase angle and impedance changes as per fabrication step. The aptasensor developed here is a ternary covalently-linked system, however, its stability still needs to be investigated. The aptasensor system showed good response towards interferon gamma signalling in both the clean phosphate buffer solution and in pleural fluid-spiked samples. A detection limit of 0.2 pg/mL was estimated for the interferon gamma detected in pleural fluid and this implies potential for practical application of the aptasensor system for signalling interferon gamma in clinical matrices.

(e). Future goals aimed at early TB diagnosis

Secretion of cytokines, such as the interferon gamma, is altered by endocrine disrupting chemicals. Amongst these chemicals, bisphenol A has been proven to interfere with IFN-γ secretion and therefore alter its levels. The study will be furthered to investigate simultaneous signalling of both BPA and IFN-γ. After necessary optimizations, the aptasensor system would be a point-of-care diagnostic device for both early identification of TB infection and endocrine disruption. However, to realize the out-of-laboratory practical application by clinicians, medical practitioners and all other individuals, this aptasensor system would need integration into an automated, portable and user-friendly device.

http://etd.uwc.ac.za